

UNIVERSITY OF OKLAHOMA
GRADUATE COLLEGE

UNCONVENTIONAL WOODFORD SHALE CHARACTERIZATION USING
SEISMIC ANISOTROPY

A THESIS
SUBMITTED TO THE GRADUATE FACULTY
in partial fulfillment of the requirements for the
Degree of
MASTER OF SCIENCE

By
OLUWATOBILOBA FRANCIS OYEBANJI
Norman, Oklahoma

2019

UNCONVENTIONAL WOODFORD SHALE CHARACTERIZATION USING
SEISMIC ANISOTROPY

A THESIS APPROVED FOR THE
SCHOOL OF GEOSCIENCES

BY THE COMMITTEE CONSISTING OF

Dr. Roger Slatt, Co-Chair

Dr. Kurt Marfurt, Co-Chair

Dr. Heather Bedle

© Copyright by OLUWATOBILOBA FRANCIS OYEBANJI 2019

All Rights Reserved.

ACKNOWLEDGEMENT

First, I acknowledge Almighty God, the author and finisher of my life, who has seen me through till this moment. The one that crowns my little efforts and strives with success. I will be eternally grateful to the Hurlimanns, my family from Switzerland, for their relentless support all through my graduate program. They are simply God-sent. To my parents, my backbone, and my root, I thank them for being there with prayers and moral support since day one.

I would like to express sincere gratitude to my advisors Dr. Roger Slatt and Dr. Kurt Marfurt for the belief, patience, encouragement and trust they had in me. In them, I found a friend, mentor and a father. Having them as my advisor is nothing short of grace. It is a huge honor to be supervised and mentored by these gentlemen. For them, I was work-in-progress and they never stopped providing the moral, financial, and academic support for me to grow. A special thanks to Dr. Heather Bedle who always have the listening ears, keep an open-door policy, and provides insightful ideas.

Successes made during my program and research would have been impossible without the input of brilliant and great friends like Thang Ha, Swetal Patel, Emilio Torres, Muizz Matemilola, Davide Duarte, AJ McGlannan, Gabriel Machado, Sophia Caylor, Jing Zhang, Folarin Kolawole, Bin Lyu, Davide Lubo, Alex Arroyo, Saurabh Sinha, Lennon Infante to mention but a few. They made studying fun, life

easier, and programming less tortuous. I value and cherish all the time spent with them. A special mention to Raymond Ng and Joe Sher, some of the most selfless and caring person I have ever met.

Also, a special shout-out to the administrative staffs of the department, Rebecca Fay, Leah Moser and Ginger Leivas and Robert Turner for the back-end support.

Table of content

1	INTRODUCTION.....	2
2	GEOLOGICAL BACKGROUND.....	5
2.1	Structural Setting.....	5
2.2	Stratigraphic Setting.....	9
2.3	Study Area.....	12
3	MATERIALS AND METHODS.....	13
3.1	Materials (data quality check and normalization).....	13
3.1.1	Well-log Conditioning.....	14
3.1.2	Seismic Data Conditioning.....	16
3.2	Sequence Stratigraphy (Log correlation) and Petrophysical Analysis.....	20
3.3	Seismic Inversion and Attributes Analysis.....	25
3.3.1	Log Correlation.....	28
3.3.2	Inversion Issues.....	31
3.4	Amplitude Variation with Azimuth (AVAz): Analysis and Inversion.....	33
3.4.1	Anisotropy.....	33
3.4.2	Theory of Anisotropy.....	34
3.4.3	Anisotropic Amplitude Variation with Offset (AVO) Analysis.....	40
3.4.4	Amplitude Variation with Azimuth (AVAz) Inversion.....	44
3.4.5	AVAz Modelling.....	46
3.5	Seismic Attribute Analysis.....	50
3.5.1	Coherence (Similarity).....	50
3.5.2	Curvature.....	51
4	RESULTS AND DISCUSSIONS.....	52
4.1	Log Correlation.....	52
4.2	Petrophysical Analysis.....	56
4.2.1	Stiffness.....	56
4.3	Seismic Inversion.....	59
4.3.1	Inversion Process.....	59

4.3.2	Seismic Inversion: Results, Resolution, and Tuning Effect	61
4.4	AVAz analysis and Inversion.....	67
4.4.1	AVAz Inversion and Seismic Attributes.....	75
5	CONCLUSIONS AND LIMITATIONS	82
6	REFERENCES	84
7	Appendix	89

List of Tables

Table 1. Values of the four models used to test for AVAz analysis. From Ruger (2012).....	48
--------------------------------------------------------------------------------------------------	----

List of Figures

Figure 1.1 Field-based lithofacies classification scheme for Woodford Shale mudrock. The first criterion distinguishes between hard and soft beds; then compositional and textural descriptors are added to the rock name. Seven lithofacies were recognized within the Woodford Shale at the Speake Ranch outcrop. The mineral composition of the lithofacies is illustrated in the ternary plot and reveals that most of the Woodford mudrock plot along the quartz-clay axis. The pie chart suggests siliceous shales, cherts, and siliceous mudstones as being the most abundant lithofacies, which account for more than 80% of the entire lithological record (from Galvis et al., 2018)..... 2

Figure 1.1 Summary of hypothetical reservoir quality (RQ) and completion quality (CQ) as interpreted based on the stacking patterns between soft and hard beds. Model 1 is typical of the lower Woodford member in which thick soft beds dominate. Model 2 presents the optimal balance between RQ and CQ, and it is characterized by the 50/50 soft-to-hard ratio made of thin beds. Model 3 illustrates a predominance of thicker hard beds, which is very typical of the upper Woodford member (from Galvis et al., 2018). 3

Figure 2.2.1 Isopach map of Cambrian Timbered Hills and upper Cambrian through lower Ordovician Arbuckle Groups, Oklahoma and western Texas. Contour interval, 1,000 and 2,000 ft; contour hachured to indicate closed low. Stippling represents areas in which Cambrian and lower Ordovician rocks are deeply eroded or removed to basement. Screen pattern represents depocentral area of southern Oklahoma trough. Modified from Gatewood (1978). 6

Figure 2.2.2 A Paleotectonic map highlighting tectonic activities such as continental margins and rift; during the late Proterozoic and early Paleozoic time. DA, Delaware aulacogen; RCG, Rough Creek graben; RFR, Reelfoot rift; RT, Rome trough; SOA, southern Oklahoma aulacogen. Modified from Keller and others (1983). 8

Figure 2.3 Stratigraphic column of the Woodford Shale across the Anadarko Basin area. (United States Geological Survey, USGS). 10

Figure 2.4 Map of Oklahoma showing location of the study area within the red rectangle and location of the complete section of the Woodford Shale outcrop within the blue rectangle about 156 miles away (Johnson,2008)..... 12

Figure 3.1 Locations of the all the wells within the study area (in the big black rectangle). Wells ‘OPD’, ‘WER’ and ‘NER’ are located within the seismic survey area (in the small black rectangle). The location of the reference outcrop is within the blue rectangle on the map. 13

Figure 3.2 A display of the amount of trace per azimuth (a) and the amount of bins along each azimuth (b) in the seismic volume used. 14

Figure 3.3 Well-log correction; (a) Repeated high frequency spikes noticed in the sonic shear and compressional log within the red box, highlighted by the blue arrows. (b) A reasonably smoothed sonic curve after applying harmonic filter to attenuate the coherent noise. 15

Figure 3.4 Spectral balancing of the seismic volume from 1.5 to 2.2seconds. (a) Spectrum of raw seismic volume, the peak frequency at 25Hz; low pass and cut at 0Hz to 15Hz and high pass and cut at 35Hz to 55Hz. Bottom: After spectral balancing, the amplitude of high frequencies component restored and the range of the spectrum now 15Hz to 80Hz..... 18

Figure 3.5 Results of data conditioning. (a) A vertical slice displaying the reflector amplitude of the original volume. (b) A vertical slice displaying the reflector amplitude of an uncompensated spectrally balanced volume. (c) A vertical slice showing the reflector amplitude of a compensated spectrally balanced seismic volume. From (c), improvement of reflectors amplitude appears to be mainly above Woodford horizon and below Hunton horizon. The green arrows compare results between raw data and a

spectrally balanced data. The blue arrows compare results from an uncompensated spectrally balanced data and a compensated spectrally balanced data at far offsets. 19

Figure 3.6. Schematic criteria for interpreting high-frequency cycles and their bounding surfaces based on Gamma Ray Parasequences (GRP). Regressive surfaces (rs) correspond with the turnaround point where stacked upward-decreasing GRP change to upward-increasing GRP. Flooding surfaces (fs) correspond with the turnaround point where stacked upward-increasing GRP change to upward-decreasing GRP. ... 21

Figure 3.7. Stratigraphic column of (a) and (b) complete Woodford section of two wells about 14km away from the (c) Speake Ranch outcrop profile. Well-log gamma-ray correlation of two wells (a) and (b) clearly correlates with the outcrop (c). The long arrows are 3rd order sequences while the small arrows are 4th order parasequence. The dotted red lines separate the Woodford Shale subdivisions, the green line is the maximum flooding surface across the wells. The average vertical thickness of the Woodford Shale penetrated by the wells is approximately 107 m (350 ft). (modified from Galvis et al., 2018). 22

Figure 3.8. A plot of Young’s modulus vs. Poisson’s ratio for two wells penetrating the upper, middle and lower Woodford Shale. The trend along the arrow shows a clear distinction for three Woodford sections with the cherty formation in the middle Woodford exhibiting the highest Young’s modulus value. 24

Figure 3.9 A summary diagram showing how seismic inversion first computes reflection coefficients (deconvolves the data) and then intergrates them to estimate the impedance. 26

Figure 3.10. A workflow showing steps involved in a model based inversion algorithm (Alali et al., 2016). 26

Figure 3.11 The zero-phase wavelet (a) time response and (b) magnitude response of the statistical wavelet extracted from the seismic volume using a commercial software. 27

Figure 3.12. Log correlation of well ‘NER’. The synthetic trace computed from the well logs and the seismic wavelet is shown in blue. The measured seismic amplitude data is in red. The correlation between the two traces is 0.968 for time range 1770 ms to 1900 ms. 29

Figure 3.13. A display of the background (0-10 Hz) low frequency impedance model constructed by kriging the values measure at three wells honoring structure. 30

Figure 3.14 (a) Woodford Shale lithology pattern analyzed by Galvis et al. (2018) for the Woodford outcrop in Ardmore, Oklahoma. (b) The proposed complete Woodford Shale anisotropic model adopted from the geological model. Two symmetries VTI and HTI effectively delineate and describes each subdivision (upper, middle and lower Woodford Shale). 35

Figure 3.15 A schematic of the two symmetries used for the anisotropic model. Left: Vertical Transverse Isotropic (VTI) medium, its symmetrical vertical and horizontal velocities (V_0 and V_{90}) along the vertical axis and elastic constants in matrix format. Right: Horizontal Transverse Isotropy (HTI) medium, its symmetrical velocities along the horizontal and its elastic constants in matrix format. 36

Figure 3.16. A cartoon describing different types of rock media and their symmetry (Lynn, 2018). 37

Figure 3.17 Elemental tensor components of a 3-D model. 38

Figure 3.18. A display of the trace amplitude as a function of offset for a representative prestack migrated CRP gathers. The red line indicates the top Meramec horizon, the green line indicates the top Woodford Shale, and the blue the top Hunton Group. Note the decrease in amplitude with increasing offset for the top Woodford shale horizon. 43

Figure 3.19. Display of the two major HTI anisotropy factors; vertical aligned fractures (left) and unequal horizontal stress (right) controlling azimuthal velocity variation in seismic reflectivity within the Woodford Shale formation. 45

Figure 3.20. (a) The reflection coefficients for Model A (change in $\gamma=0$, $\epsilon=0$ and $\delta=-0.1$) as a function of azimuth, ϕ for 0, 30, 60 and 90 degrees. (b) The reflection coefficients for Model C (change in $\gamma = -0.15$, $\epsilon=-0.05$ and $\delta=-0.05$) as a function of azimuth angle for incident angles $\theta =10, 20, 30$ and 40 degrees. ... 48

Figure 3.21.(a) The reflection coefficients for Model B (change in $\delta=-0.1$) as a function of azimuth, ϕ for 0, 30, 60 and 90 degrees. (b) The reflection coefficients for Model B (change in $\delta = -0.1$) as a function of azimuth angle for incident angles $\theta =10, 20, 30$ and 40 degrees. 48

Figure 3.22. (a) The reflection coefficients for Model C (change in $\epsilon= -0.1$) as a function of azimuth, ϕ for 0, 30, 60 and 90 degrees. (b) The reflection coefficients for Model C (change in $\epsilon = -0.1$) as a function of azimuth angle for incident angles $\theta =10, 20, 30$ and 40 degrees..... 49

Figure 3.23. (a) The reflection coefficients for Model D (change in $\gamma = -0.15$, $\epsilon=-0.05$ and $\delta=-0.05$) as a function of azimuth, ϕ for 0, 30, 60 and 90 degrees. (b) The reflection coefficients for Model C (change in $\gamma = -0.15$, $\epsilon=-0.05$ and $\delta=-0.05$) as a function of azimuth angle for incident angles $\theta =10, 20, 30$ and 40 degrees. 49

Figure 3.24 A schematic representation of a 2D curvature. Synclinal features have negative curvature, anticlinal features have positive curvature, and planar features have zero curvatures (Modified from Roberts, 2001)..... 51

Figure 4.1 Complete Woodford Shale lithology (gamma-ray) log correlation using 3rd order cycles (long red and blue arrows) across three (3) wells (BOB, WER, and NER) in the study area and the fourth gamma-ray log from the Speake Ranch outcrop. Correlating lithologies using Gamma-ray Parasequences, GRP (small blue and red arrows), all the logs approximately as the subdivisions are bounded by the green line. The maximum flooding surface (black lines) is easily identified in the middle Woodford Shale for both profiles and the subdivisions (separated by green lines) are identified as a complete 4th order sequence..... 54

Figure 4.2 Woodford Shale lithology (Gamma-ray) log correlation across eight (8) wells in the study area. The topmost formation is the Osage group and Hunton formation at the base. Flattened on top of upper Woodford Shale and segmented as upper, middle and lower (blue, cyan and green). The Woodford Shale formation has an average thickness of 100ft and the condensed section (the red dash lines) is seen in the middle Woodford correspond to the global Frasnian-Famennian boundary..... 55

Figure 4.3 A cross-plot of Young’s modulus and Poisson’s ratio for well ‘WER’ with datapoints from the upper, middle and lower Woodford formation. There is an inverse relationship between the two parameters, but more importantly, the subdivisions are clearly delineated. The middle Woodford Shale having the highest Young’s modulus value is the stiffest of the three Woodford Shale sections..... 57

Figure 4.4 A cross-plot of Young’s modulus against Poisson’s ratio for well ‘BOB’. The two histograms clearly delineate the middle Woodford Shale as the stiffest and the least ductile. The stiffness attributes points to the fact that it is the most fractured interval of the three Woodford Shale formations. 58

Figure 4.5 Seismic inversion analysis window. The correlation between the trace and the synthetic is quite good and error analysis verifies that with an error margin of 6.67% during the inversion process. In the error analysis column, the black curve is the initial model, the blue curve is acoustic impedance from well-logs, and the red curve is the synthetic curve. After ten (10) iterations, the error was minimized to 6.67%. 60

Figure 4.6 A seismic resolution study of the Woodford Shale using Widess’s (1993) wedge model showing that the limits to vertical resolution for a 45 Hz wavelet is about 100 ft for a velocity of 11,000 ft/s. Fortunately, after spectral balancing, our data has useful information up to 80 Hz, thereby increasing the resolution..... 62

Figure 4.7 A vertical view of the seismic volume line BB’ shown in inserted map (top right). From the traces, the Woodford Shale is clearly identified as a strong trough (the cyan pick) overlying the Hunton

formation strong peak (the red pick). It corresponds that the thickness of the entire Woodford Shale is approximately $\lambda/5$ 62

Figure 4.8 A vertical slice through the P-impedance volume (along line CC' in inserted map) connecting wells OPD, NER, and WER. The lower impedance of the Woodford Shale underlies the Osage formation and overlies Hunton group. The inversion result was able to resolve the entire Woodford Shale but does not clearly delineate the middle Woodford Shale or other subdivisions..... 63

Figure 4.9 A plot showing the difference between the measured seismic data and the synthetic traces corresponding the inverted P-impedance model for the line connecting wells 'NER' and 'WER'. The amplitude scale is the same as the seismic line shown in Figure 4.11 and indicates a very small residual. 64

Figure 4.10 Time structural map of top of Woodford Shale formation. The depth of the top Woodford increases from northeast to southwest. Location of profiles BB' and CC' discussed in figures 4.14 and 4.15. This figure corresponds to the trend seen in the Anadarko basin geology literature. 64

Figure 4.11 (A) An isochron map of Woodford Shale. Generally, the formation is thicker within the east area of the map. (B) Map of the study area showing location of the wells, the small black rectangle is the seismic volume area (C) P-impedance stratal slice through the middle Woodford Shale approximately 15 ms below the top Woodford Shale horizon. The black polygon indicates an area of low impedance which may be due to several causes, one of which is the area being highly fractured. The region within the polygon will be further investigated using AVAz analysis. 66

Figure 4.12 A seismic CDP gather time-window at well 'NER' location showing the Woodford Shale time (1840ms) interval (green line) and the trace amplitudes used for AVAz analysis. Notice the amplitude of the Woodford reflection in blue colour reduces as the offset increases. The magnitude of the decline is higher than that of Hunton below. 69

Figure 4.13 A AVAz window analysis at well 'NER' showing the predicted AVAz curves from Ruger approximation matching the data-points of the seismic traces at well 'NER". Amplitude of the reflection coefficient is plotted against azimuth. The predicted curve represents the approximation of the reflection coefficient along azimuth for different incident angles (i.e. 0° , 7° , 14° , 21° , 28°). Notice the separation of the curves and the sinusoids pattern along azimuth compared with subsequent figures. The magnitude of the B_{aniso} is estimated at 16000. The isotropy azimuth is 80° 70

Figure 4.14 A seismic CDP gather time-window at well 'OPD' location showing the Woodford Shale time (1840ms) interval (green line) and the trace amplitudes used for AVAz analysis. Notice the amplitude of the Woodford reflection in blue colour reduces as the offset increases. The magnitude of the decline is higher than that of Hunton below. 71

Figure 4.15 A AVAz analysis window at well 'OPD' showing the predicted AVAz curve using Ruger approximation. Amplitude of the reflection coefficient is plotted against azimuth. The predicted curve represents the approximation of the reflection coefficient along azimuth for different incident angles (i.e. 0° , 7° , 14° , 21° , 28°). The data-points are fairly approximated by the curves. Notice the separation of the curves and the sinusoids pattern along azimuth. At this location, the B_{aniso} is estimated at 12840. The isotropy azimuth is 70° 72

Figure 4.16 A seismic CDP gather time-window at well 'WER' location showing the Woodford Shale time (1840ms) interval (green line) and the trace amplitudes used for AVAz analysis. Notice the amplitude of the Woodford reflection in blue colour reduces as the offset increases. The magnitude of the decline is higher than that of Hunton below. 73

Figure 4.17 AVAz window analysis at well 'WER' showing the predicted AVAz curves from Ruger approximation matching the data-points of the seismic traces at well 'WER". Amplitude of the reflection coefficient is plotted against azimuth. The predicted curve represents the approximation of the reflection coefficient along azimuth for different incident angles (i.e. 0° , 7° , 14° , 21° , 28°). Notice the separation of

the curves and the sinusoids pattern along azimuth. The magnitude of the B_{aniso} is estimated at 6240. The isotropy azimuth is -60° 74

Figure 4.18 Anisotropy inversion results. Stratal slice of the azimuthal isotropy, ϕ_{iso} with 0° north orientation (a) and anisotropic gradient B_{aniso} (b) of the Woodford Shale. The black polygon defines a zone where B_{aniso} is high and the ϕ_{iso} is in the E-W or NE-SW orientation. We hypothesize that the region within the polygon has higher fracture intensity, and perhaps a thicker middle Woodford Shale unit than other regions..... 76

Figure 4.19 Strata slice of anisotropy gradient B_{aniso} using a monochrome black color bar and opacity, overlain with azimuthal isotropy ϕ_{iso} . Areas that appear black are relatively isotropic. There is a correlation between the two volumes as the bright region in the purple polygon matches region with a certain pattern of orientation in the ϕ_{iso} map and the locations of the three wells (located in the star symbols) drilled. The bright region has high magnitude fractures that are in the same orientation as the bitumen-filled fracture-sets seen in the outcrop. Interestingly, the three well locations were situated within the region highlighted. 77

Figure 4.20 A display of the vector plot of Woodford Shale. This is done by resampling the seismic azimuth isotropy and anisotropy gradient geometrically and applying it on 3D vector grid. The arrows indicate the orientation of the fracture or stress while the color of the arrow is the magnitude of the fractures at each location. Regions around well locations ‘OPD’, ‘NER’, and ‘WER’ have high anisotropy gradient compared to other locations. Hence, they have relatively thick middle Woodford formation with fracture-sets in the E-W or NE-SW orientation. 78

Figure 4.21 A display of the Woodford Shale vector plot co-rendered with anisotropy gradient volume. The bright regions correspond to where there is high gradient while the dim or dark regions are where there is low gradient. Notice that the direction of the vector plot (arrows) where in the bright regions are mostly in the E-W or NE-SW orientation while in the dark regions, the fracture-sets are mostly N-S or NW-SE direction. From previous studies, the E-W and NE-SW fracture-sets in the Woodford Shale are the primary natural fracture-sets embedded with bitumen (Ghosh, 2017)..... **Error! Bookmark not defined.**

Figure 4.22 A vector plot of Woodford fracture intensity co-rendered with anisotropy gradient and azimuthal isotropy. Here, the well locations are situated around the bright area, and also where the arrows are in the E-W and NE-SW direction, and the magnitude are high. In the background is the ϕ_{iso} orientation between 60° - 90° 80

Figure 4.23 A display of the Woodford Shale vector plot underlying curvature co-rendered attributes, K_{max} and K_{min} . The red regions are prominent for dome and anticline features from K_{max} attribute, the blue zone corresponds to regions with bowl and synclinal features from K_{min} attribute. Majority of the bright areas i.e. fracture swarms areas lie within the flexure (red) features highlighted by the yellow arrows. Hence, investigation of fracture intensity using seismic surface attributes is feasible. 81

ABSTRACT

Information on the geomechanical condition of the vertical and lateral heterogeneities in unconventional reservoirs is critical in designing completion programs for targets such as the 100 ft thick, 10,000 ft deep Woodford Shale. To address this problem, I use the azimuthal and offset information provided by a modern wide azimuth 3D seismic survey to map the variation in the elastic properties of the formation.

In the absence of direct measures of natural fractures in the borehole, I used measures of natural fractures in a suite of Gamma-Ray Parasequences (GRP) where the Woodford Shale outcrops 150 miles to the southeast of the seismic survey. I then correlated the outcrop GRPs to those seen in three wells in the Anadarko Basin target area to generate a lithology stack of the upper, middle, and lower Woodford Shale subdivisions. Stiffness analysis results from Young's modulus and Poisson's ratio crossplots indicated the middle Woodford to be the stiffest of the three subdivisions, consistent with the higher chert content seen in the outcrop.

Without access to shear wave logs, I limited my inversion to poststack analysis, which showed the Woodford shale to be a low-impedance unit across the study area. Even after spectral balancing which increased the bandwidth 50% from 15-42 Hz to 12-84 Hz, there was insufficient resolution to separate the three Woodford subdivisions. Nevertheless, the seismic data were sufficiently good to apply modern AVAz analysis to estimate the anisotropy gradient (B_{aniso}) and azimuth (ϕ_{iso}). Using the outcrop where the great majority of the natural fractures are confined to the chert-rich, laminated middle Woodford as our model, we assume the same fracture pattern continues into the area of the 3D seismic data. The AVAz analysis shows regions with high fracture intensity with orientations $\sim 90^\circ$ (E-W) and $\sim 50^\circ$ (NE-SW) corresponding to those identified in the Woodford Shale outcrop with bitumen filling. Because we are measuring the AVAz effect for the Woodford

Shale as a unit, the areas of higher anisotropy indicate either more intense fracturing, a thicker middle Woodford, or both.

1 INTRODUCTION

Over the past couple of decades, the oil industry has evolved from considering organic shales to play the restricted roles of source rock or seal to treating them as a self-source self-sealed unconventional resource. State-of-the-art technological advancements coupled with a good understanding of the pore network and geomechanical properties have made exploitation of the Woodford Shale resource more economically viable than most conventional resource plays (Slatt et al., 2013). A successful hydraulic fracturing completion project on shale cannot be achieved without understanding or incorporating its' anisotropic nature (Higgins et al., 2008). Crucial to exploration of an economically viable unconventional shale resources is a robust and high-density seismic volume (wide-azimuth prestack migrated gathers) with an appropriate suite of well-logs.

The shale's geomechanical condition, which is dependent not only on lithology but on the regional and local stress regime, along with TOC and porosity, are critical to the optimization of unconventional shale resource plays (Rickman et al., 2008). Using outcrops, Ghosh (2017), and Molinares (2019) used the geometry, placement and infill of the resultant fracture sets to understand the chronology of regional and local stress acting within the local environment. Using palynomorphs, geochemical proxies and well-log signatures, Urban (1960), Sullivan (1985), Hester et al. (1990), and Lambert (1993) subdivided the Woodford Shale into the upper, middle and lower sections. Becerra (2017), Galvis (2017), and Ghosh (2017) applied laboratory techniques such as X-ray diffraction (XRD), X-ray fluorescence (XRF) and scanning electron microscopy (SEM) to further discriminate between the two dominant lithologies in the Woodford, chert and siliceous clay-organic shales (Figure 1.1). Given the response of these two lithologies to natural fracturing, they dubbed them hard (clay rich) and soft (chert rich) beds, or more precisely stiff and less-stiff beds. Galvis (2017) used outcrop samples from Ardmore, Oklahoma, modeled

how cyclicity and thickness of the two beds influences the resulting fracture intensity (Figure 1.2). He proposed that the fracture-set network also determines the reservoir and completion quality (RQ and CQ) of the Woodford formation and postulated that the ideal landing zone for horizontal wells is one with an equal percent of RQ-CQ quality.

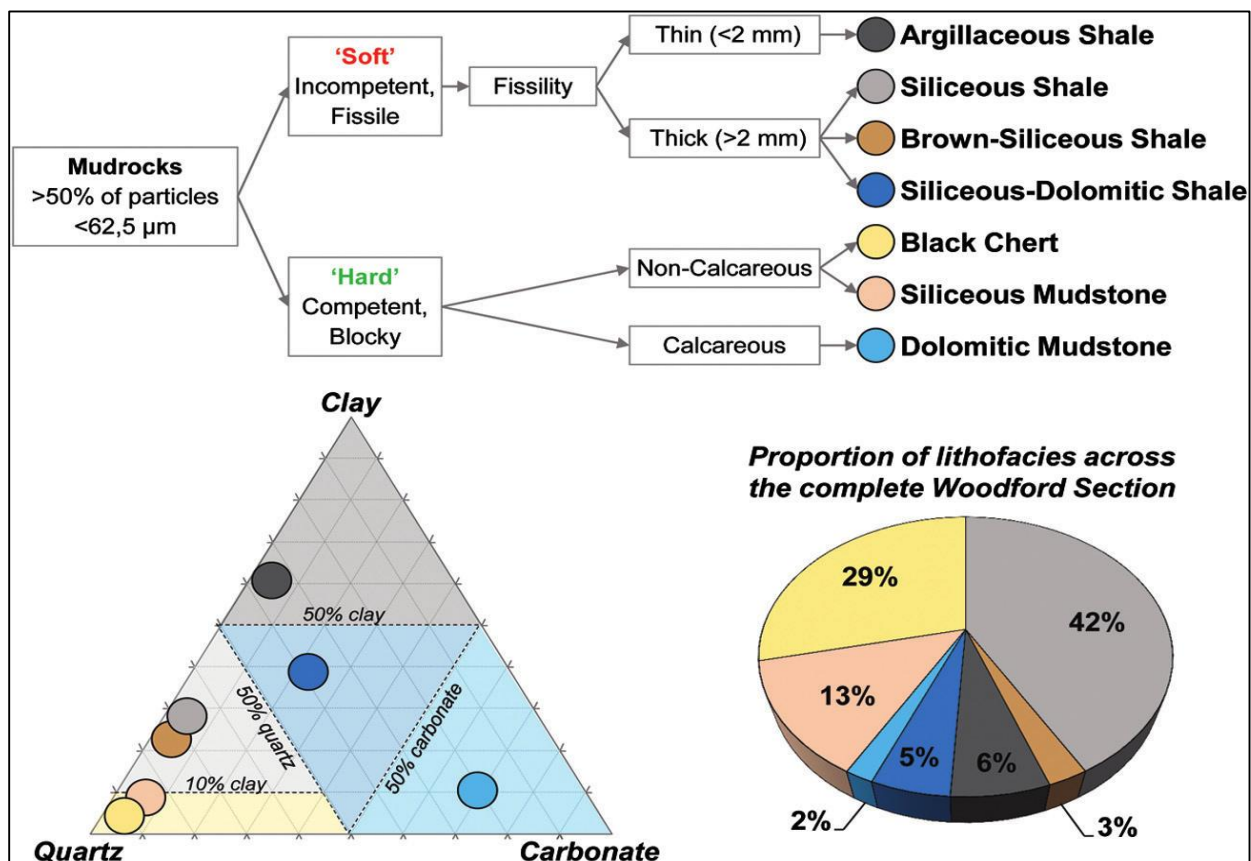


Figure 1.1 Field-based lithofacies classification scheme for Woodford Shale mudrock. The first criterion distinguishes between hard and soft beds; then compositional and textural descriptors are added to the rock name. Seven lithofacies were recognized within the Woodford Shale at the Speake Ranch outcrop. The mineral composition of the lithofacies is illustrated in the ternary plot and reveals that most of the Woodford mudrock plot along the quartz-clay axis. The pie chart suggests siliceous shales, cherts, and siliceous mudstones as being the most abundant lithofacies, which account for more than 80% of the entire lithological record (from Galvis et al., 2018)


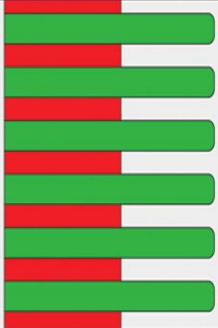
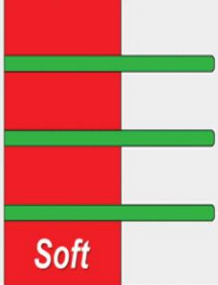
Stacking Pattern	Characteristics	Assumptions of RQ and CQ
Model 3 	Hard >>> Soft <ul style="list-style-type: none"> * Thick chert beds (8-12 cm) * Very thin shale beds (<3cm) * Moderate organic contents (<5%) * Very high hardness and brittleness * Moderate natural fracture intensity 	Better CQ – Poor RQ <ul style="list-style-type: none"> * Fracability, high fracture conductivity * Efficient proppant placement * Low potential as a hydrocarbon source rock (low expulsion efficiencies) * Moderate to poor matrix porosity
Model 2 	Soft ≈ Hard <ul style="list-style-type: none"> * Homogeneous bed thickness (~4 cm) * High frequency, thin interlayering * Organic-rich shales and brittle cherts * Moderate Hardness * Very high natural fracture intensity 	Balance between RQ and CQ <ul style="list-style-type: none"> * Storage capacity in fractures of cherts and in the shale matrix (porosity) * Development of more complex artificial fracture networks * Excellent matrix-fracture connectivity * Efficient proppant placement
Model 1 	Soft >>> Hard <ul style="list-style-type: none"> * Thick shale beds (>10cm) * Few thin scattered chert beds (<3cm) * Excellent organic contents (8-20%) * Low Hardness (high ductility) * Very low density of natural fractures 	Better RQ – Poor CQ <ul style="list-style-type: none"> * Super high potential as a hydrocarbon source interval (with matrix storage) * High ductility, Low fracability * Poor reservoir connectivity * Proppant embedment

Figure 1.2 Summary of hypothetical reservoir quality (RQ) and completion quality (CQ) as interpreted based on the stacking patterns between soft and hard beds. Model 1 is typical of the lower Woodford member in which thick soft beds dominate. Model 2 presents the optimal balance between RQ and CQ, and it is characterized by the 50/50 soft-to-hard ratio made of thin beds. Model 3 illustrates a predominance of thicker hard beds, which is very typical of the upper Woodford member (from Galvis et al., 2018).

From a seismic method perspective, the presence of fine laminar, fissile shale beds and fractured non-fissile cherty beds in the Woodford Shale makes it an anisotropic medium (Sayers, 2004, Zhang, 2019). In the absence of vertical fractures, measurements of elastic and geomechanical properties of Woodford Shale is polarized along an axis of symmetry making it transversely isotropic. About four established factors contribute to the anisotropic nature of organic shales: (1) the intrinsic anisotropic nature of shales is attributed to preferred aligned plate-like minerals in organic shales (Sayers, 1994) and (2) the stacking of a large number of fine shale strata whose individual layer thickness is far lower than the seismic wavelength and cannot be resolved with seismic reflection data (Backus, 1962). Shale's geomechanical response to regional stress (tectonics) is another dependent factor to its anisotropic nature. These two major factors play major roles in influencing and optimizing the expected ultimate recovery (EUR) of the Woodford Shale (Goodway and Perez, 2010).

In this study, I relied on suites of well-logs and 5D prestack P-wave seismic data recorded to delineate and characterize the regions with relatively thick RQ-CQ intervals (the middle Woodford Shale) within the Woodford Shale. Seismic reflection data indirectly provides impedance contrast maps and other petrophysical properties to characterize the lithology of interest through seismic inversion. However, data conditioning procedures are prioritized to optimize signals recorded in the seismic volume and avoid pitfalls associated with seismic data quality (Marfurt and Alves 2015). Procedures like migration-stretch-compensation were applied to preserve far offset trace amplitude information (Patel et al., 2019). I then used Ruger's (2002) technique to analyze offset and azimuthal information to derive an anisotropy gradient and orientation to predict fracture intensity and the orientation within the target formation.

2 GEOLOGICAL BACKGROUND

Understanding the geology provides information about the depositional environment, basin evolution and the materials deposited. For this study, discussions on the structural background of the study area (Anadarko basin) will extend to the Arkoma basin formation as it relates to time of deposition of the Woodford Shale formation. Generally, the focus is on the geological (structural and stratigraphic) background of the Anadarko basin from late Cambrian age to Carboniferous time within the Paleozoic era.

2.1 Structural Setting

The Anadarko basin is seated within the northern flank of the late Proterozoic to the early Paleozoic of the southern Oklahoma aulacogen. Regarded as the deepest sedimentary basin in the North American craton, the Anadarko basin accommodates over 40,000 ft of Paleozoic formation made up of igneous and sedimentary rocks from Cambrian to Permian (Ham and Wilson, 1967). Due to its complex structural evolution, Perry (1989) divided the Anadarko basin formations into four periods, namely: i) Precambrian consolidation, ii) Late Precambrian to middle Cambrian aulacogen development, iii) Cambrian to early Mississippian development of the southern Oklahoma trough, and iv) late Paleozoic events within the Anadarko basin northwest of the trough.

According to Ham and Wilson (1967) and Denison (1982), intrusive and metamorphic rocks of late Precambrian to early Cambrian age underlay the Anadarko basin. These inferences were made after drilling into the basin within the faulted blocks around the southern and south-eastern margin of the basin. The structural nature of the Cambrian complex is similar to that of a linear rift or the southern Oklahoma aulacogen (SOA) formed as a result of a plate tectonic triple junction (Burke, 1977).

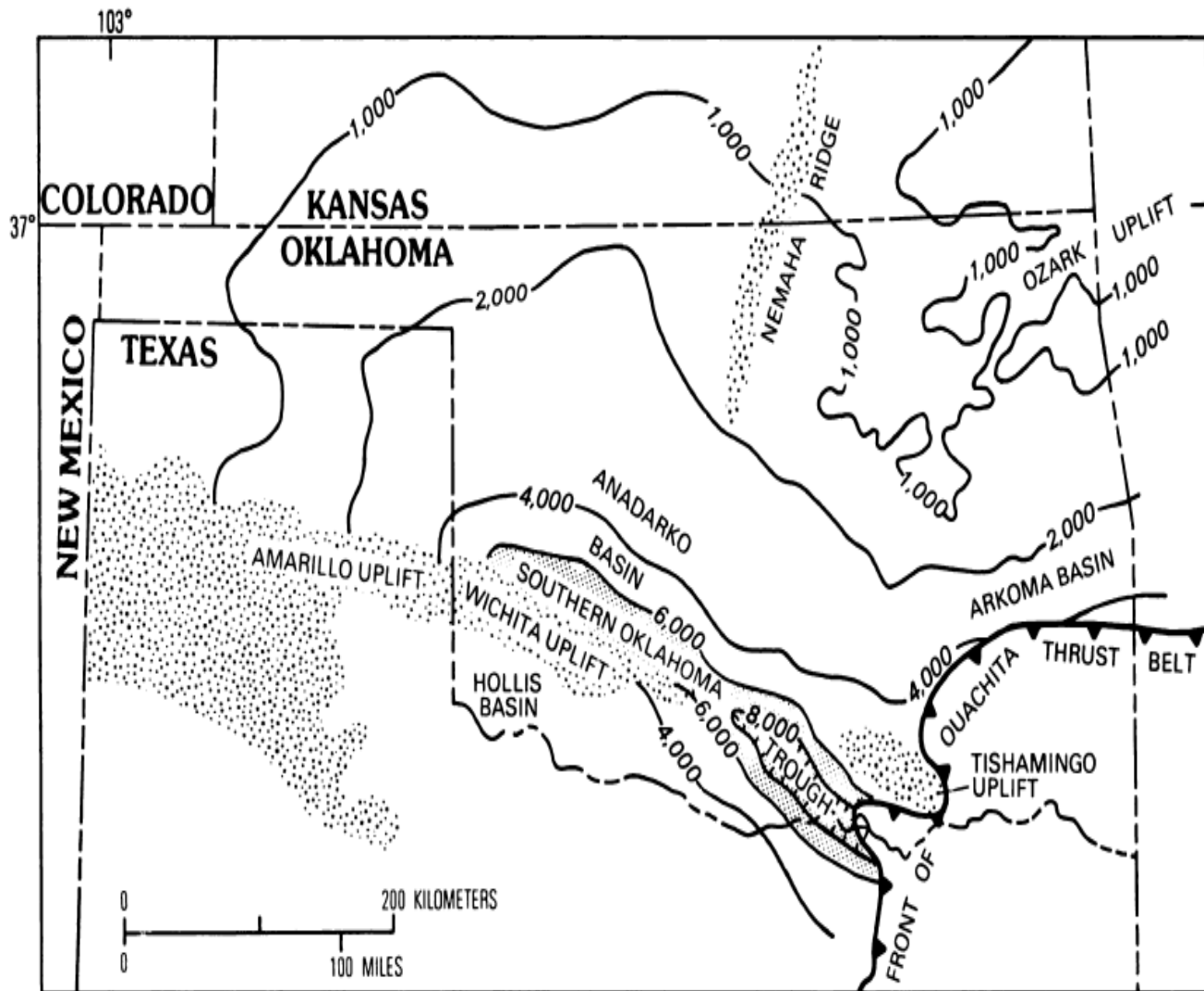


Figure 2.2.1 Isopach map of Cambrian Timbered Hills and upper Cambrian through lower Ordovician Arbuckle Groups, Oklahoma and western Texas. Contour interval, 1,000 and 2,000 ft; contour hachured to indicate closed low. Stippling represents areas in which Cambrian and lower Ordovician rocks are deeply eroded or removed to basement. Screen pattern represents depocentral area of southern Oklahoma trough. Modified from Gatewood (1978).

[Figure 2.1](#) describes the north section of the older aulacogen relatively lying under the southern Oklahoma trough which corresponds to a sharp southward thickening between Cambrian and lower Ordovician carbonate rocks (Gatewood, 1978). Along the northern flank of the SOA is where the Anadarko basin is situated.

During the early Precambrian period, the aulacogen phase began to develop as the failed arm of the triple junction cut through the North American craton as the proto-Atlantic Ocean continues to open. The aulacogen experienced subsidence and cooling as the rifting phase ceased to form the southern Oklahoma trough ([Figure 2.2](#)). During the rifting phase, over 11,000 ft of Cambrian through lower Devonian carbonate rocks were deposited along the aulacogen axis between the Wichita and south-western Arbuckle Mountains (Ham, 1973). Feinstein (1981) modelled and proposed a decreasing rate of subsidence over time from Cambrian to Early Mississippian time along the southern Oklahoma trough.

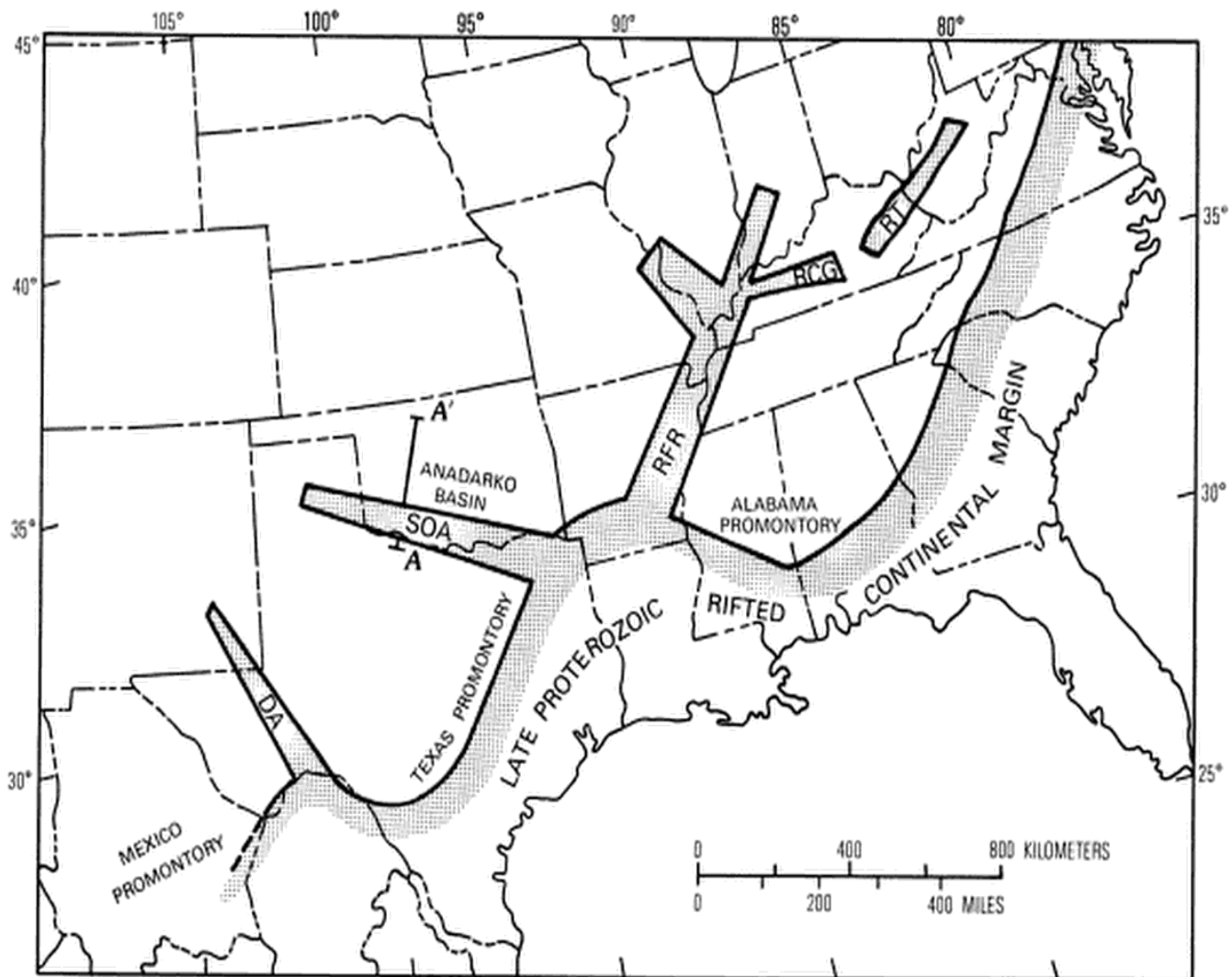


Figure 2.2.2 A Paleotectonic map highlighting tectonic activities such as continental margins and rift; during the late Proterozoic and early Paleozoic time. DA, Delaware aulacogen; RCG, Rough Creek graben; RFR, Reelfoot rift; RT, Rome trough; SOA, southern Oklahoma aulacogen. Modified from Keller and others (1983).

The late Mississippian time witnessed the beginning of the fourth phase of tectonism. During this period, parts of the Anadarko basin in central and western Oklahoma on the northern flank of the Cambrian rift began to evolve asymmetrically as a result of structural inversion from the collision of the north American plate with Gondwana. It also resulted in the Ouachita orogeny. There have been valid arguments on what structural features are associated to this phase of tectonism.

2.2 Stratigraphic Setting

The black Woodford Shale deposited during the late Devonian unconformably overlies the Hunton formation. It occupies the upper Devonian to lower Mississippian period and it is an important source rock in the region (Webster, 1980). With thickness ranging from 50 – 150 ft for the most part of the Anadarko basin, it abruptly thickens around the fault blocks of the frontal Wichita fault system south of the Anadarko basin. Variation in thickness of the Woodford formation in the study area and in most of Oklahoma can also be due to subaerial erosion of the underlying Hunton formation which created a karsted unconformity (Amsden, 1975). In some part of north eastern Oklahoma, the Woodford Shale directly overlies the Sylvian shale due to complete erosion of the Hunton formation (Amsden, 1975). A stratigraphic column as seen in [Figure 2.3](#) illustrates the pattern of deposition of the Woodford across parts of Anadarko basin. Another unique feature is the cyclicity of hard cherty and fissile-siliceous shales beds in the middle Woodford formation due to local tectonics and mainly due to a combination of 3rd order and 2nd order eustatics (Abousleiman and Slatt, 2011). Gathering Woodford samples from the Wichita fault blocks, Cardott and Lambert (1985) used vitrinites reflectance analysis to prove that the Woodford formation was buried not more than 1 million years (approximately 1.2 miles).

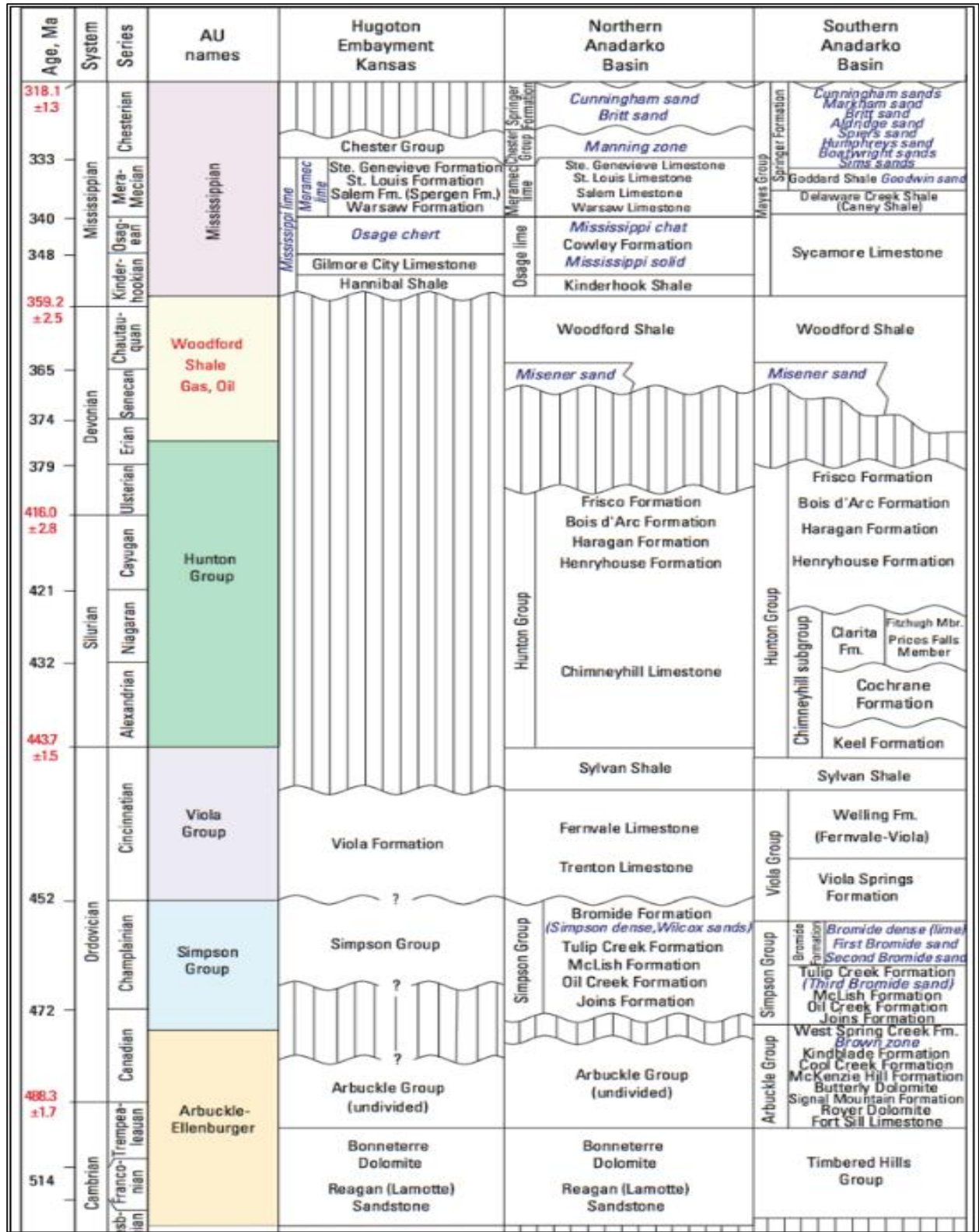


Figure 2.3 Stratigraphic column of the Woodford Shale across the Anadarko Basin area. (United States Geological Survey, USGS).

Comer and Hinch (1987), Roberts and Mitterer (1992), and Fishman et al., (2013) all identified two distinctive lithologies (shales and cherts) in terms of their geochemical and petrophysical properties within the Woodford formation. Using palynomorphs, geochemical proxies and well-log signatures, Urban (1960), Sullivan (1985), Hester et al. (1990), and Lambert (1993) categorized the Woodford Shale into three sections, namely; upper, middle and lower Woodford Shale. The condensed section is within the middle Woodford Shale; hence it is the highest TOC interval. The presence of phosphate nodules is used as an indicator for the upper Woodford interval (Hester et al., 1988)

Mississippian age formations in the North American system can be classified into four major stages, from the earliest: Kinderhookian, Osagean, Meramecian and Chesterian as seen in Figure 2.3 Within the study area, north of the Anadarko basin, the top of the Woodford Shale can be grouped as a Kinderhookian aged formation underlying the Osagean rocks which is placed in Osagean time (Bennison, 1956; Curtis and Champlin, 1959. The Ouachita orogeny formed as a result of the collision between the North American plate and Gondwana (Kluth, 1986). It is linked to the formation of the Meramecian units which truncates the Osagean rocks to the south. Lastly, the latest Mississippian aged Chesterian rocks were deposited during the development of the Anadarko basin north of the aulacogen during the Mississippian-Pensylvanian tectonism (Curtis and Champlin, 1959).

2.3 Study Area

The study area is located north of the Anadarko Basin in Kingfisher county northwest Oklahoma ([figure 2.4](#)).

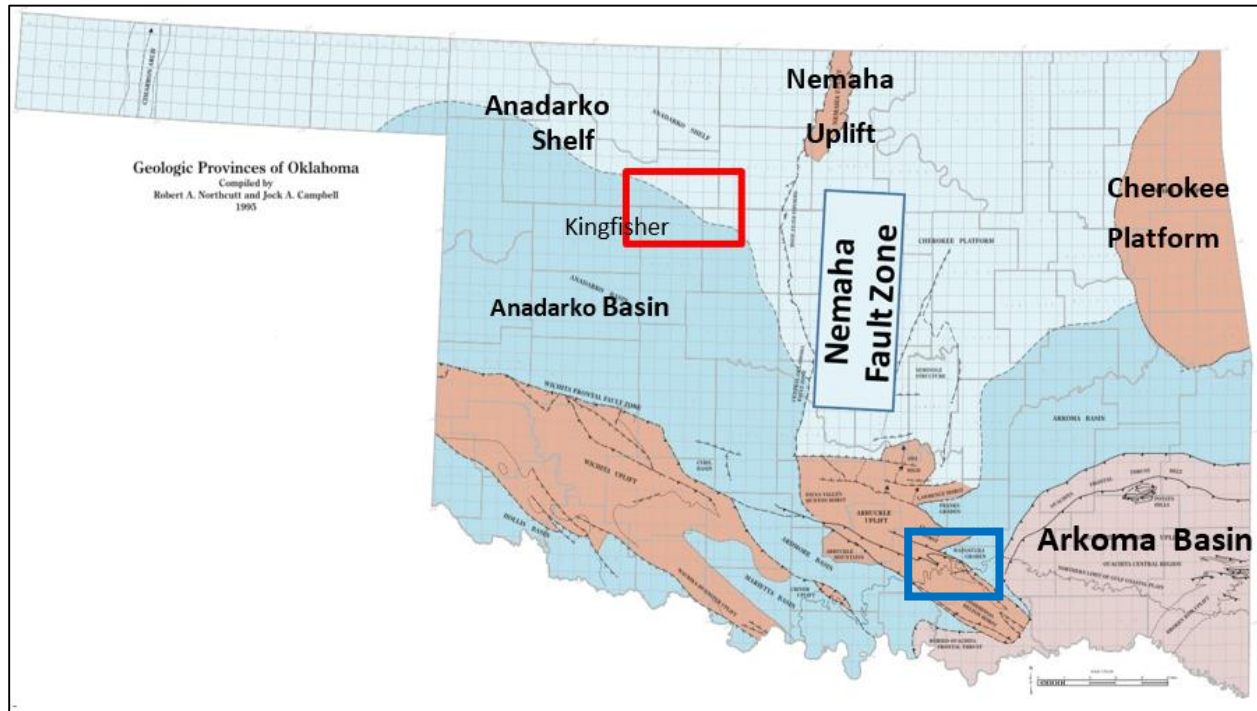


Figure 2.4 Map of Oklahoma showing location of the study area within the red rectangle and location of the complete section of the Woodford Shale outcrop within the blue rectangle about 156 miles away (Johnson,2008).

3 MATERIALS AND METHODS

3.1 Materials (data quality check and normalization)

I used eight (8) suites of well-log data, a prestack time-migrated seismic volume and a complete Woodford Shale outcrop analysis in this study (Figure 3.1). A 3D seismic prestack gather volume with offset and azimuth components (Figure 3.2) is used for amplitude variation for both poststack seismic inversion and amplitude variation with azimuth analysis. The lack of a shear log precluded computation of prestack inversion volumes.

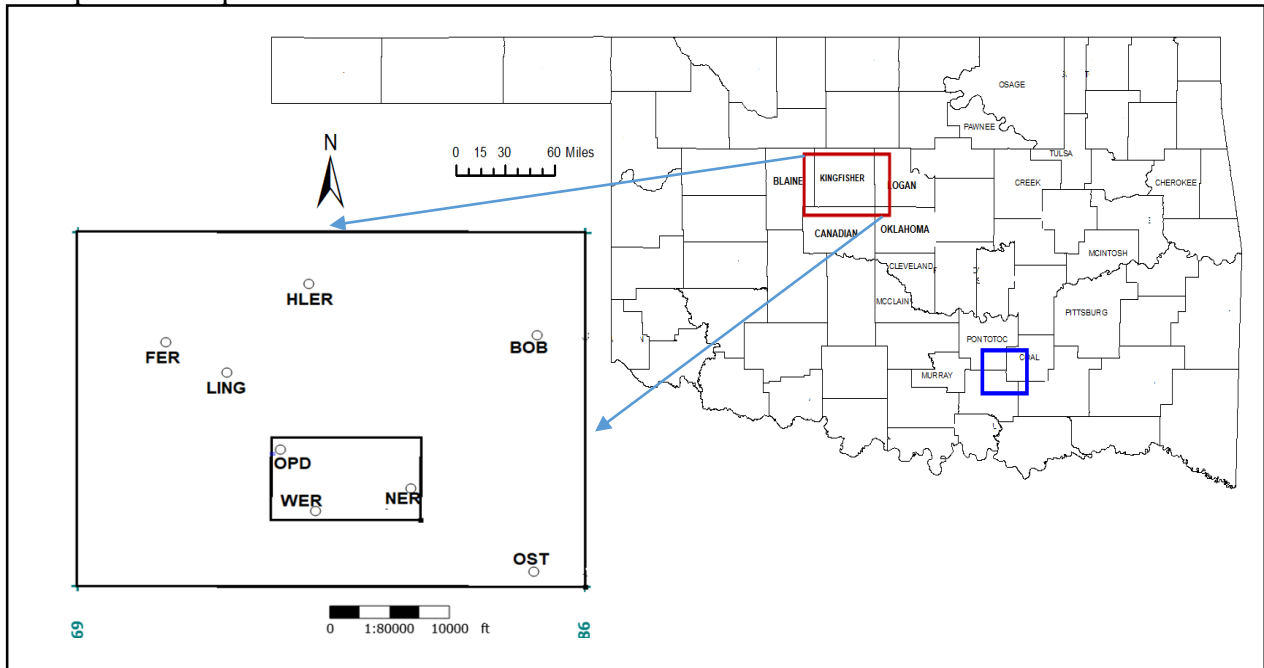


Figure 3.1 Locations of the all the wells within the study area (in the big black rectangle). Wells ‘OPD’, ‘WER’ and ‘NER’ are located within the seismic survey area (in the small black rectangle). The location of the reference outcrop is within the blue rectangle on the map.

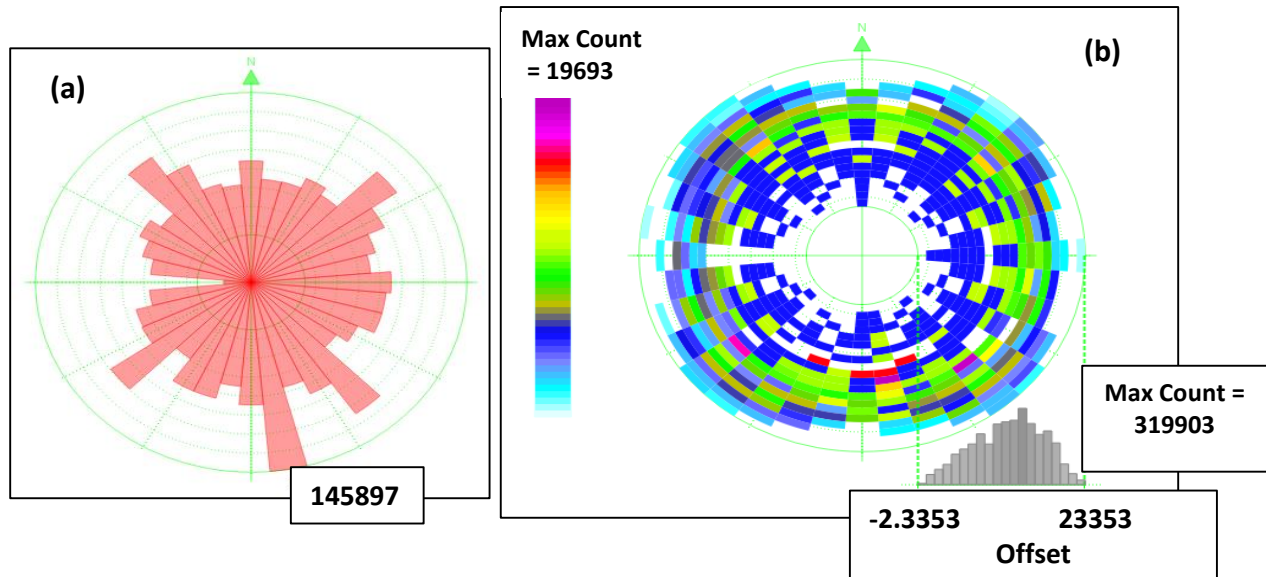


Figure 3.2 A display of the amount of trace per azimuth (a) and the amount of bins along each azimuth (b) in the seismic volume used.

3.1.1 Well-log Conditioning

Well-log data were also quality-checked (QC) for traces of high frequency coherent noise (spikes) in the log profiles. As seen in Figure 3.3, regular, repeated spikes identified in the sonic logs are due to malfunctioning of the logging tools (Burch, 2002). In order to eliminate this noise and also to preserve log information, a gentle smoothing harmonic function was applied. Few feet of missing log data due to malfunctioning of the operational logging tool were also observed in some of the logs. Hence, some intervals in the well-log were interpolated with available adjacent depth values.

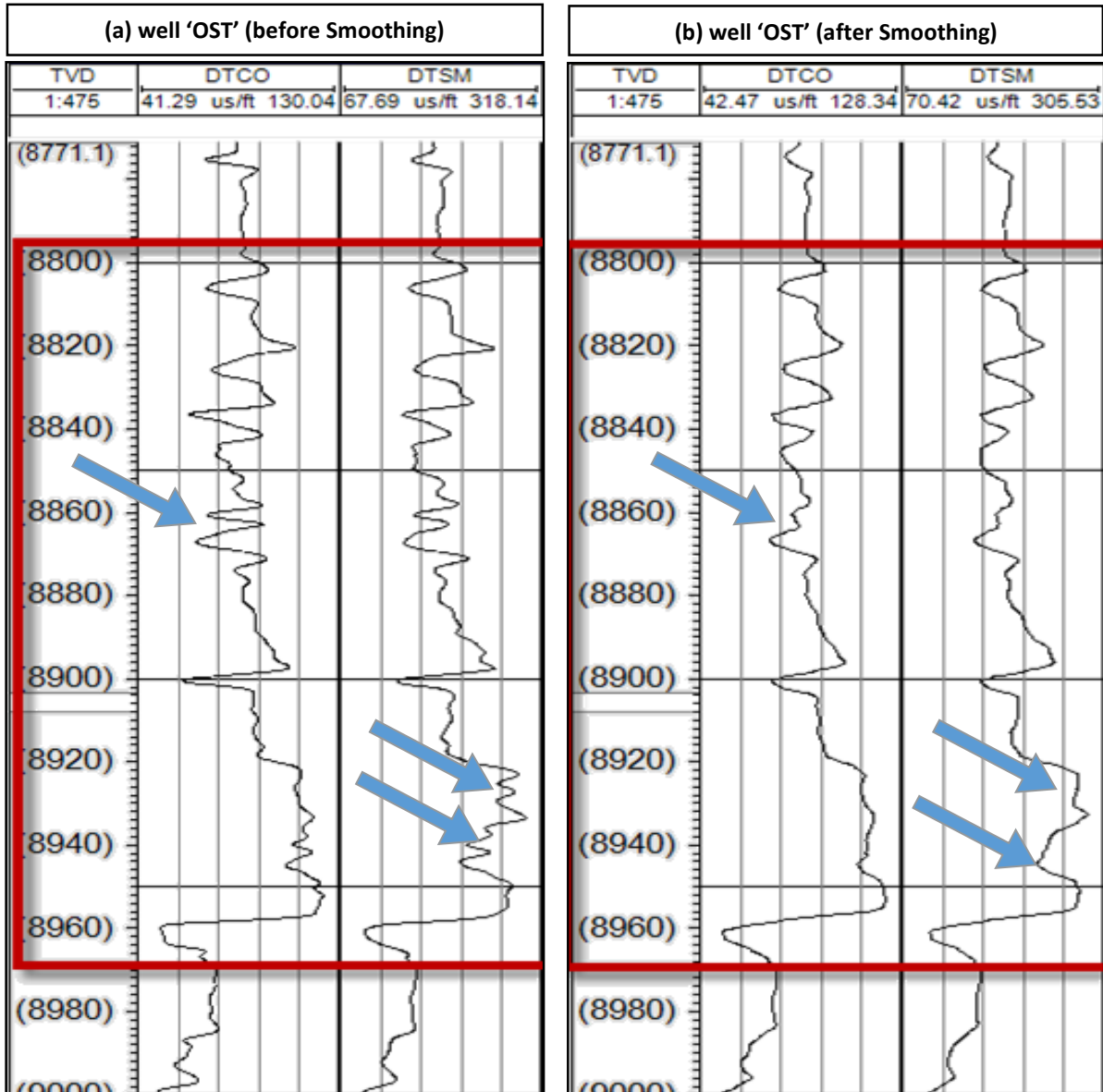


Figure 3.3 Well-log correction; (a) Repeated high frequency spikes noticed in the sonic shear and compressional log within the red box, highlighted by the blue arrows. (b) A reasonably smoothed sonic curve after applying harmonic filter to attenuate the coherent noise.

3.1.2 Seismic Data Conditioning

Seismic surveys are acquired and processed to image multiple objectives. In the absence of access to well control, or the understanding of the geology of the exploration objective, the seismic processor chooses parameters that produce an image that provides a good image of both the stratigraphy and tectonic features for the full sedimentary section. In contrast, the seismic interpreter usually has more focused objectives, sometimes tectonic, sometime stratigraphic, and in nearly all cases, for a specific reservoir. For this reason, we are able to improve upon the otherwise state-of-the-art processing provided by the service company. The first step taken is to compensate for amplitudes of far offset traces smeared or lost through migration stretch during normal moveout (NMO) correction by using a velocity model (Patel et al., 2019). Figure 3.4b and 3.4c compare result of a compensated and an uncompensated gather, reflectors in the far offset are improved in the compensated gather.

The next step is to investigate and improve the amplitude spectrum of the stacked seismic volume. The half-power bandwidth of the original data is 15-42 Hz. After spectral balancing I was able to increase the half-power bandwidth to 12-82 Hz, or almost double the original (Figure 3.3). Such balancing bolsters the amplitude of high frequency components so as to better resolve thin beds and provide more information within the interval of interest (Chopra and Marfurt, 2007) . Nevertheless, even with such improvement, there is little or no changes in amplitude or reflectors within the Woodford Shale formation interval (Figure 3.4c). Figure 3.4 compares the input data with the final output and shows an improved amplitude result after the two steps.

A trim statics correction was applied to the seismic volume to correct for misalignment of traces along offset and to correct for small errors in azimuthal/anisotropic imaging. Because the data were prestack time migrated using an azimuthally anisotropic velocity model, I am unable to use any residual moveout errors to estimate the velocity variation with azimuth (VVAz) analysis to find fracture intensity or the orientation.

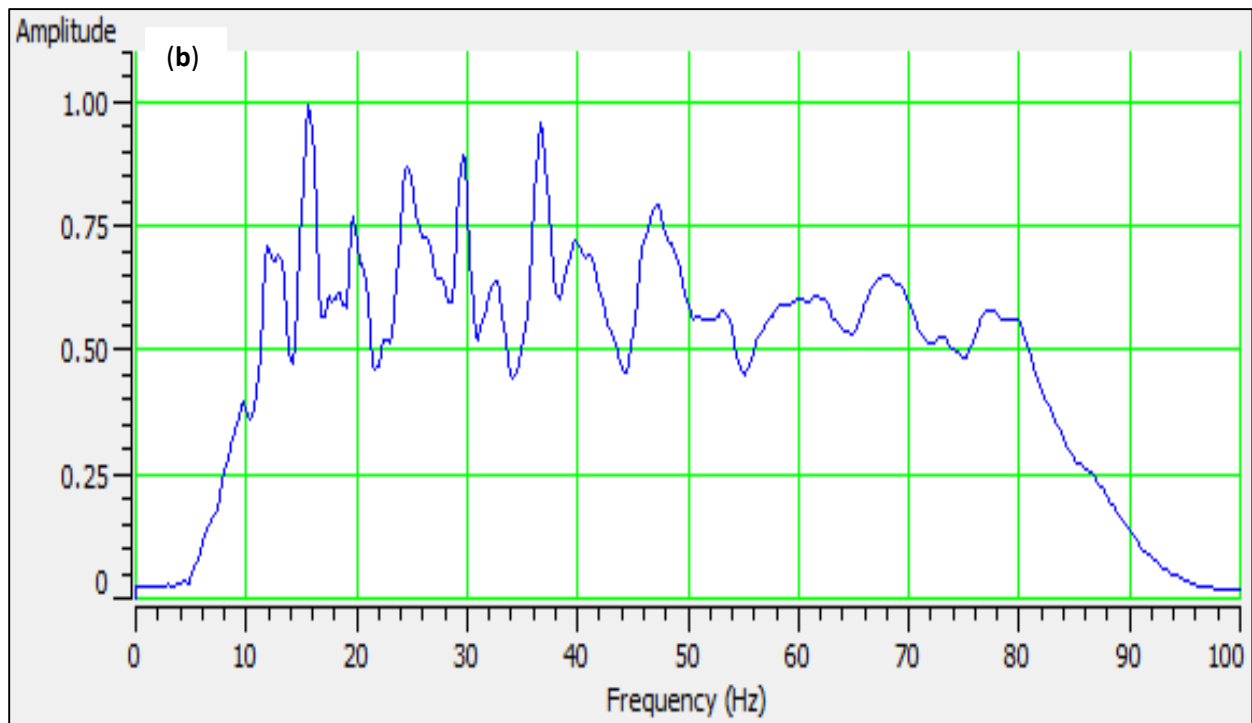
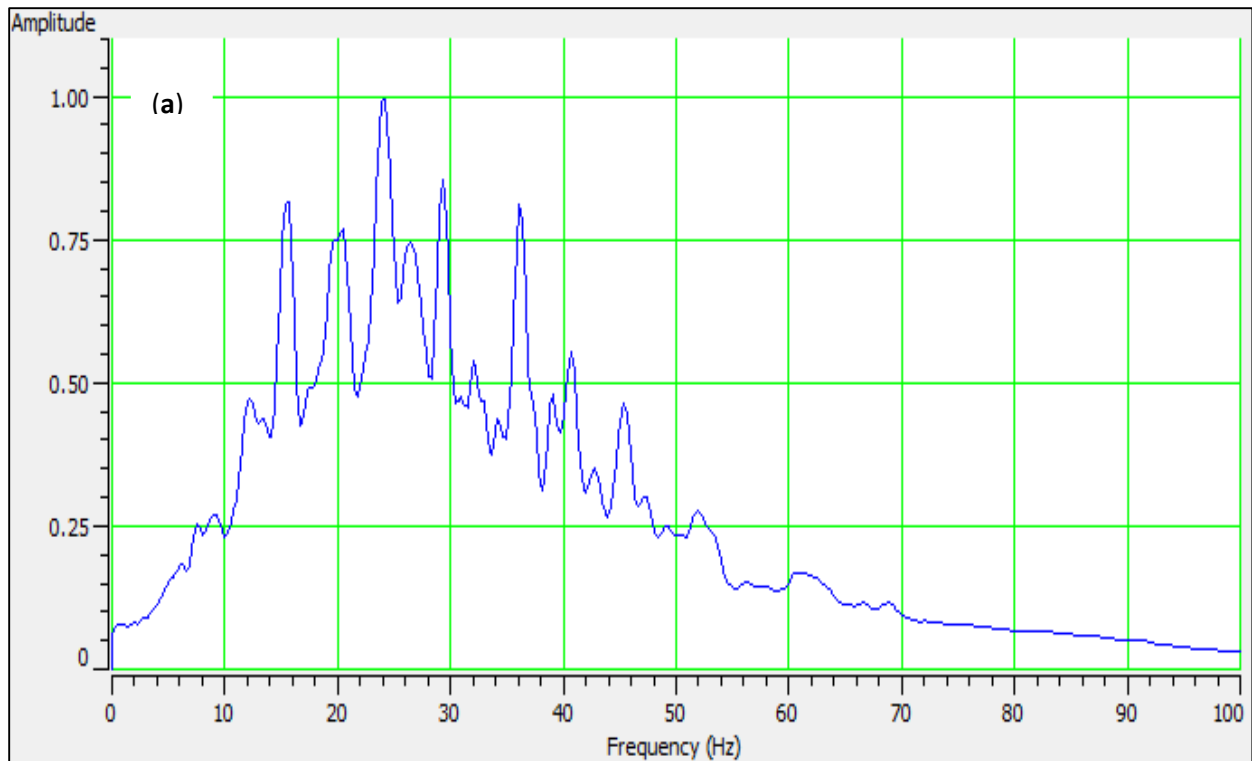


Figure 3.4 Spectral balancing of the seismic volume from 1.5 to 2.2seconds. (a) Spectrum of raw seismic volume, the peak frequency at 25Hz; low pass and cut at 0Hz to 15Hz and high pass and cut at 35Hz to 55Hz. Bottom: After spectral balancing, the amplitude of high frequencies component restored and the range of the spectrum now 15Hz to 80Hz.

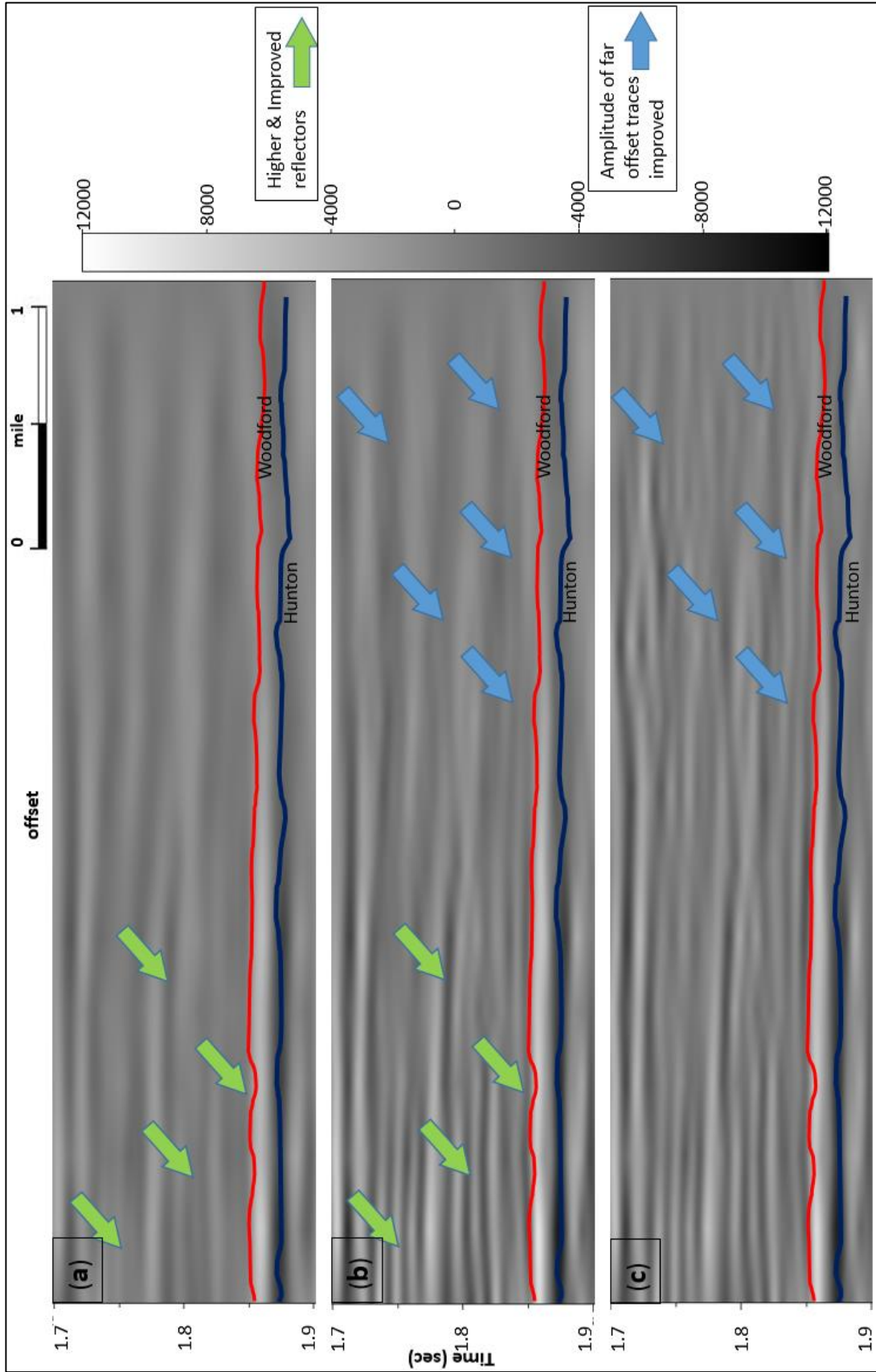


Figure 3.5 Results of data conditioning. (a) A vertical slice displaying the reflector amplitude of the original volume. (b) A vertical slice displaying the reflector amplitude of an uncompensated spectrally balanced volume. (c) A vertical slice showing the reflector amplitude of a compensated spectrally balanced volume. From (c), improvement of reflectors amplitude appears to be mainly above Woodford horizon and below Hunton horizon. The green arrows compare raw data and a spectrally balanced data. The blue arrows compare results from an uncompensated spectrally balanced data and a compensated spectrally balanced data at far offsets.

3.2 Sequence Stratigraphy (Log correlation) and Petrophysical Analysis

Due to unavailability of cuttings, outcrop exposure or core plug data of the complete Woodford Shale in the study area, this analysis aims to optimize all relevant data from a complete Woodford Shale outcrop located around the Ardmore basin, southern Oklahoma and correlate well-log information within the study area.

A constructed sequence stratigraphy model computed from gamma-ray profile and outcrop information at the outcrop location provides a model that can be used to correlate the well location within and around the paleo-environment (Galvis et al., 2017). From literature and outcrop analysis, the complete Woodford Shale is considered to be deposited during a 2nd order sequence phase of marine transgression with transgressive system tract (TST) and highstand system tract (HST), bounded by unconformities (Slatt, 2006). Influenced by two orders of cycle (2nd and 3rd), the types of lithology deposited during the entire Woodford Shale formation differ and it is a function of the relative sea level and climate (Weltje et al., 1998). Hence, the subdivisions of the Woodford can be delineated using a higher (4th) order cyclicity or parasequences. Resolving each subdivision lithology of the Woodford Shale formation is hinged on identifying the parasequences and high frequency stratigraphic cycles in the 3rd order sequence (Figure 3.6).

Utilizing well-log correlation and cross-plotting reservoir properties with elastic properties, one can scientifically interpret the Woodford lithology stack and their geomechanical properties from well-logs information. This procedure helps to “ground-truth” or constrain inferences made during fracture intensity interpretation from anisotropy analysis done through seismic data volume.

Galvis et al., (2018) characterized the Woodford Shale lithology properties through lab analysis, outcrop analysis (bed thickness), and gamma-ray data from over 350ft outcrop sample along

Interstate-35, Oklahoma. A 1-D interpretation profile of the complete Woodford Shale data was created from the outcrop. He analyzed the Woodford Shale's geomechanical properties for the three subdivisions (upper, middle and lower) and then correlated the same Woodford intervals across the available well-logs (about 8.7miles away) to investigate lateral continuity of these intervals as seen in Figure 3.7. The same procedure is applied to the wells in the study area using a gamma-ray log provided that the gamma-ray profile reflects the variation in the type of sediment deposited. This way, I investigate the existence of the upper, middle and lower Woodford with the same geomechanical and geological attributes as that observed in the outcrop sample.

Becerra et al. (2018), through XRD, XRF, TOC, and MICP analysis, characterized the Woodford Shale outcrop samples and established a direct relationship between rock stiffness and key mineralogy proxies. Hence, I rely on brittleness indicators (using Poisson's ratio and Young's modulus) to infer lithology within the intervals of interest.

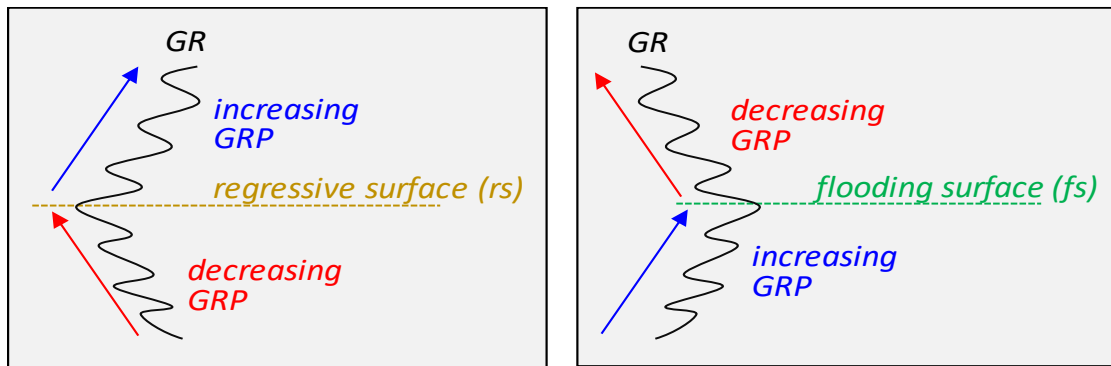


Figure 3.6. Schematic criteria for interpreting high-frequency cycles and their bounding surfaces based on Gamma Ray Parasequences (GRP). Regressive surfaces (rs) correspond with the turnaround point where stacked upward-decreasing GRP change to upward-increasing GRP. Flooding surfaces (fs) correspond with the turnaround point where stacked upward-increasing GRP change to upward-decreasing GRP.

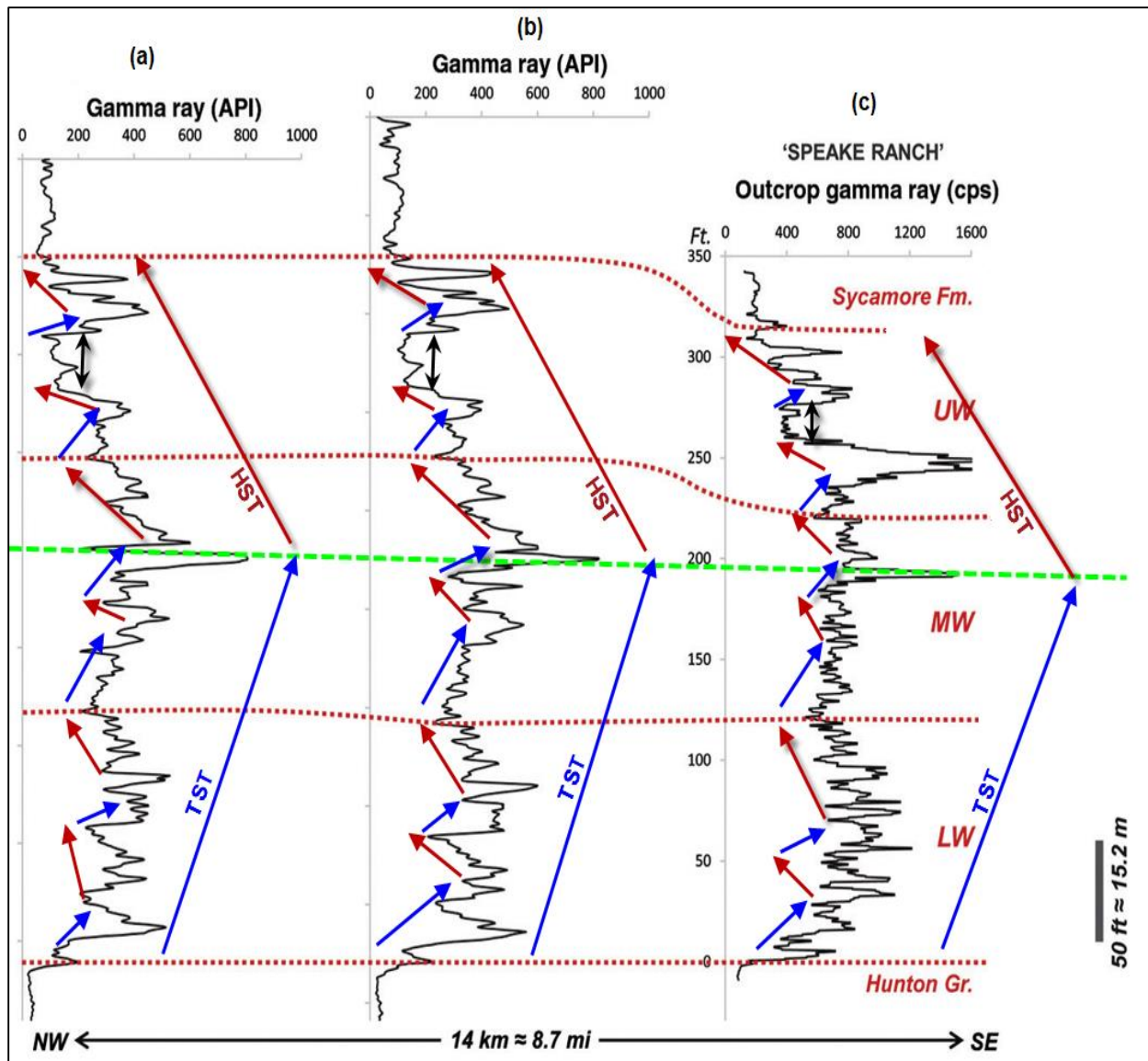


Figure 3.7. Stratigraphic column of (a) and (b) complete Woodford section of two wells about 14km away from the (c) Speake Ranch outcrop profile. Well-log gamma-ray correlation of two wells (a) and (b) clearly correlates with the outcrop (c). The long arrows are 3rd order sequences while the small arrows are 4th order parasequence. The dotted red lines separate the Woodford Shale subdivisions, the green line is the maximum flooding surface across the wells. The average vertical thickness of the Woodford Shale penetrated by the wells is approximately 107 m (350 ft). (modified from Galvis et al., 2018).

In the place of unavailable image logs or core, which are the most effective tool used to estimate fracture intensity and the orientation, I used other available petrophysical data to plot established reservoir-geomechanical relationships to predict lithology, TOC content and stiffness. Stiffness measures the characteristics of rock to fail under uniaxial stress or maintain open fractures after artificial fracturing. Two key logs that help to identify stiff lithology from a well-log are Young's modulus and Poisson's ratio, PR. Young's modulus is applied uni-axial stress divided by normal strain while Poisons ratio is the ratio of strain in a perpendicular direction to the strain in the direction of the extensional force. Point samples from the two wells in the study area were used to validate this relationship. A plot of Young's modulus with Poisson's ratio as seen in Figure 3.8 shows a trend (using the arrow direction) where the thin cherty beds in the middle Woodford Shale intervals are identified as a brittle lithology (Becerra et al., 2017) and have higher values of Young's modulus.

Poisson's ratio (PR) is the ratio of transverse contraction strain to extensional strain. The higher the PR, the lower the stiffness and vice-versa. PR is computed from compressional velocity, V_p and shear velocity, V_s , measured by the logs (equation 3.1);

$$PR = \frac{(0.5 * (\frac{V_p}{V_s})^2 - 1)}{((\frac{V_p}{V_s})^2 - 1)} \quad (3.1)$$

Young's modulus, η is the longitudinal stress σ divided by normal strain, e . It measures the ability of a material to withstand changes in length under deformation. The higher the Young's modulus, the higher the stiffness as described in Figure 3.8.

$$\eta = \frac{\sigma}{e} \quad (3.2)$$

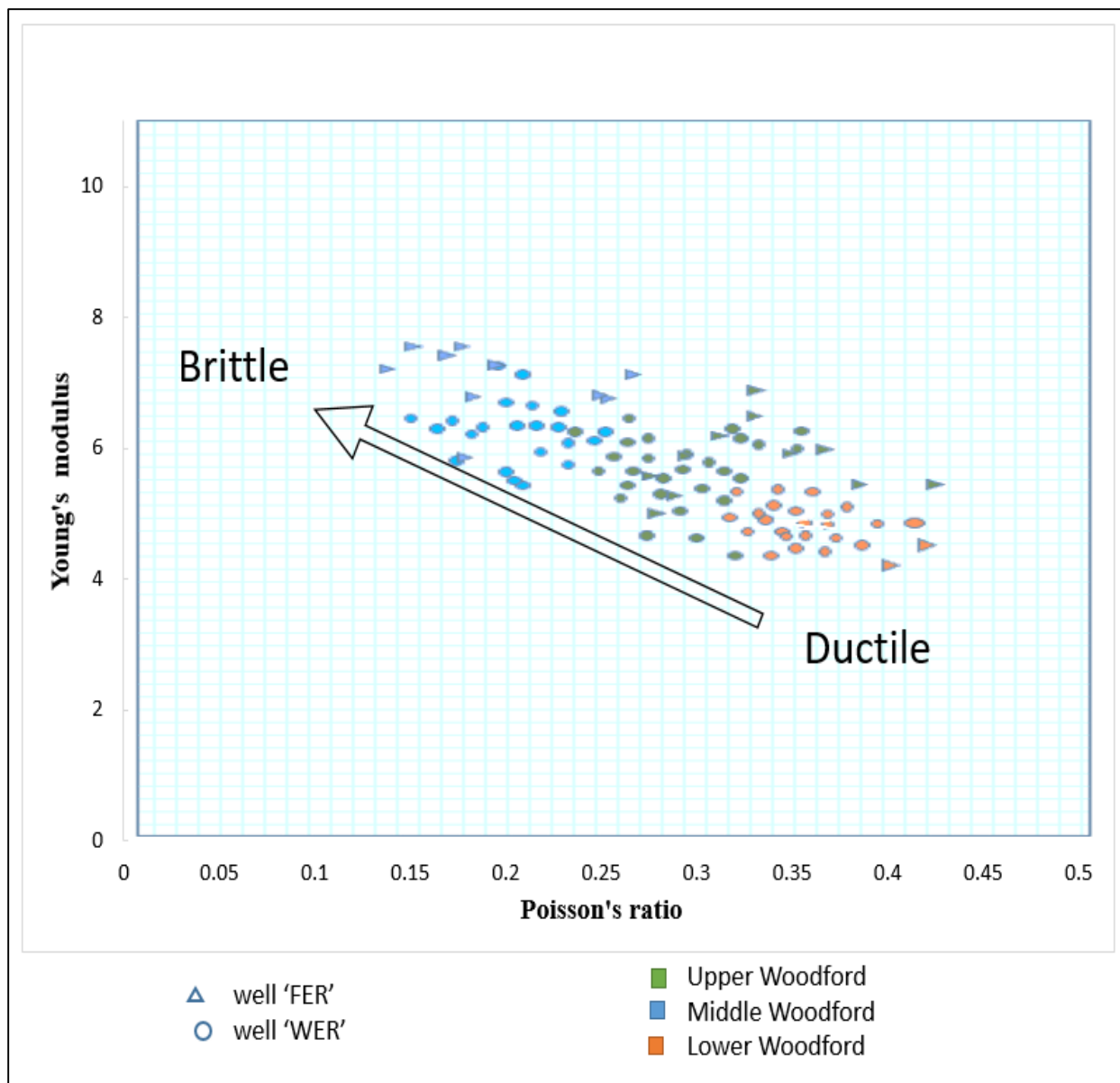


Figure 3.8. A plot of Young's modulus vs. Poisson's ratio for two wells penetrating the upper, middle and lower Woodford Shale. The trend along the arrow shows a clear distinction for three Woodford sections with the cherty formation in the middle Woodford exhibiting the highest Young's modulus value.

3.3 Seismic Inversion and Attributes Analysis

Estimation of reservoir properties from seismic volume away from well location is performed through seismic inversion. This analysis affords the opportunity to estimate rock properties from seismic reflection volumes with the help of well-log data. We derive elastic parameters such as P-impedance, S-impedance, V_p/V_s , Lambda-Rho and Mu-Rho which are directly related to lithology, fluid property, and porosity. Seismic reflection volume only provides boundary information i.e. relative impedance values at a limited band of frequency for the entire area of study, while well-log data provides absolute impedance information at a 1-D location although measured at a larger band of frequency. Seismic inversion incorporates boundary information from seismic volume and elastic properties of identified lithology at the well location to estimate interval properties across the seismic volume.

Conventionally, seismic volumes are made of seismic traces which are multiplication (convolution) of wavelets with different bandwidth and the reflection coefficients between adjacent lithological boundaries down into the earth subsurface with respect to time. Hence, relative impedance is derived by de-convolving an estimated wavelet from the seismic volume trace (Simm and Bacon, 2014). As summarized in Figure 3.9 and Figure 3.10, with a background model derived from sonic and density log, we can estimate the absolute impedance of the seismic volume. Due to the bandlimited frequency information in the seismic volume, there is always a resolution limitation. Through inversion we restored the low frequency and high frequency component absent in the seismic record. Hence, we were able to fairly delineate thin bed information missing from the seismic record using well-log data which has a frequency range from about 6 – 180Hz. The frequency spectrum from well log measurements is typically used to compensate for the limited frequency range of the seismic record.

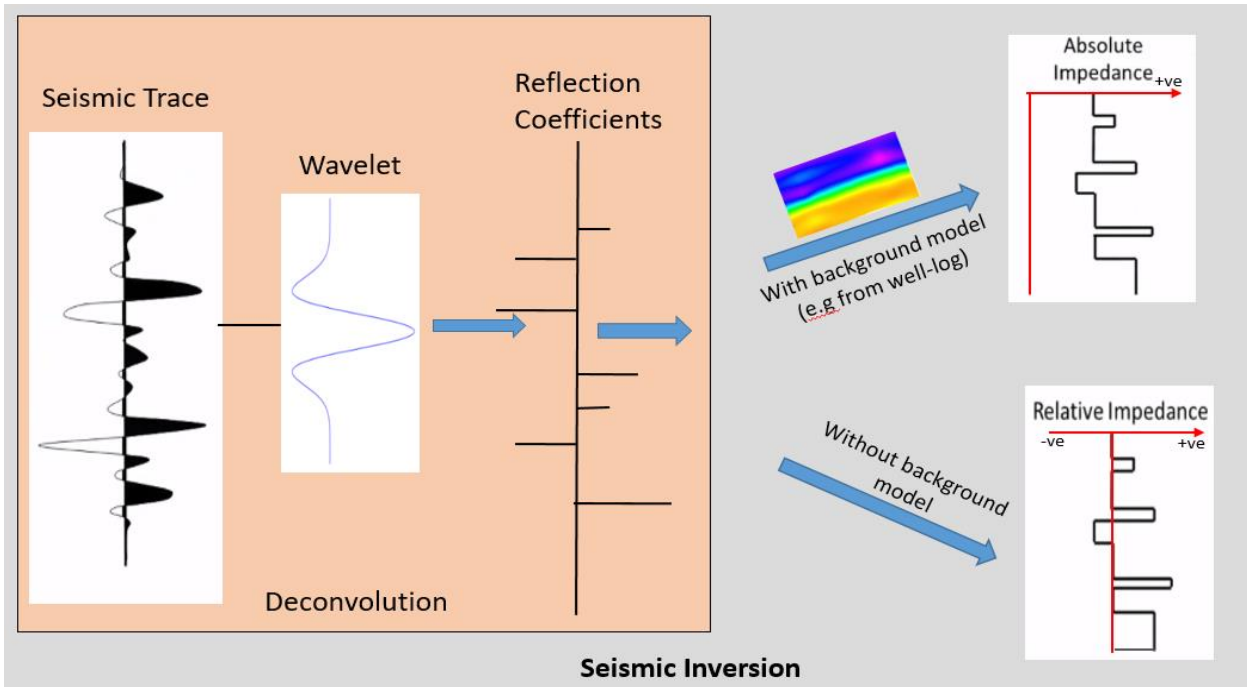


Figure 3.9 A summary diagram showing how seismic inversion first computes reflection coefficients (deconvolves the data) and then intergrates them to estimate the impedance.

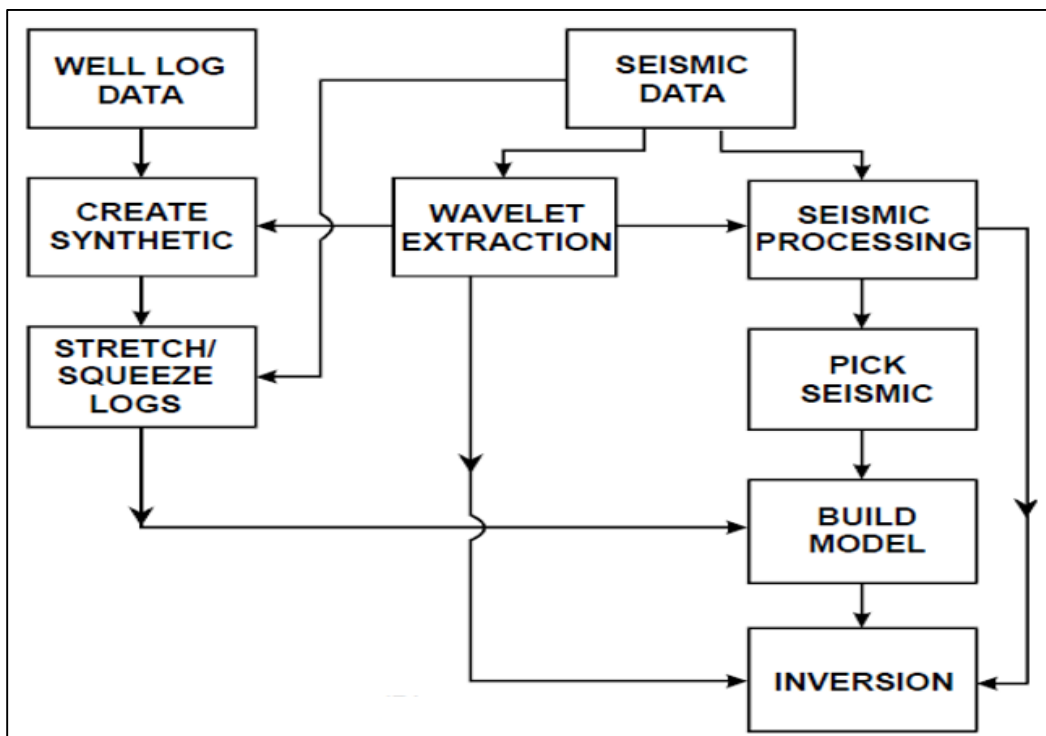


Figure 3.10. A workflow showing steps involved in a model based inversion algorithm (Alali et al., 2016).

A workflow in Figure 3.10 annotates the general steps involved in extracting geological information through a model based inversion. Before any inversion process, one critical check to make is to ensure that the phase of the seismic volume is approximately zero. The phase of the seismic data was rotated by 180^0 to correct to zero phase. From the stacked seismic volume, a statistical wavelet (time window of 150ms) is created from the seismic data which is a fair representation of the amplitude and spectrum of the seismic wavelet (Figure 3.11). The seismic time window used is within the interval of interest (600ms around Woodford horizon) from 1500 ms to 2100 ms according to the horizons picked.

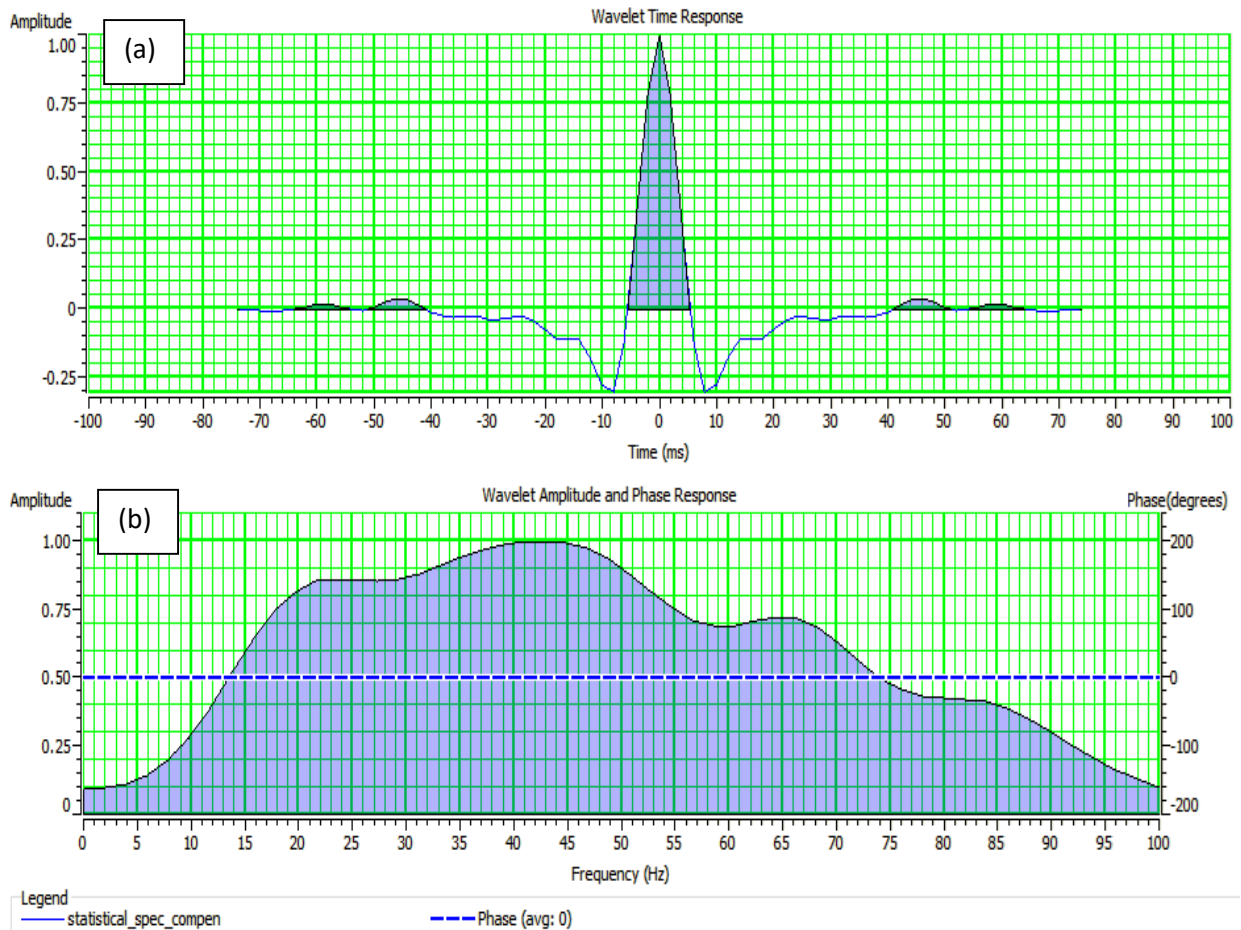


Figure 3.11 The zero-phase wavelet (a) time response and (b) magnitude response of the statistical wavelet extracted from the seismic volume using a commercial software.

3.3.1 Log Correlation

Seismic-well tie and log correlation is done using acoustic information from well 'NER', 'WER' and 'OPD'. A wavelet was first extracted from the seismic volume at a time interval of 1500ms to 2,200ms. All well-synthetic ties had a correlation of about 93% accuracy after applying the wavelet from the well-log (Figure 3.12). It was observed that the seismic volume does not have the same phase throughout as not all the wells are at zero-phase with the seismic volume at each well location. Hence, I accommodate a phase deviation of about $\pm 10^0$ for all the wells.

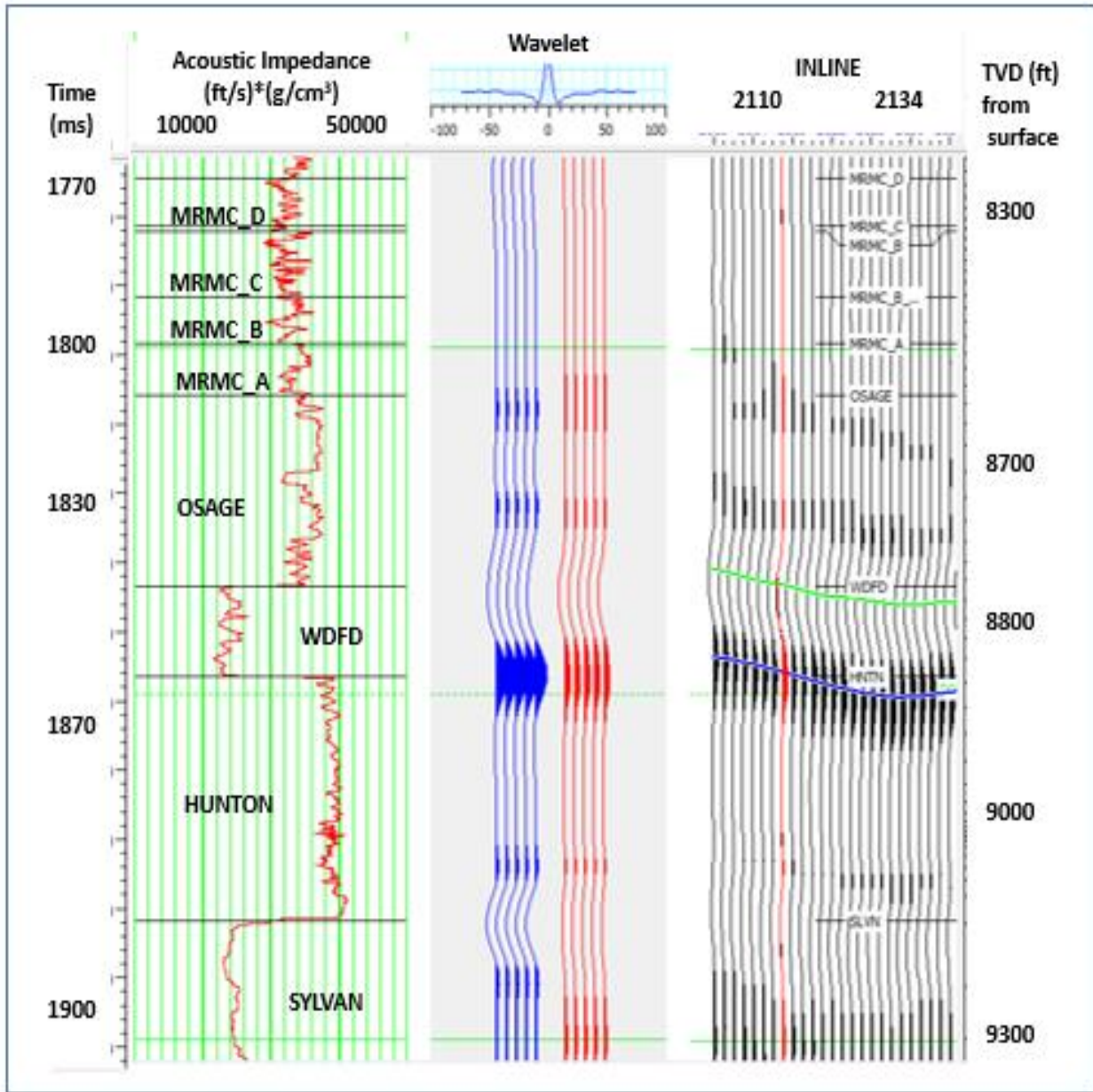


Figure 3.12. Log correlation of well 'NER'. The synthetic trace computed from the well logs and the seismic wavelet is shown in blue. The measured seismic amplitude data is in red. The correlation between the two traces is 0.968 for time range 1770 ms to 1900 ms.

A well synthetic trace is built using the synthetic wavelet and the acoustic impedance (velocity and density) of the well data. The log synthetic trace is then matched with seismic traces in order to tie seismic time with well depth at the well location. Attaining a maximum coefficient of correlation is aimed at. A wavelet is then extracted from the well-log data to ensure both seismic and well log data are at approximately zero phase.

To convert a relative impedance to absolute impedance, a background P-impedance model (for post-stack inversion) is built using three (3) well-logs (Wells OPD, NER and HER). Here, well-log impedance data are extrapolated across the seismic survey in 3D using the interpreted horizons (as in Figure 3.13).

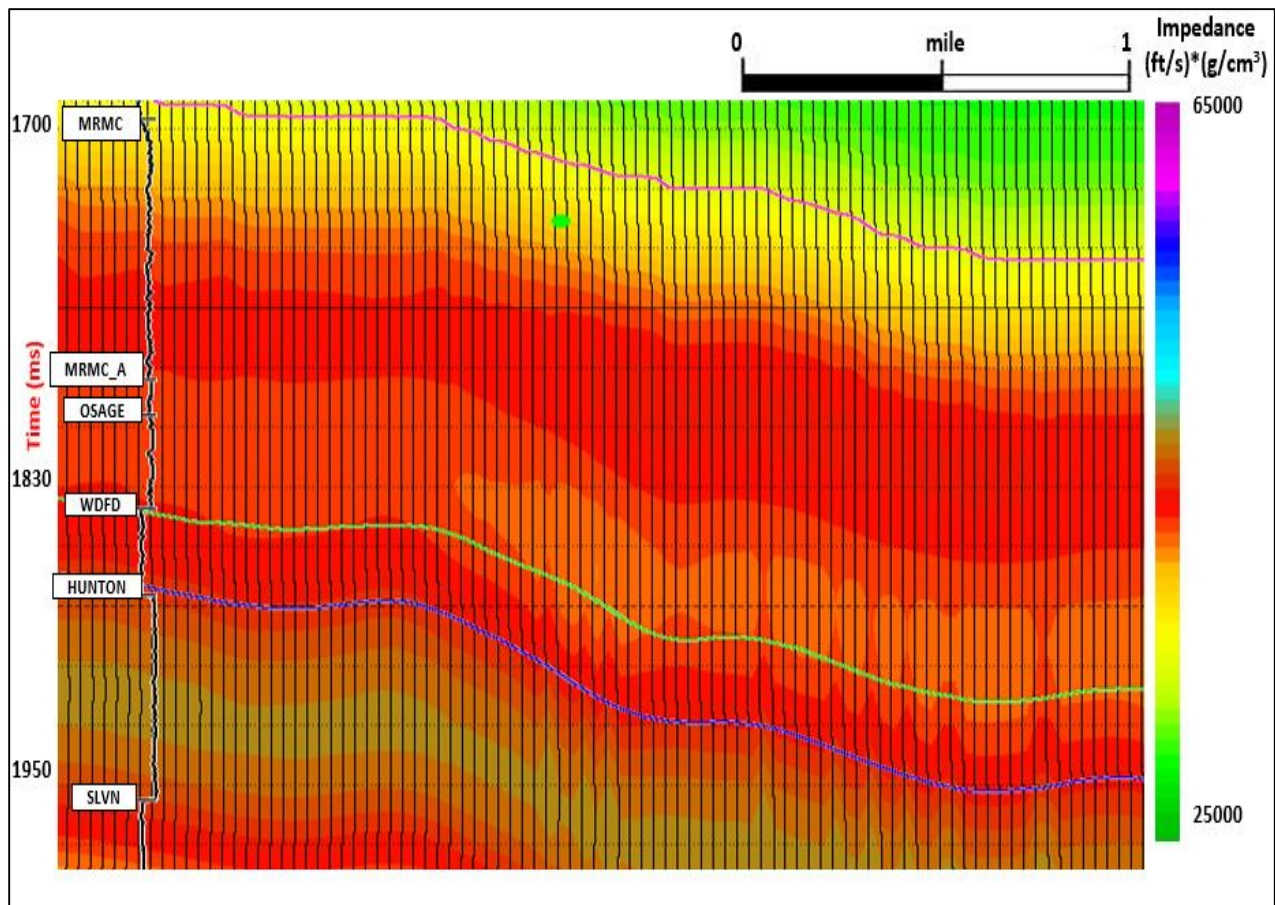


Figure 3.13. A display of the background (0-10 Hz) low frequency impedance model constructed by kriging the values measure at three wells honoring structure.

The deterministic inversion algorithm here minimizes the difference between built models from wells and seismic traces. During a model-based inversion process, measures such as impedance constraints, weighting parameters and levels of iteration can be applied to ensure impedance results generated are in tandem with geological possibilities (Simm and Bacon, 2014). Hence, there are a number of non-unique solutions involved in seismic inversion results. However, a succinct and quality checked algorithm strongly constrain the number of uncertainties or reduces incidents of wrong inversions.

3.3.2 *Inversion Issues*

Due to the non-unique nature of deterministic inversion procedure, there are certain inversion ambiguities to be considered during interpretation of the results. They include;

- Wavelet issues

To extract interface reflectivity from seismic trace, a constant wavelength, zero phase wavelet is used for deconvolution of the seismic trace. However, the phase of the seismic wavelet varies across the entire volume due to different sweeps of frequency signals sent into the ground. The phase of the seismic volume is also assumed to be consistent all through. Hence, we limit our inversion to a fairly small window about the Woodford Shale target.

- Background model

The seismic data are bandlimited, hence, any inversion result derived from frequencies lower or higher than that of the seismic volume are derived from well-log information. Therefore, deterministic inversion which relies on the background model is mainly a function of a 1-D data interpolation from available wells. As a consequence, we underestimate geologic uncertainties beyond wells location.

- Well-ties

In the absence of a check-shot survey or vertical seismic profile (VSP) data, the sonic and density log from well is used to tie time from seismic with depth at the well location. We also assume that the sonic data used for the well-tie is from a vertical well

- Thin bed effects

An implication of applying bandlimited seismic data to resolve intervals below thin bed resolution is that an amplitude trace can be inferred as several non-unique interpretations or solutions (Meckel and Nath, 1977).

3.4 Amplitude Variation with Azimuth (AVAz): Analysis and Inversion.

The presence of natural vertical fractures, micro-cracks, unequal stress regime, and very fine shale strata makes the Woodford Shale exhibit different elastic properties along different directions. All these effects make the Woodford Shale highly anisotropic. I review the concept of anisotropy for those less familiar with its use in seismic data analysis. Application of this concept to detect natural fractures solely depends on the robustness of the offset and azimuth content of the seismic volume. The rose diagram and histogram plot in [Figure 3.2](#) show the trace count and the orientation component of the volume. Models adopted for this analysis are ideal for structurally simple formations and may not be effectively applied to very complex geology.

3.4.1 Anisotropy

Anisotropy is the property of a rock or medium to exhibit variations in physical measurements with respect to different directions (Sheriff, 2002). I apply the directional variation of Woodford Shale's response to the passage of seismic waves to characteristics the fractures. Due to its complex geological nomenclature, the earth by default is generally considered as anisotropic (Saberri and Ting, 2016) and has varying degrees of anisotropy depending on lithology, structural deformation, and unequal stress acting on them. For this study, the geomechanical condition observed at the Woodford Shale outcrop (Galvis et al., 2018) is used to propose an anisotropic model which is then adopted for the study area (Figure 3.14). With this model, one can use characterize the fracture intensity and the orientation of the formation through seismic anisotropy.

3.4.2 Theory of Anisotropy

For this anisotropic model, two symmetries are applied to define and delineate the three subdivisions of the Woodford Shale as displayed in Figure 3.15. First is vertical transverse isotropy (VTI) which defines a medium whose axis of symmetry is vertical and are mostly caused by the presence of fine layering of strata within a lithology and is mostly associated with shaley formations. The second is Horizontal Transverse Isotropy (HTI) which is interpreted as any medium whose angle of symmetry is horizontal mainly consisting of parallel vertical fractures. Examples and elastic properties of these two media are elaborated in Figure 3.16.

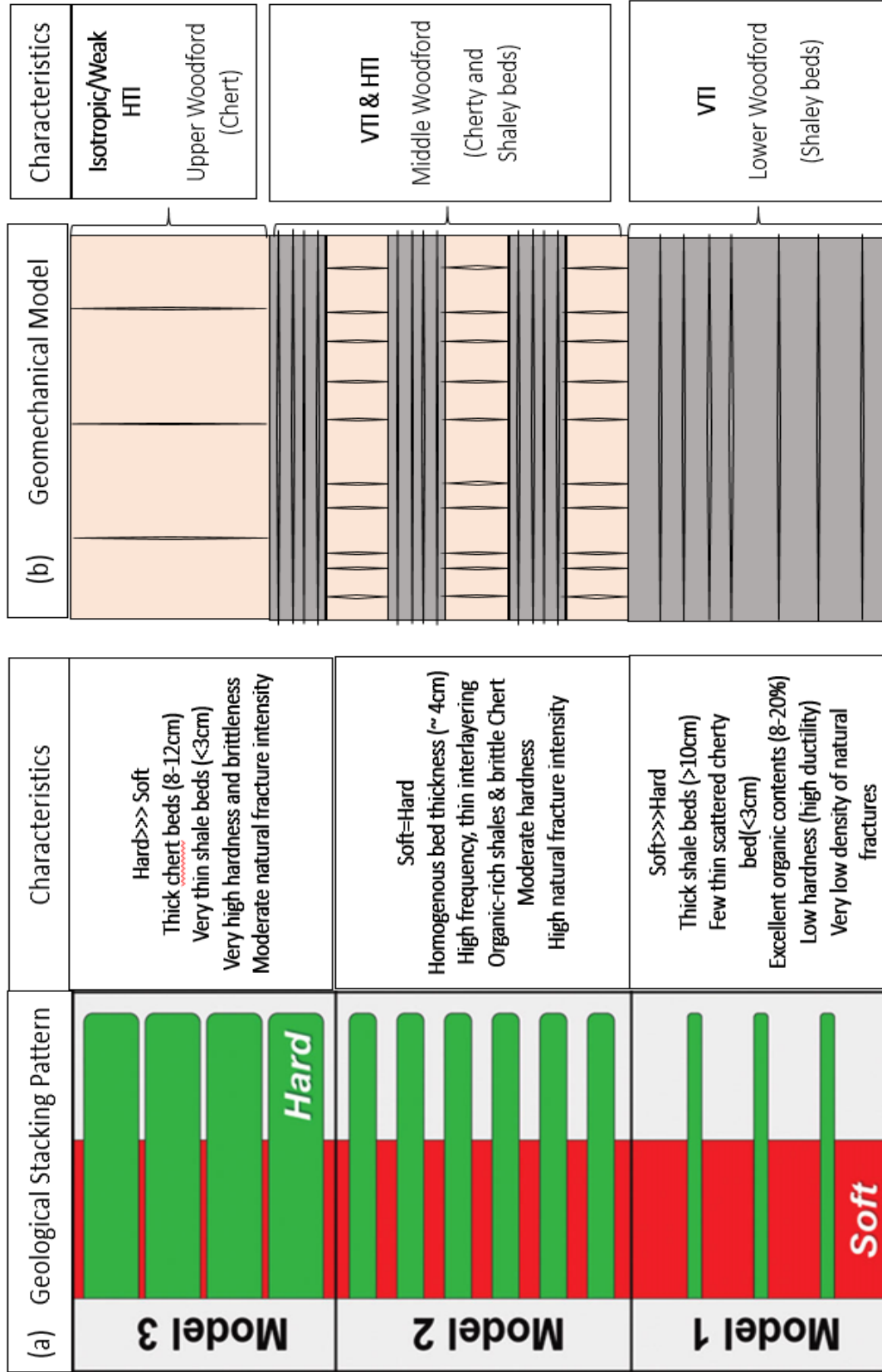


Figure 3.14 (a) Woodford Shale lithology pattern analyzed by Galvis et al. (2018) for the Woodford outcrop in Ardmore, Oklahoma. (b) The proposed complete Woodford Shale anisotropic model adopted from the geological model. Two symmetries VTI and HTI effectively delineate and describes each subdivision (upper, middle and lower Woodford Shale).

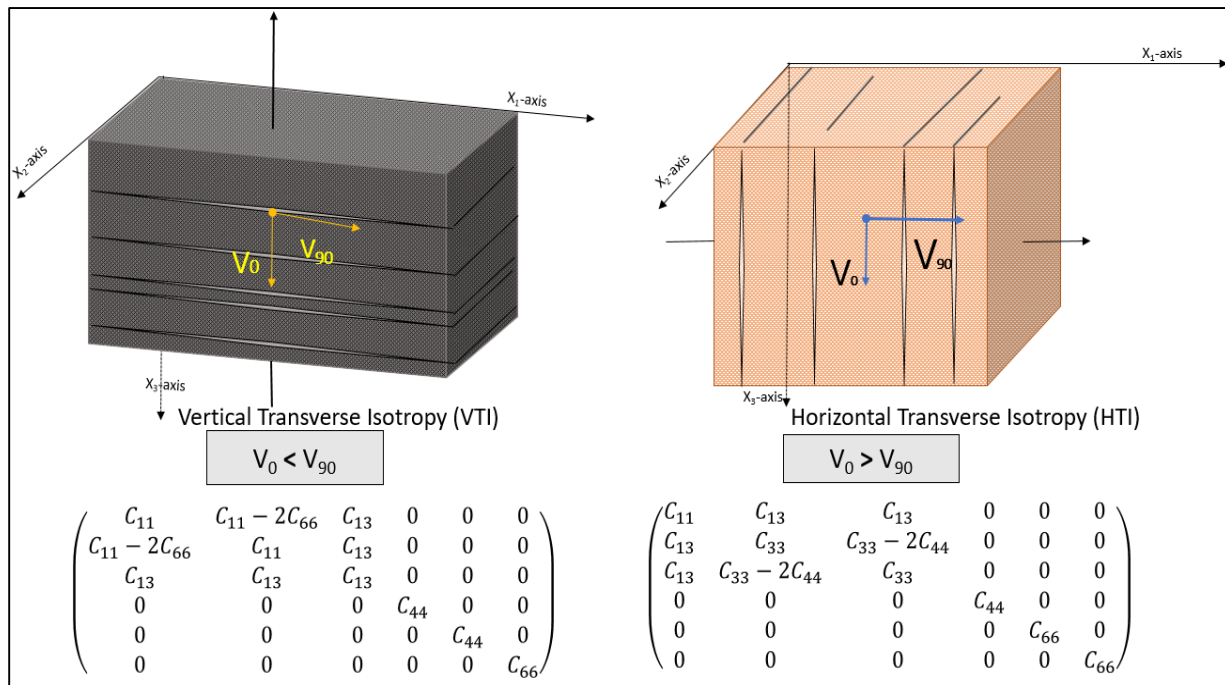


Figure 3.15 A schematic of the two symmetries used for the anisotropic model. Left: Vertical Transverse Isotropic (VTI) medium, its symmetrical vertical and horizontal velocities (V_0 and V_{90}) along the vertical axis and elastic constants in matrix format. Right: Horizontal Transverse Isotropy (HTI) medium, its symmetrical velocities along the horizontal and its elastic constants in matrix format.

Depending on the scale or frequency of measurement, the term anisotropy differs from heterogeneity, but both are sometimes confused for one another. Unlike heterogeneity which depends on the location of measurement in 3D space, anisotropy depends on the directional variation of properties at one point (Sheriff, 2002). Figure 3.15. annotates and distinguishes between these two phenomena.

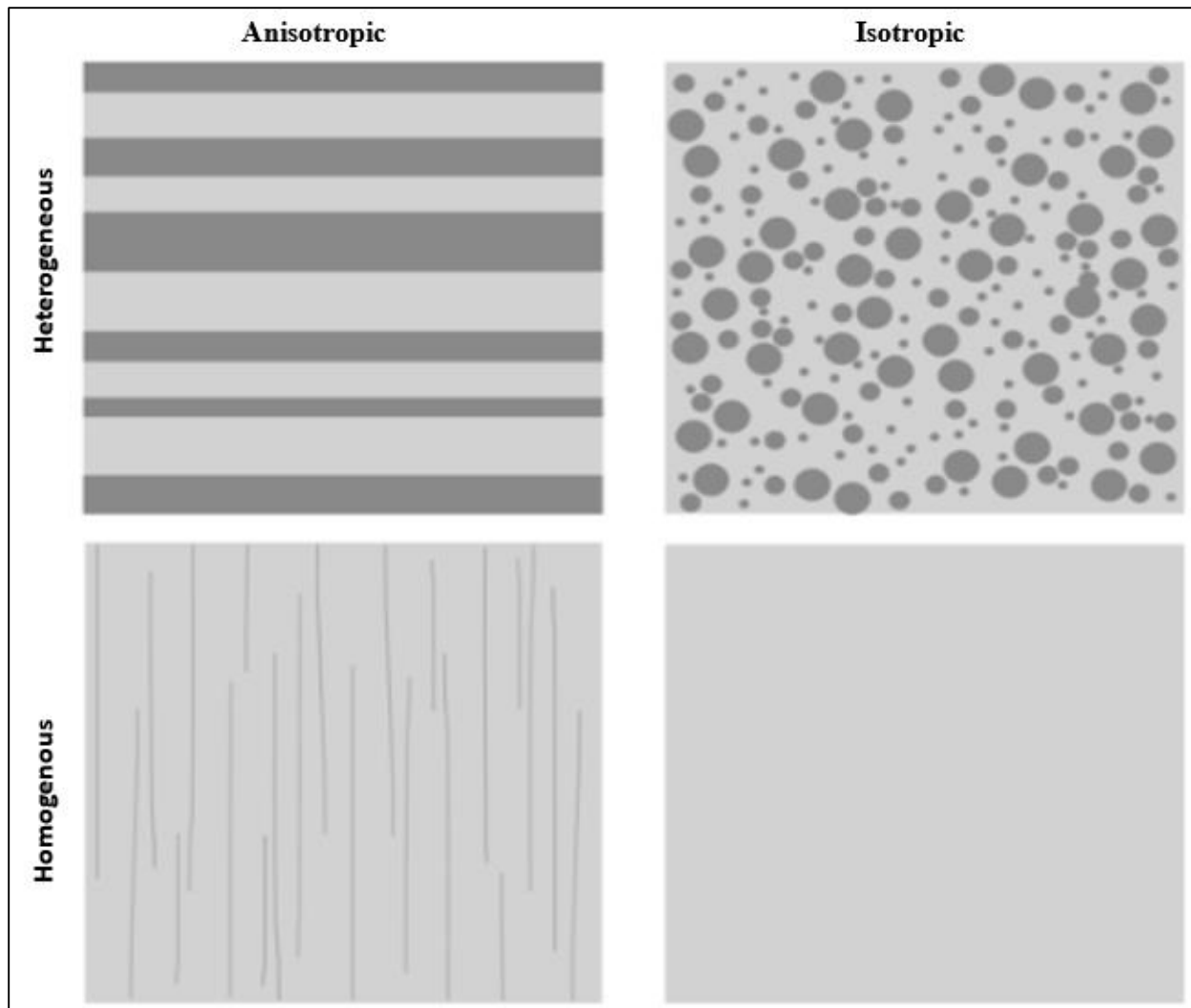


Figure 3.16. A cartoon describing different types of rock media and their symmetry (Lynn, 2018).

Elastic properties like velocities, C (compressional and shear) which are functions of stress, σ and strain, e tensors (equation 3.3) acting on the 3D (horizontal, vertical and orthogonal) particle model as seen in Figure 3.17, are expressed in terms of stiffness components, C_{ij} (see equation 3.4 - 3.8). Stiffness coefficients, C_{ij} is a form of symmetric matrix (as seen in equation 3.9) and varies for different conditions of anisotropy. Each stiffness constant identifies with velocities recorded along different planes, vertical or horizontal as seen in Figure 3.15. C_{11} (equation 3.3) corresponds to the

horizontal velocity V_{90} which is the fast velocity in a VTI medium and slow velocity in a HTI medium while the C_{33} (equation 3.4) corresponds to the vertical velocity which is the slow velocity in a VTI medium and fast velocity in a HTI medium. C_{44} and C_{66} (equation 3.5 and equation 3.6) are stiffness components for shear wave velocity of the medium. For anisotropic rocks like shales or carbonates with VTI or HTI symmetries, there are five key independent coefficients necessary, which give rise to different velocities along with different angles.

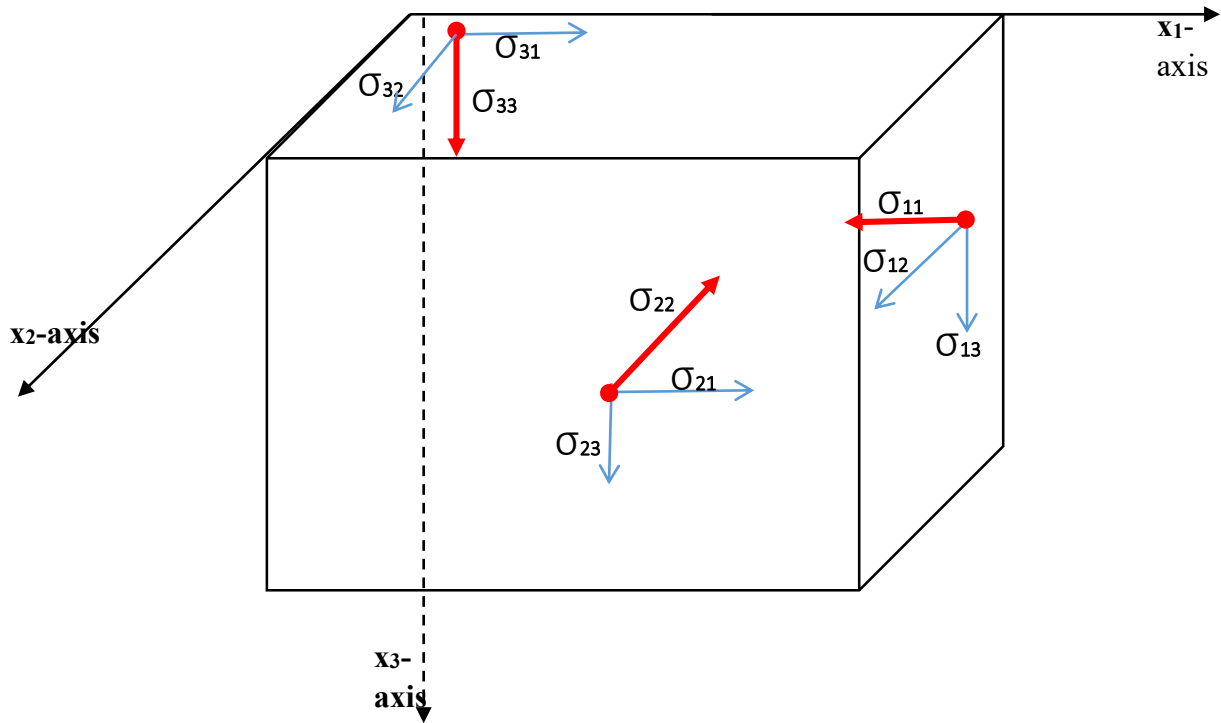


Figure 3.17 Elemental tensor components of a 3-D model

$$\boldsymbol{\sigma} = \mathbf{C}\mathbf{e} \quad (3.3)$$

$$C_{11} = \rho V_{p90}^2 \quad (3.4)$$

$$C_{33} = \rho V_{p0}^2 \quad (3.5)$$

$$C_{44} = \rho V_{s1,90}^2 \quad (3.6)$$

$$C_{66} = \rho V_{s2,90}^2 \quad (3.7)$$

$$C_{13} = \left(\frac{(4V_{p45}^2 - C_{11} - C_{33} - 2C_{44})^2 - (C_{11} - C_{33})^2}{4} \right)^{\frac{1}{2}} - C_{44} \quad (3.8)$$

$$\begin{pmatrix} C_{11} & C_{12} & C_{13} & C_{14} & C_{15} & C_{16} \\ C_{12} & C_{22} & C_{23} & C_{24} & C_{25} & C_{26} \\ C_{13} & C_{23} & C_{33} & C_{34} & C_{35} & C_{36} \\ C_{14} & C_{24} & C_{34} & C_{44} & C_{45} & C_{46} \\ C_{15} & C_{25} & C_{35} & C_{45} & C_{55} & C_{56} \\ C_{16} & C_{26} & C_{36} & C_{46} & C_{56} & C_{66} \end{pmatrix} \quad (3.9)$$

Thomsen (1986), in his classical paper identified and simplified the anisotropic nature of the two media by establishing the anisotropic parameters epsilon, ϵ , delta, δ and gamma, γ called the Thomsen parameters. For VTI media, the Thomsen parameters are;

$$\epsilon^{(VTI)} = \frac{C_{11} - C_{33}}{2C_{33}} \approx \frac{V_p(90^\circ) - V_p(0^\circ)}{V_p(0^\circ)}, \quad (3.10)$$

$$\gamma^{(VTI)} = \frac{C_{66} - C_{44}}{2C_{44}} \approx \frac{V_{SH}(90^\circ) - V_{SH}(0^\circ)}{V_{SH}(0^\circ)}, \text{ and} \quad (3.11)$$

$$\delta^{(VTI)} = \frac{(C_{13} + C_{55})^2 - (C_{33} - C_{55})^2}{2C_{33}(C_{33} - C_{55})} \approx 4 \left[\frac{V_p(45^\circ) - V_p(0^\circ)}{V_p(0^\circ)} \right] - \epsilon, \quad (3.12)$$

while for HTI media they are,

$$\varepsilon^{(HTI)} = \frac{C_{33} - C_{11}}{2C_{11}}, \quad (3.13)$$

$$\gamma^{(HTI)} = \frac{C_{44} - C_{66}}{2C_{66}}, \text{ and} \quad (3.14)$$

$$\delta^{(HTI)} = \frac{(C_{13} + C_{66})^2 - (C_{11} - C_{66})^2}{2C_{11}(C_{11} - C_{66})}. \quad (3.15)$$

For both media, ε estimates the difference between the horizontal and vertical P-wave velocities while γ measures the difference between the horizontal and vertical SH- waves and SV-wave velocities. δ is an important parameter used during seismic data processing for non-hyperbolic move-out correction (NMO) due to VTI effect which causes a hockey stick effect (Tsvankin, 1994). For seismic data interpretation, γ and δ are critical to fracture analysis as they help determine effect of vertical fractures on seismic trace amplitude (Treadgold et al., 2008).

3.4.3 Anisotropic Amplitude Variation with Offset (AVO) Analysis

Here, I analyze this interface-probing process used to investigate the degree of VTI in a medium through which P-wave is propagated. Non-hyperbolic moveout can be used to investigate the presence of fine shale strata whose influence is like that of a VTI (sometimes called polar anisotropy) model on prestack seismic reflection data. Because the data were prestack time-migrated using an anisotropic velocity, I can analyze any remaining residual move-out for a VVAz

efferent. However, VTI media also exhibit an amplitude response. A simple and crude illustration of effect of VTI on seismic reflection as a function of offset can be seen in Figure 3.17. Along the Woodford horizon (the green line in the red box), the magnitude becomes less negative as the offset increases. However, along the Meramec horizon, (the yellow line in the blue box), there is relatively little change in the trace magnitude as offset increases. The drop in the Woodford Shale reflection magnitude can be attributed to the presence of fine shale strata which represents a VTI medium as identified in the geomechanical model (Figure 3.13) which will be further discussed in the next chapter. Shales' anisotropic nature is mathematically expressed in terms of Thomsen's parameters.

Approximation of the amplitude reflectivity along boundary, $R_{\text{iso}}(\theta)$ as derived by Zoepritz (1985) and linearized by Aki-Richards (1980) have only been effective for isotropic medium (Wright, 1987). However, this approximation provides poor estimated reflection amplitudes for highly anisotropic models at middle to far offset. The Aki-Richards AVO approximation accounts for changes in P-wave velocity, S-wave velocity and density.

$$R_{\text{iso}}(\theta) = \left[\frac{1}{2} \left(\frac{\Delta V_p}{V_p} + \frac{\Delta \rho}{\rho} \right) \right] + \left[\frac{1}{2} \frac{V_p}{V_p} - 4 \frac{V_s^2}{V_p^2} \frac{\Delta V_s}{V_s} - 2 \frac{V_s^2}{V_p^2} \frac{\Delta \rho}{\rho} \right] \sin^2 \theta + \left[\frac{1}{2} \frac{\Delta V_p}{V_p} \right] (\tan^2 \theta - \sin^2 \theta), \quad (3.16)$$

Where the intercept, $A_{\text{iso}} = \left[\frac{1}{2} \left(\frac{\Delta V_p}{V_p} + \frac{\Delta \rho}{\rho} \right) \right]$,

gradient, $B_{\text{iso}} = \left[\frac{1}{2} \frac{V_p}{V_p} - 4 \frac{V_s^2}{V_p^2} \frac{\Delta V_s}{V_s} - 2 \frac{V_s^2}{V_p^2} \frac{\Delta \rho}{\rho} \right]$,

and curvature, $C_{\text{iso}} = \left[\frac{1}{2} \frac{\Delta V_p}{V_p} \right]$.

Ruger (2002) modified Aki-Richards AVO approximation by inserting Thomsen's anisotropic parameters δ and ε into the second and third term of equation 3.17 to accommodate VTI anisotropy.

$$R(\theta) = R_{\text{iso}}(\theta) + \left(\frac{\Delta \delta}{2} \sin^2 \theta \right) + \left(\frac{\Delta \varepsilon}{2} \sin^2 \theta \tan^2 \theta \right) \quad (3.17)$$

To visualize the effect of anisotropy, I approximate the reflectivity using Aki-Richards equation for isotropic model, $R_{\text{iso}}(\theta)$ and compare with Ruger approximation, $R(\theta)$.

$$R(\theta) = A_{\text{iso}} + \left(B_{\text{iso}} + \frac{\Delta \delta}{2} \right) \sin^2 \theta + \left(C_{\text{iso}} + \frac{\Delta \varepsilon}{2} \right) \sin^2 \theta \tan^2 \theta \quad (3.18)$$

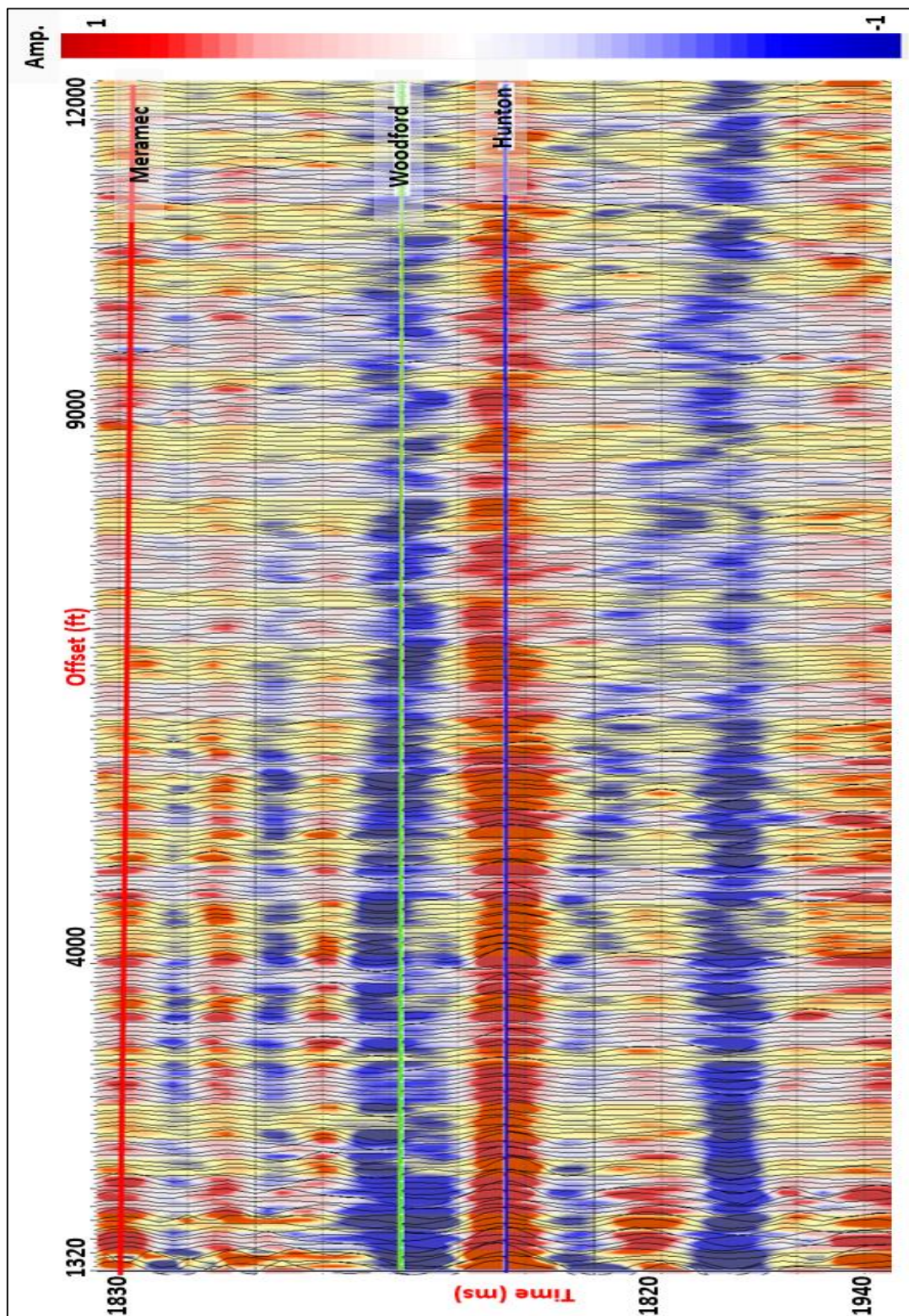


Figure 3.18. A vertical display of the trace amplitude as a function of offset for a representative prestack migrated CRP gathers. The red line indicates the top Meramec horizon, the green line indicates the top Woodford Shale, and the blue the top Hunton Group. Note the decrease in amplitude with increasing offset for the top Woodford shale horizon.

3.4.4 Amplitude Variation with Azimuth (AVAz) Inversion

AVAz is invaluable to understanding fracture intensity and the orientation provided that the values of the source-receiver angle of the seismic data changes with respect to the north orientation (azimuthal component). In the Woodford Shale outcrop analysis shows a great many natural fractures that can be open by relatively tensile horizontal stress field. Values of the P-wave velocity of Woodford Shale measured along the horizontal axis of symmetry changes symmetrically or asymmetrically due to the effect of regional stress and the presence of vertical fractures (as in Figure 3.19). Such phenomenon is the fundamentals of amplitude variation with azimuth analysis (sometimes referred to as azimuthal anisotropy). Analysis from Johnson (1995) and Lynn et al. (1995) using field data, corroborates how P-wave reflection is controlled by azimuthal variation due to the presence of fractures.

Unlike anisotropic AVO analysis, where P-wave reflectivity is dependent only on incident angle θ for VTI model, AVAz P-wave reflectivity is controlled not only by the incident angle θ but also by the azimuthal angle ϕ from the north. when $\theta=0$; the zero offset reflection has no azimuthal variation. When $\phi=0$; AVAz reduces to Anisotropic AVO analysis as all gradients associated to a sine function reduces to zero in the Ruger's HTI AVAz approximation (equation 3.19).

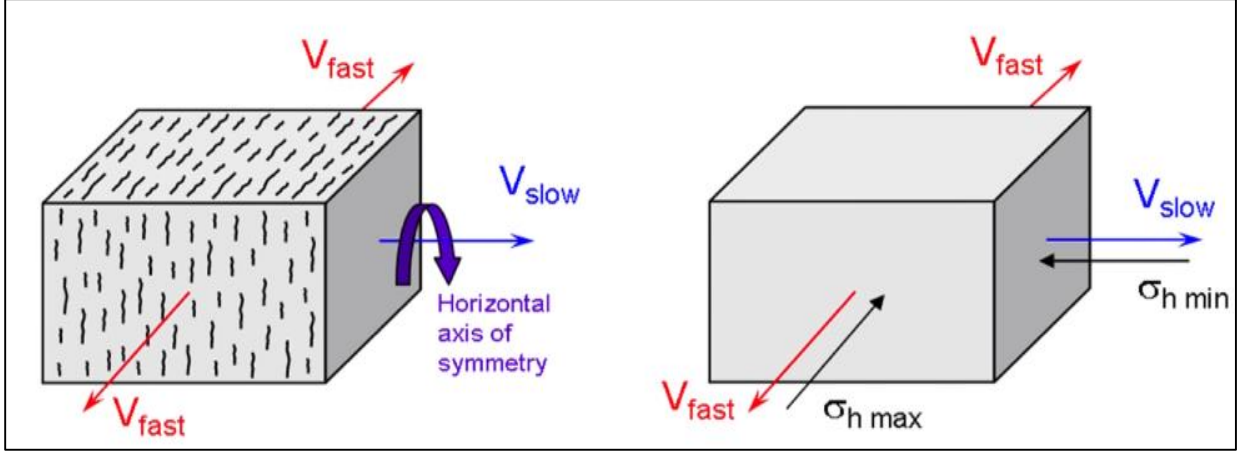


Figure 3.19. Display of the two major HTI anisotropy factors; vertical aligned fractures (left) and unequal horizontal stress (right) controlling azimuthal velocity variation in seismic reflectivity within the Woodford Shale formation.

Changes in different fractures and stress orientation gives rise to changes in seismic reflectivity for different source-receiver orientations. Hence, the Thomsen's anisotropic parameters (δ and γ) are non-zero as they are directly proportional to the variation of P-wave velocity as azimuth changes. Thomsen's parameters for HTI model are derived by transforming the vertical axis reference to 90° denoted by (*HTI*) (see equations 3.13 – 3.15). Ruger's (2002) approximation, which is a revision of Aki-Richards (1980) linearized equation for P-wave reflectivity AVO is utilized to extract the AVAz terms in HTI medium.

$$R(\theta, \phi) = A + [(B_{\text{iso}} + B_{\text{aniso}} \sin^2(\phi_j - \phi_{\text{iso}}))] \sin^2 \theta \quad (3.19)$$

$$\text{where, } B_{\text{aniso}} = \left[\frac{1}{2} \Delta \delta^v - 8 \left(\frac{V_s^2}{V_p^2} \right) \Delta \gamma \right].$$

The following AVO and AVAz terms are used in estimating the intensity and the orientation of fractures;

A – The standard intercept.

B_{iso} – The isotropic gradient.

B_{aniso} – The anisotropic gradient, a measure of fracture density.

ϕ_{iso} – The direction of the isotropy plane, which is the same as the fracture strike (azimuthal Isotropy).

θ – Incidence angle.

Ruger’s approximation integrates the anisotropic variables and azimuthal components into Aki and Richards equation (equation 3.16). Hampson Russell software package was used for the anisotropic inversion. The first two terms of the Ruger’s equation are used for anisotropy inversion. The only AVAz terms used are the anisotropy gradient, B_{aniso} and azimuthal isotropy, ϕ_{iso} .

3.4.5 AVAz Modelling

To validate his approximation, Ruger (2012) used synthetic models with different range of anisotropy as described in table 1 to investigate the effectiveness of AVAz analysis in identifying fracture intensity and the orientation.

Model	$\Delta Vp/Vp$	A	$\Delta\mu/\mu$	$\delta^{(HTI)}$	$\epsilon^{(HTI)}$	$\gamma^{(HTI)}$
A	0.1	0.1	0.2	0	0	-0.1
B	0.1	0.1	0.2	-0.1	0	0
C	0.1	0.1	0.2	0	-0.1	0
D	0.1	0.1	0.2	-0.05	-0.05	-0.15

Table 1. Values of the four models used to test for AVAz analysis. From Ruger (2012)

Four models A, B, C, and D (with properties in table 1) each made of an isotropic half-space over an HTI half-space medium were used. From AVO analysis of Model B and C (Figure 3.21 and 3.22), which has zero anisotropy parameters i.e. implying no fracture, there is a small or marginal change in the values of reflection coefficient with respect to azimuthal curves up until angle 25° incidence angle. For AVAz analysis of model C and D, there is relatively no change in the reflection coefficient for all the angle curves except for angle 45° curve at azimuth 90° . For Models A and D (Figure 3.20 and 3.21), with over 10% value of $\Delta\gamma$, Ruger's approximation is able to resolve the presence of fractures. In the AVO analysis, the azimuth curves projects along different directions as the incidence angle increases and angle curves are expresses unique sinusoids profile along azimuth.

The main goal of AVAz analysis is to run an anisotropic inversion for the entire Woodford Shale interval in the seismic volume and generate the B_{aniso} and ϕ_{iso} parameters to delineate the fracture intensity and its orientation. A weighted average of the B_{aniso} gradient of the Woodford Shale interval co-rendered with ϕ_{iso} volume is computed. From prior knowledge, the middle Woodford Shale with good reservoir quality and completion quality is identified as the region with high B_{aniso} gradient. This helps with the characterization of the Woodford Shale interval.

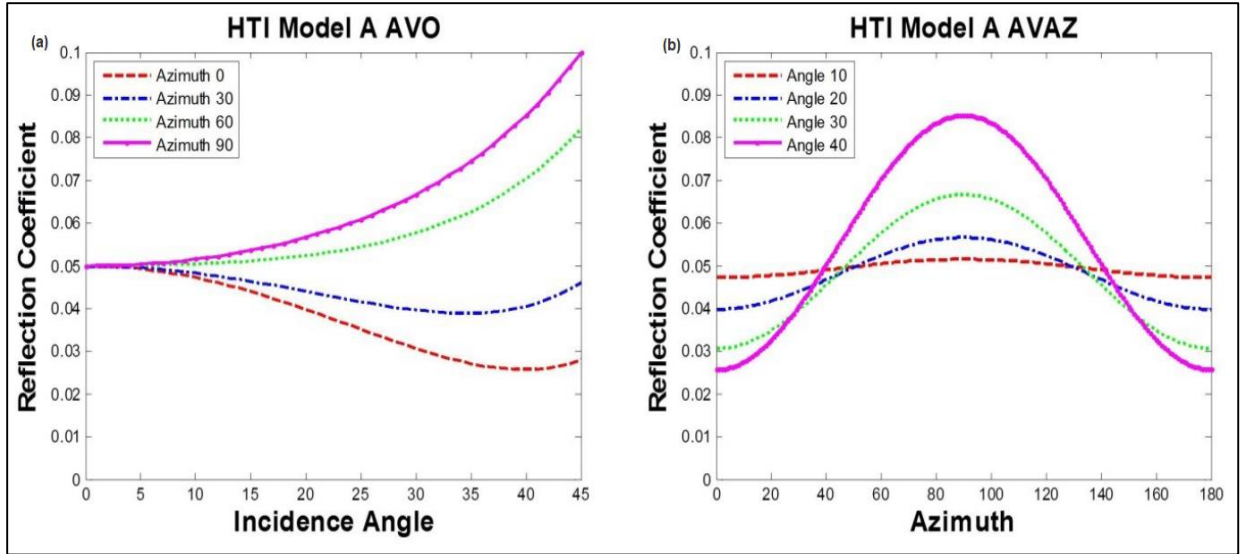


Figure 3.20. (a) The reflection coefficients for Model A (change in $\gamma=0$, $\epsilon=0$ and $\delta=-0.1$) as a function of azimuth, ϕ for 0, 30, 60 and 90 degrees. (b) The reflection coefficients for Model C (change in $\gamma = -0.15$, $\epsilon=-0.05$ and $\delta=-0.05$) as a function of azimuth angle for incident angles $\theta = 10, 20, 30$ and 40 degrees.

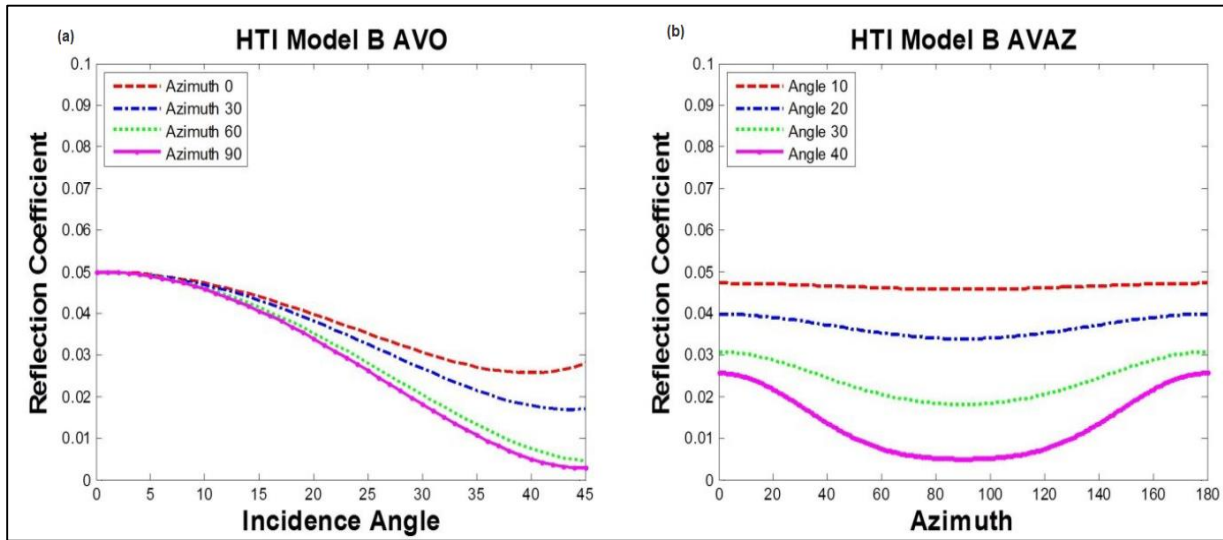


Figure 3.21.(a) The reflection coefficients for Model B (change in $\delta=-0.1$) as a function of azimuth, ϕ for 0, 30, 60 and 90 degrees. (b) The reflection coefficients for Model B (change in $\delta = -0.1$) as a function of azimuth angle for incident angles $\theta = 10, 20, 30$ and 40 degrees.

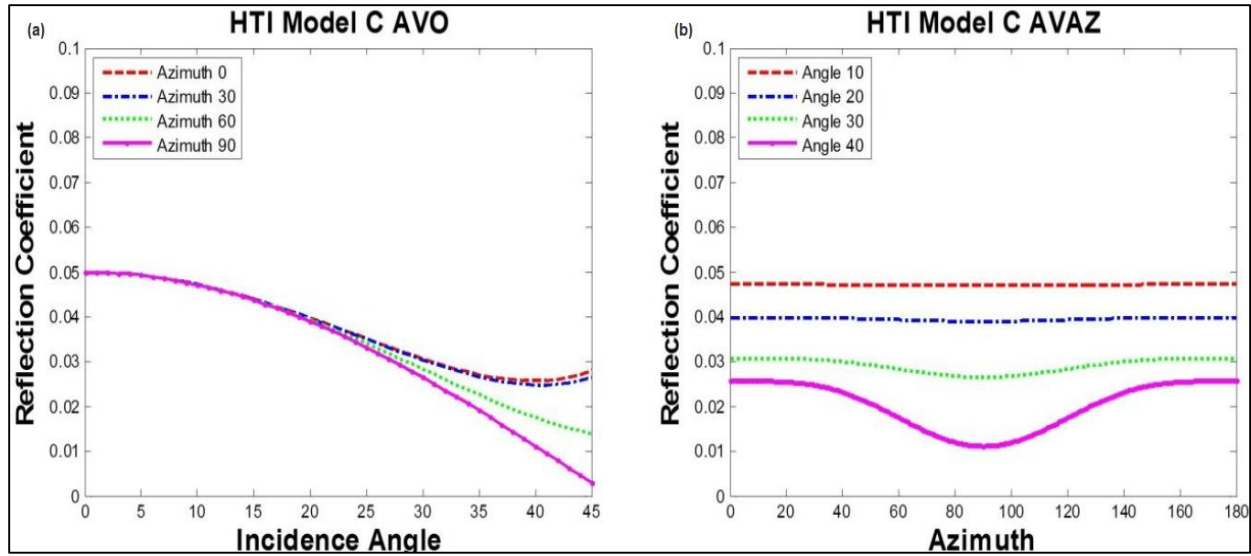


Figure 3.22. (a) The reflection coefficients for Model C (change in $\epsilon = -0.1$) as a function of azimuth, ϕ for 0, 30, 60 and 90 degrees. (b) The reflection coefficients for Model C (change in $\epsilon = -0.1$) as a function of azimuth angle for incident angles $\theta = 10, 20, 30$ and 40 degrees.

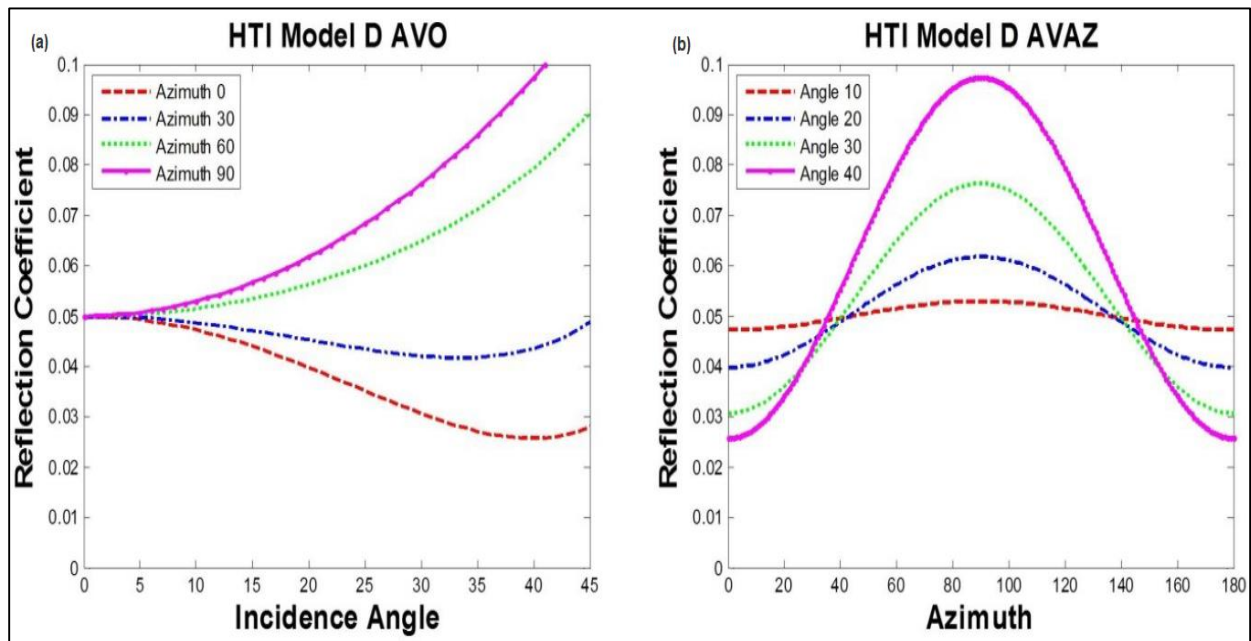


Figure 3.23. (a) The reflection coefficients for Model D (change in $\gamma = -0.15$, $\epsilon = -0.05$ and $\delta = -0.05$) as a function of azimuth, ϕ for 0, 30, 60 and 90 degrees. (b) The reflection coefficients for Model C (change in $\gamma = -0.15$, $\epsilon = -0.05$ and $\delta = -0.05$) as a function of azimuth angle for incident angles $\theta = 10, 20, 30$ and 40 degrees.

3.5 Seismic Attribute Analysis

Through seismic (volumetric) attributes like coherence and curvature, I provide information on tectonic stress (regional and local) influence on the stratigraphy and the paleo-topography of the Woodford formation (top and base). By extension, this influence connotes the placement of fractures within the Woodford subdivisions (Hart et al., 2002). To assess overall formation topography of the formation, we investigate the boundary or layer properties of the interval of interest by analysis its geometric attributes from the seismic traces along Woodford horizon time.

Here, I used two important seismic attributes; coherence and curvature attributes to resolve discontinuities, flexures and folds which are indicators for fracture swarms in brittle rocks (Chopra and Marfurt, 2007)

3.5.1 Coherence (Similarity)

Coherence delineates surface discontinuities by measuring the similarity between seismic traces (Chopra and Marfurt, 2010). Either along horizon surface or time slice, coherence helps to identify abrupt changes in seismic waveform that can be interpreted as low coherence and can be linked to presence of fractures or fault. Coherence is effective if the geologic feature of interest is resolvable from seismic waveforms.

For the semblance-based coherence analysis, I define a spatial and temporal aperture computation window and define dip and azimuth at each point. To improve lateral resolution, I used a small window width of 110 ft and a half-window time of 20 ms for computing the inline and crossline components of the structural dip. The inputs for computing coherence attribute are the inline dip, crossline dip, and seismic amplitude data.

3.5.2 Curvature

Curvature is a valuable seismic attribute used to predict features like fractures, fault and flexures expressed through their geomorphological expressions. These features reflect the nature and orientation of the paleostress regime and the present-day stress regime (Chopra and Marfurt, 2007). One of the key indicators for identifying fracture swarms in brittle rocks is the flexure pattern seen in the curvature attribute on the surface of geobodies.

I compute a 3D volumetric-type curvature from a vertical window of seismic samples in order to avoid backscattered noise and to resolve features that cannot be seen from seismic horizon. Positive curvature and negative curvature with a short wavelength analysis window is computed to delineate finer and localized fractured systems. Most positive curvature portrays the anticlinal features while the most negative curvature mirrors synclinal features as seen in Figure 3.24.

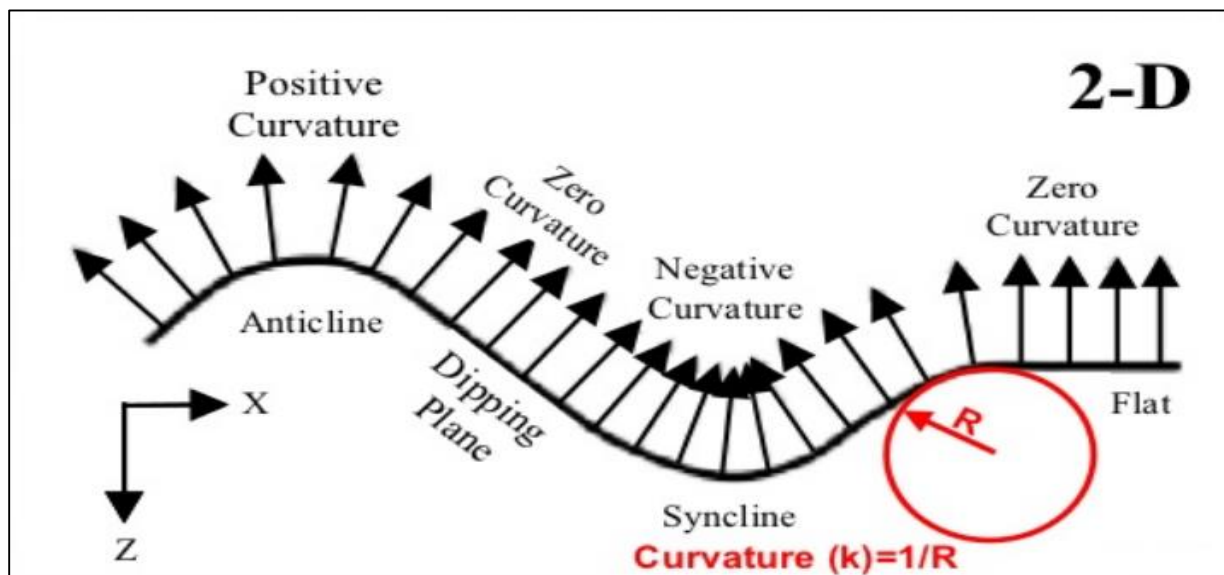


Figure 3.24 A schematic representation of a 2D curvature. Synclinal features have negative curvature, anticlinal features have positive curvature, and planar features have zero curvatures (Modified from Roberts, 2001).

4 RESULTS AND DISCUSSIONS

4.1 Log Correlation

Gamma-ray log, a reliable lithology log, is used to correlate similarities in lithology between the reference outcrop gamma-ray log 350 ft thick and well-logs in the study area. In this section, the primary task is to apply gamma-ray parasequences to identify and correlate the upper, middle and lower Woodford Shale intervals as identified in the complete Woodford Shale outcrop in Ardmore. As seen in Figure 4.1, the distance between the study area and the outcrop is about 155 miles. From Figure 4.2, there is a good correlation in gamma-ray parasequences between the well-logs and the outcrop gamma-ray log. A 120 ft thick, high gamma-ray section of the lower Woodford Shale at the outcrop location approximately matches 30ft of lower Woodford Shale gamma-ray profile at wells 'BOB', 'NER' and 'WER' corresponding to a 3rd order transgressive system tract (TST).

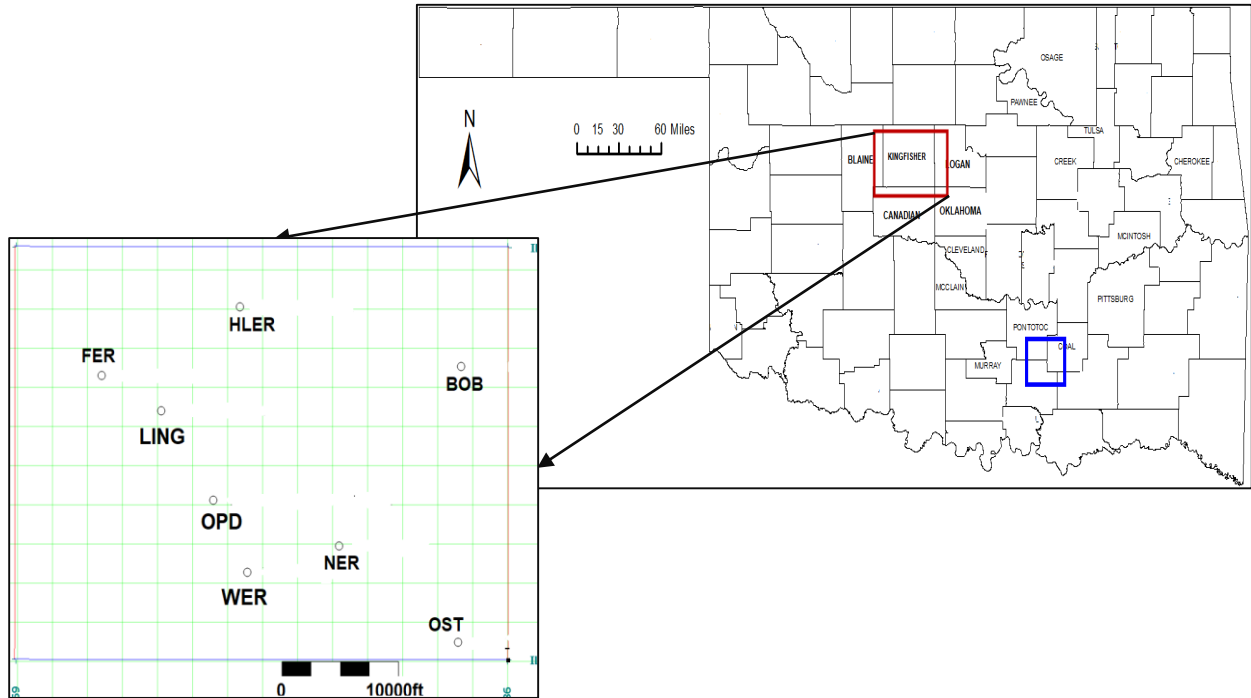


Figure 4.1: Right: Oklahoma map showing location of the study area in red box and location of the reference Woodford Shale outcrop at Speake Ranch southern Oklahoma in blue box. Left: Map of the study area showing the location of the wells used for log correlation and petrophysical analysis.

More importantly, I situate the interval with the highest TOC content across all the wells. Using approximately 30 ft middle Woodford Shale section of the well-log has a coarsening upward gamma-ray profile trend between the TST and HST and the peak gamma-ray count representing the condensed section. This trend is also seen in the 110 ft middle Woodford section of the outcrop profile. This validates the existence of the same lithology stack at the outcrop as characterized by Galvis et al., (2017). In Figure 4.3, eight (8) well logs were correlated to ascertain lateral continuity of the Woodford Shale intervals across the entire survey area. With middle Woodford Shale ranging from 20ft to 60ft, there is an appreciable level of heterogeneity in thickness within the Woodford formation subdivisions.

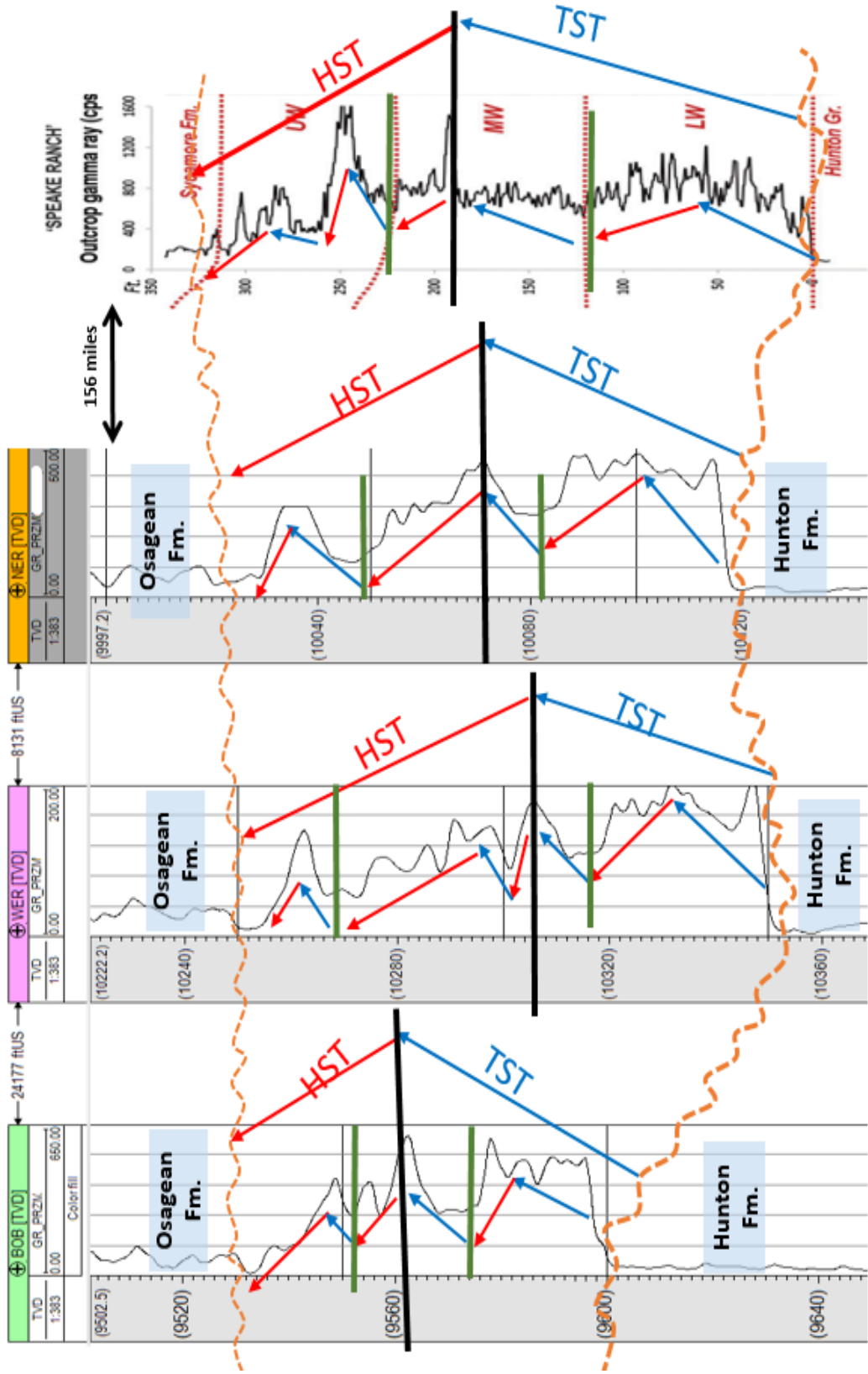


Figure 4.1 Complete Woodford Shale lithology (gamma-ray) log correlation using 3rd order cycles (long red and blue arrows) across three (3) wells (BOB, WER, and NER) in the study area and the fourth gamma-ray log from the Speake Ranch outcrop. Correlating lithologies using Gamma-ray Parasequences, GRP (small blue and red arrows), all the logs approximately as the subdivisions are bounded by the green line. The maximum flooding surface (black line) is easily identified in the middle Woodford Shale for both profiles and the subdivisions (separated by green lines) are identified as a complete 4th order sequence.

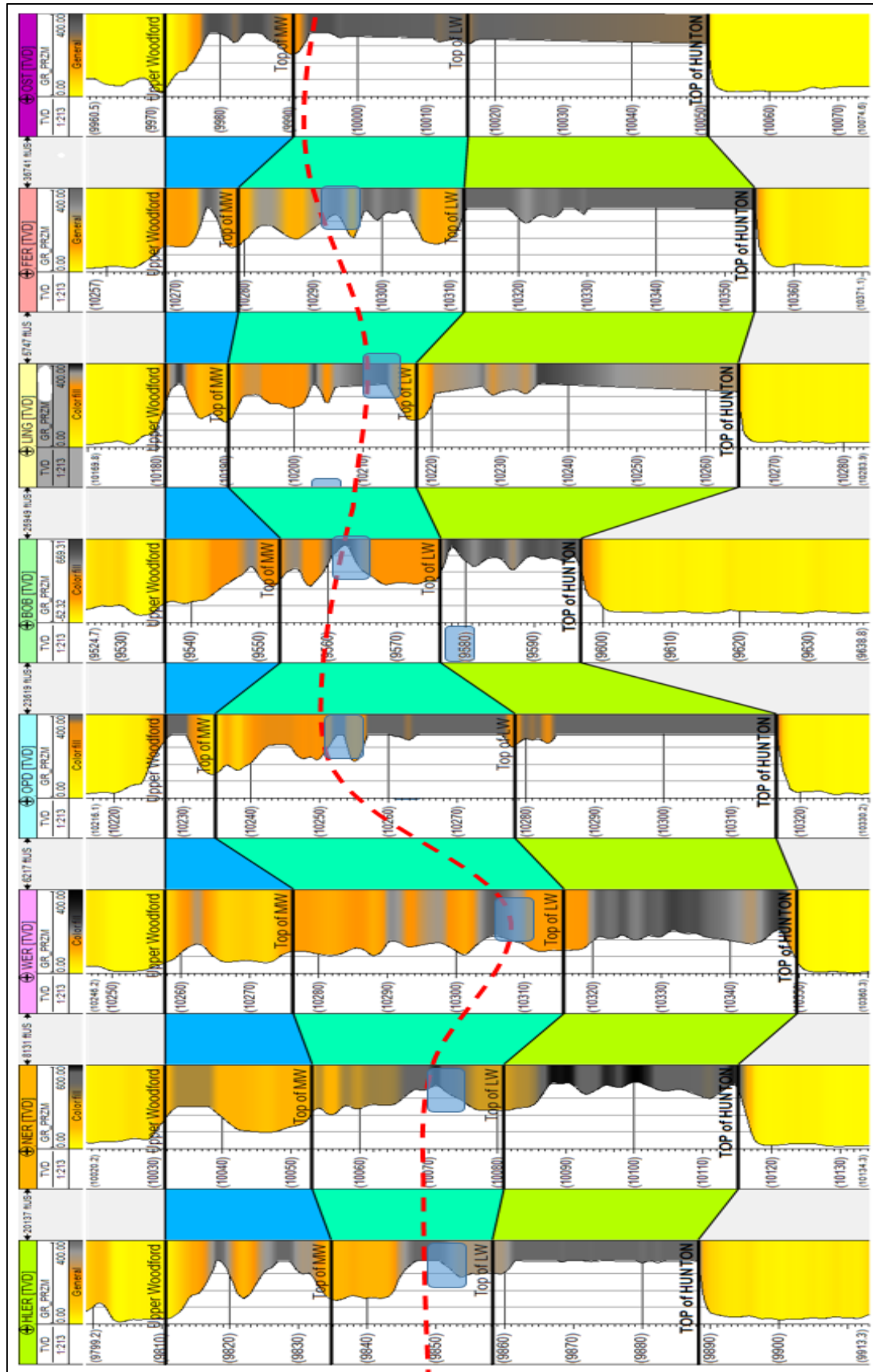


Figure 4.2 Woodford Shale lithology (Gamma-ray) log correlation across eight (8) wells in the study area. The topmost formation is the Osage group and Hunton formation at the base. Flattened on top of upper Woodford Shale and segmented as upper, middle and lower (blue, cyan and green). The Woodford Shale formation has an average thickness of 100ft and the condensed section (the red dash lines) is seen in the middle Woodford correspond to the global Frasnian-Famennian boundary.

4.2 Petrophysical Analysis

Reservoir properties necessary for unconventional Woodford Shale characterization includes organic content, geomechanical properties, and elastic properties (Slatt et al., 2012). In this section, reservoir and completion qualities are investigated using gamma-ray Parasequence (GRP) and stiffness analysis from well-log data. From previous results in section 4.1, I identified the middle Woodford Shale as the interval with the highest TOC because of the presence of the condensed section denoted by the peak in the Gamma-ray profile across the entire Woodford Shale interval. A distinctive geomechanical attribute seen in the middle Woodford Shale outcrop is the intensity of vertical fracture sets which is a function of its lithology (cherty), bed thickness and regional stress or tectonics. Stiffness is a measure of the fracture intensity of a material or medium which directly determines its anisotropy property. I also investigate roles elastic properties like velocity play in delineating zones with low or high fracture intensity using well-log sonic data.

4.2.1 *Stiffness*

From well-log data, cross-plot of Young's modulus and Poisson's ratio is used to estimate the stiffness (formally referred to as brittleness indicator) of a material or interval. This is a geomechanical property measured and computed from well-logs (equation 3.1 and 3.2).

Cross-plots in Figures 4.4 and 4.5 help to analyze the stiffness distribution of the Woodford Shale subdivisions across each well in the study area and also a display of histogram plots for both axes to ascertain data-points distribution. Data-points from the middle Woodford Shale are situated towards the stiff area of the plot while data-points from lower and middle Woodford Shale are mainly situated at the less stiff region. Interpretations from the two figures, the cross-plots identify with Galvis et al., (2018) postulations which state that the middle Woodford Shale is the stiffest

interval (stiffness previously termed as most brittle) due to mineralogy but mainly the presence of intercalations of thin shale and cherty beds (Zhang, 2019). Hence, anisotropy analysis is reliable in delineating zones of high fracture intensity within the Woodford Shale subdivisions.

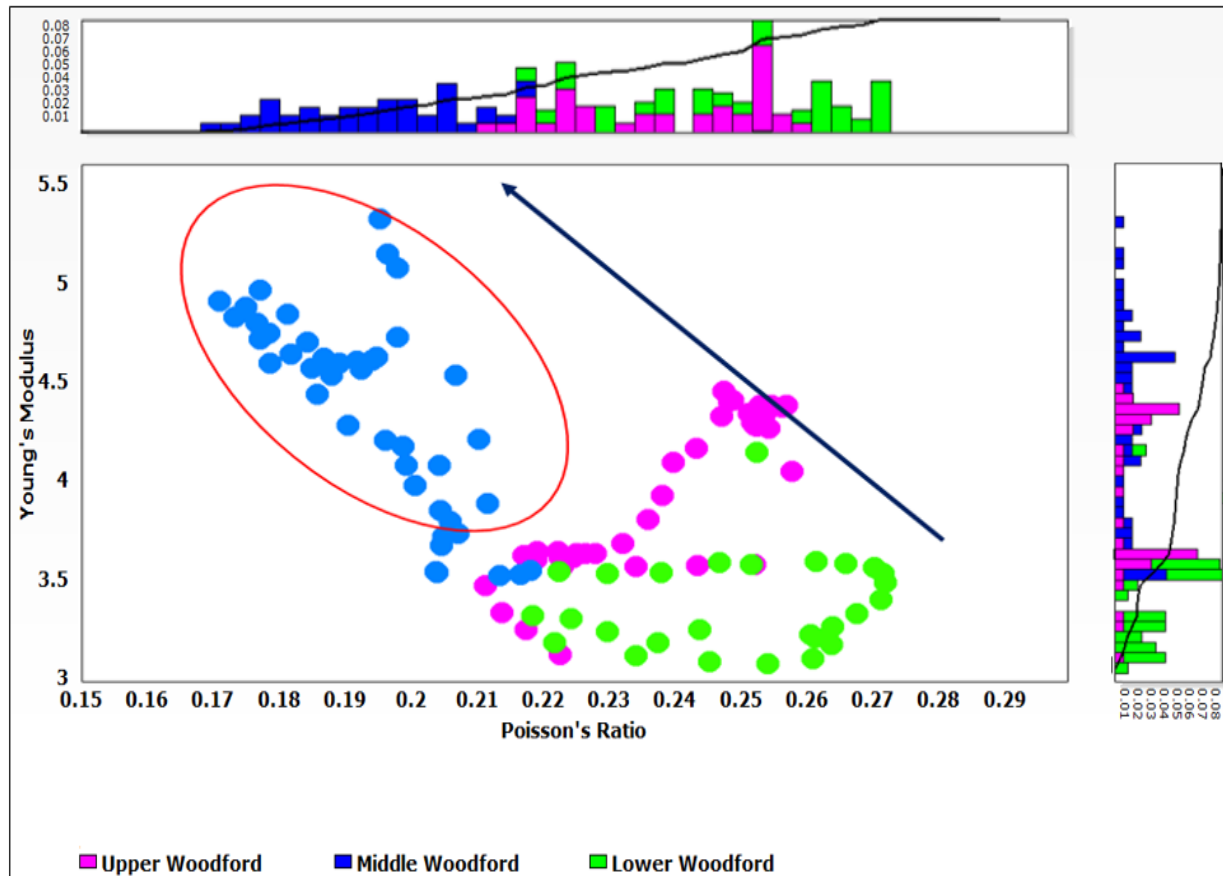


Figure 4.3 A cross-plot of Young's modulus and Poisson's ratio for well 'WER' with datapoints from the upper, middle and lower Woodford formation. There is an inverse relationship between the two parameters, but more importantly, the subdivisions are clearly delineated. The middle Woodford Shale having the highest Young's modulus value is the stiffest of the three Woodford Shale sections.

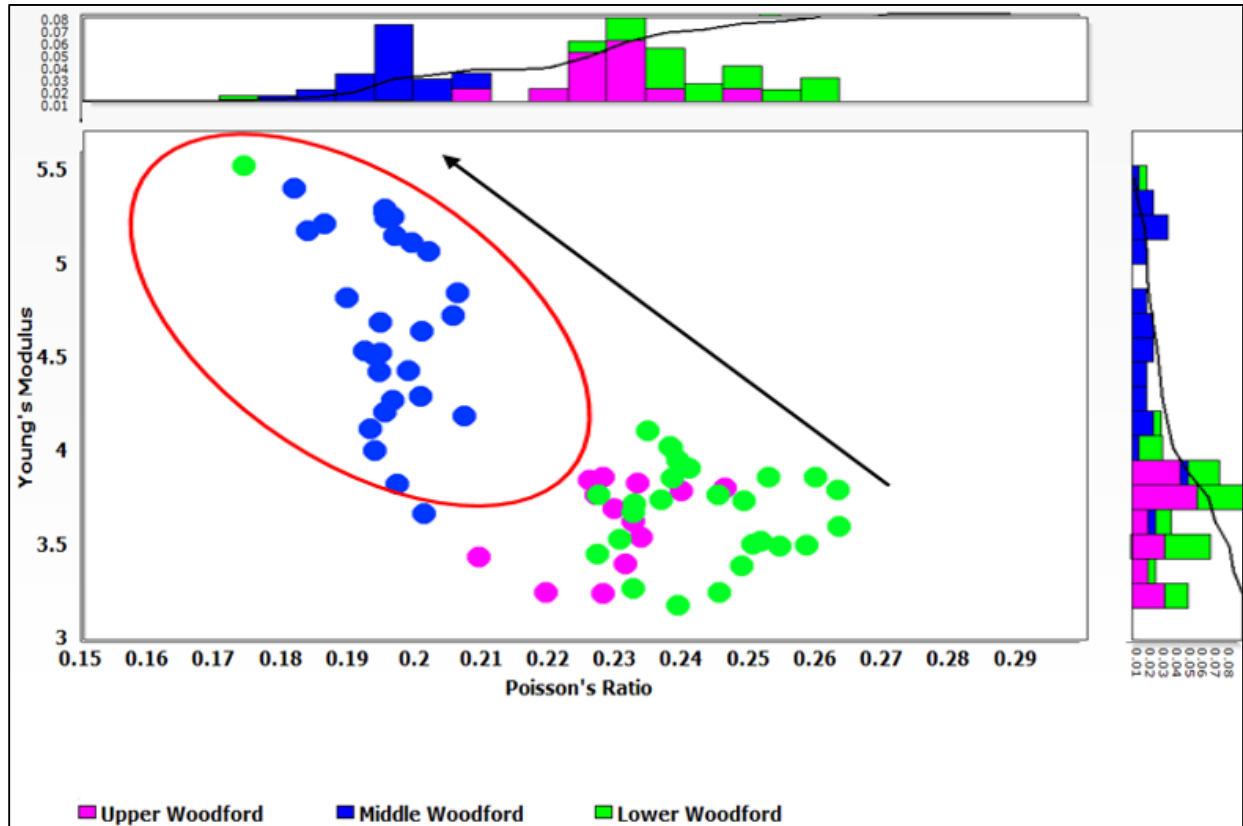


Figure 4.4 A cross-plot of Young's modulus against Poisson's ratio for well 'BOB'. The two histograms clearly delineate the middle Woodford Shale as the stiffest and the least ductile. The stiffness attributes points to the fact that it is the most fractured interval of the three Woodford Shale formations.

4.3 Seismic Inversion

With seismic inversion, I delineated the properties of the whole Woodford Shale including the total thickness, lateral heterogeneity, and P-impedance from seismic volume. In addition to seismic data preconditioning such as migration stretch compensation and spectral balancing, the seismic volume was also corrected to a zero-phase volume before inversion.

4.3.1 Inversion Process

To start the model-based inversion analysis, an initial P-impedance background model was built using three (3) wells ('NER', 'WER', and 'OPD') within the seismic survey area. The wavelet extracted from well-log is used to convolve input seismic volume with the background model. The commercial software package used affords the options of creating impedance constraints and the number of iterations to perform. With these options, I minimize the difference between the seismic volume and P-impedance initial model. An analysis window is used to confirm the accuracy of the inversion along the well as seen in Figure 4.6. There is a good correlation between the synthetics and the seismic trace with an error plot of 7%.

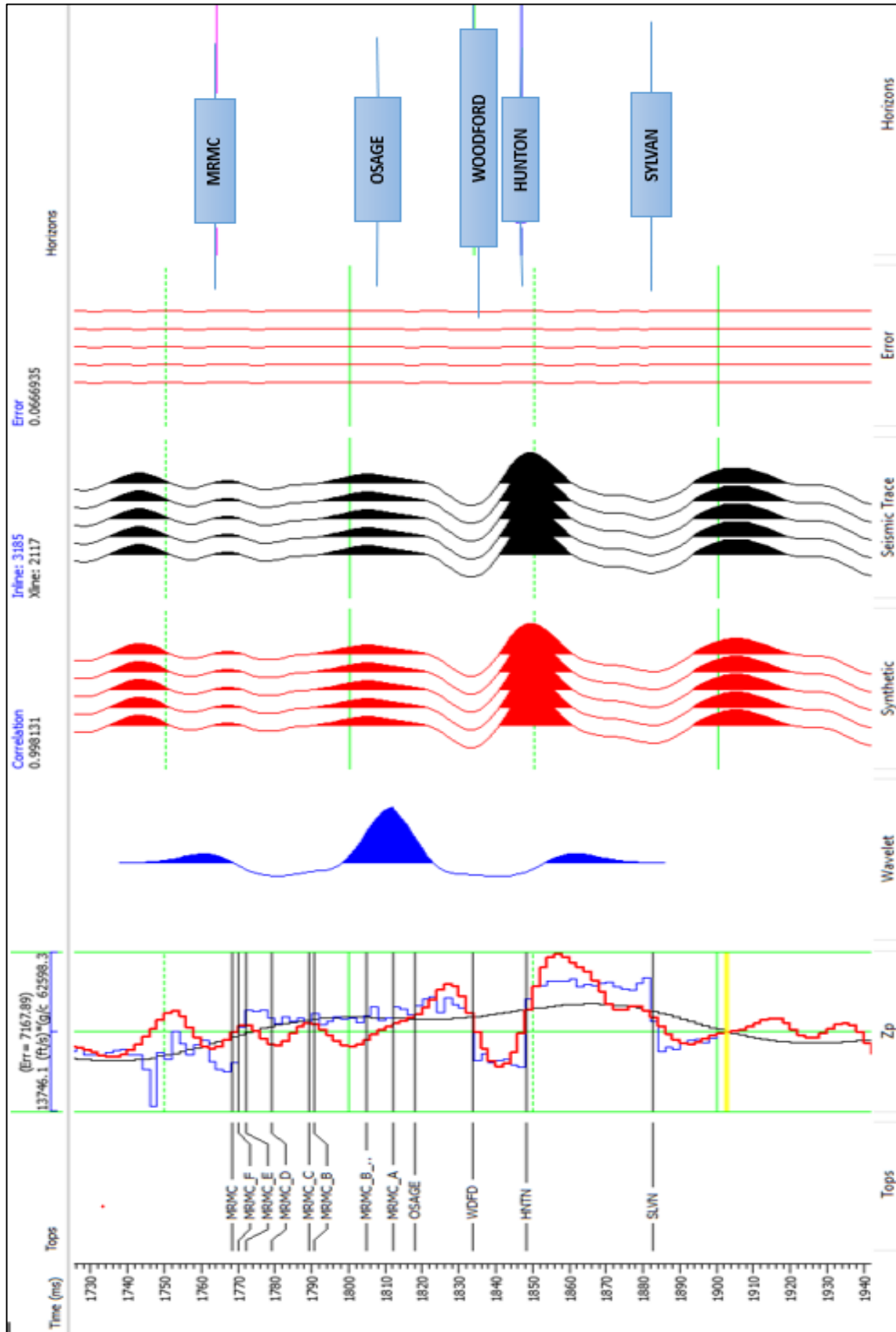


Figure 4.5 Seismic inversion analysis window. The correlation between the trace and the synthetic is quite good and error analysis verifies that with an error margin of 6.67% during the inversion process. In the error analysis column, the black curve is the initial model, the blue curve is acoustic impedance from well-logs, and the red curve is the synthetic curve. After ten (10) iterations, the error was minimized to 6.67%.

During the inversion procedure, a couple of estimation or assumptions were made; such as wavelet extraction, absolute phase of the seismic volume and the initial background model. These make the derived inversion volume a non-unique solution. Nonetheless, I ensure thorough steps are taken during the inversion analysis in order to produce an efficient inversion volume.

4.3.2 Seismic Inversion: Results, Resolution, and Tuning Effect

The middle Woodford Shale is about 40 ft thick, with little or no acoustic contrast with adjacent Woodford Shale subdivisions. I investigated the vertical seismic resolution limit of the bandlimited seismic volume in resolving the top and base of an approximately 100 ft thick Woodford Shale with a velocity of 11,000 ft/s.

At a dominant frequency of 55Hz, the Woodford Shale formation corresponds to one-fifth of the seismic wavelength ($\lambda/5$). Hence the spectrally broadened seismic volume can constructively resolve top and base of the Woodford Shale formation as described in a wedge model in Figure 4.7 and visualized through the vertical seismic slice (Figure 4.8). However, adopting the conventional Widess (1973) proposition, imaging a 40 ft middle Woodford Shale formation (less than $\lambda/5$) will be impossible due to the thickness and low reflection coefficient between its overlying and underlying upper and lower Woodford shale interval. Efforts to further amplify the already boosted high frequency content will diminish the signal to noise ratio of the seismic data.

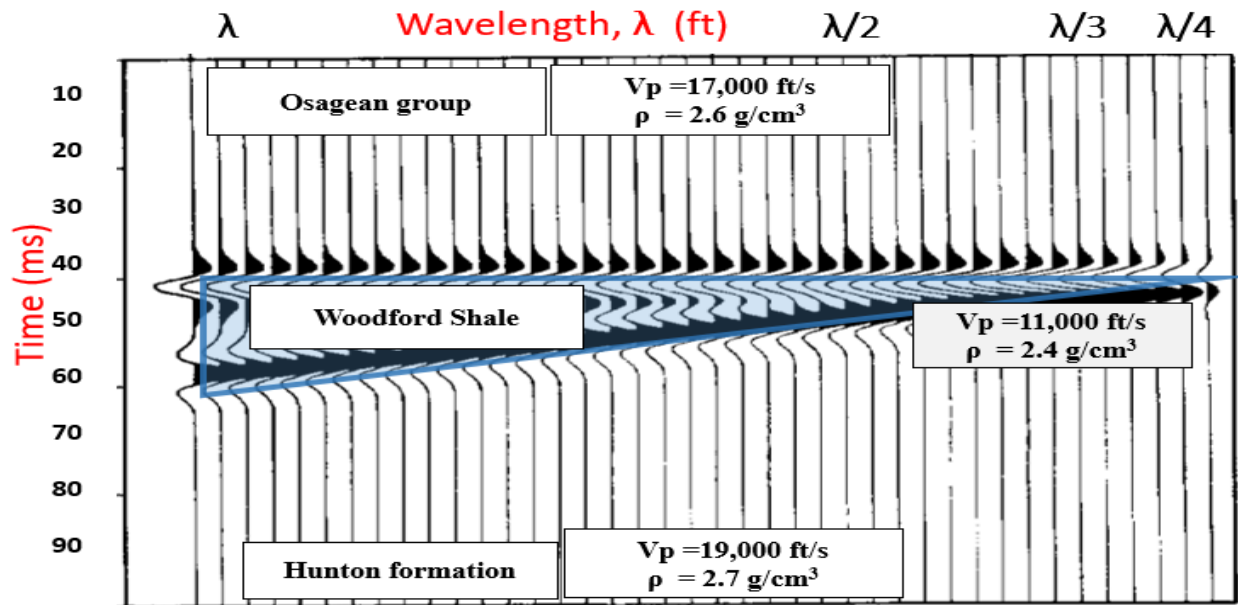


Figure 4.6 A seismic resolution study of the Woodford Shale using Widess's (1993) wedge model showing that the limits to vertical resolution for a 45 Hz wavelet is about 100 ft for a velocity of 11,000 ft/s. Fortunately, after spectral balancing, our data has useful information up to 80 Hz, thereby increasing the resolution.

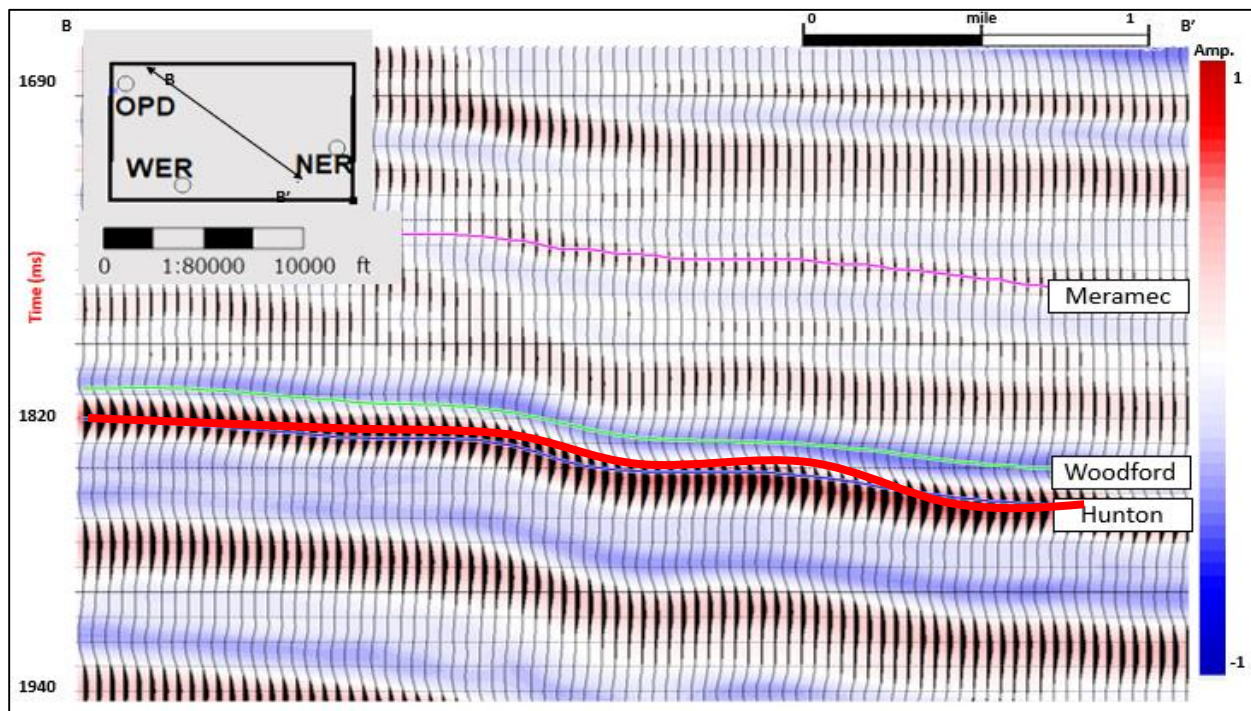


Figure 4.7 A vertical view of the seismic volume line BB' shown in inserted map (top right). From the traces, the Woodford Shale is clearly identified as a strong trough (the cyan pick) overlying the Hunton formation strong peak (the red pick). It corresponds that the thickness of the entire Woodford Shale is approximately $\lambda/5$.

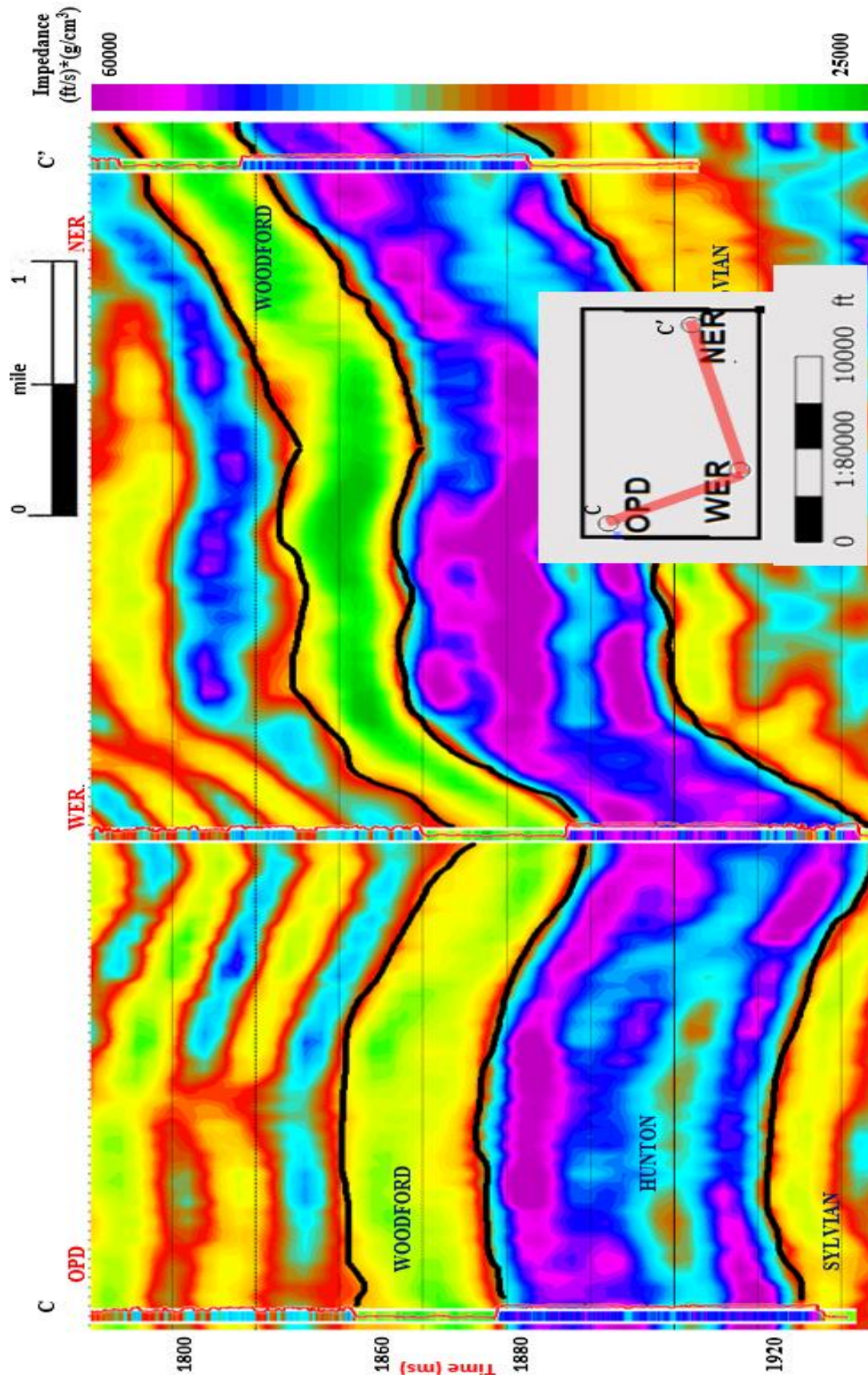


Figure 4.8 A vertical slice through the P-impedance volume (along line CC' in inserted map) connecting wells OPD, NER, and WER. The lower impedance of the Woodford Shale underlies the Osage formation and overlies Hunton group. The inversion result was able to resolve the entire Woodford Shale but does not clearly delineate the middle Woodford Shale or other subdivisions.

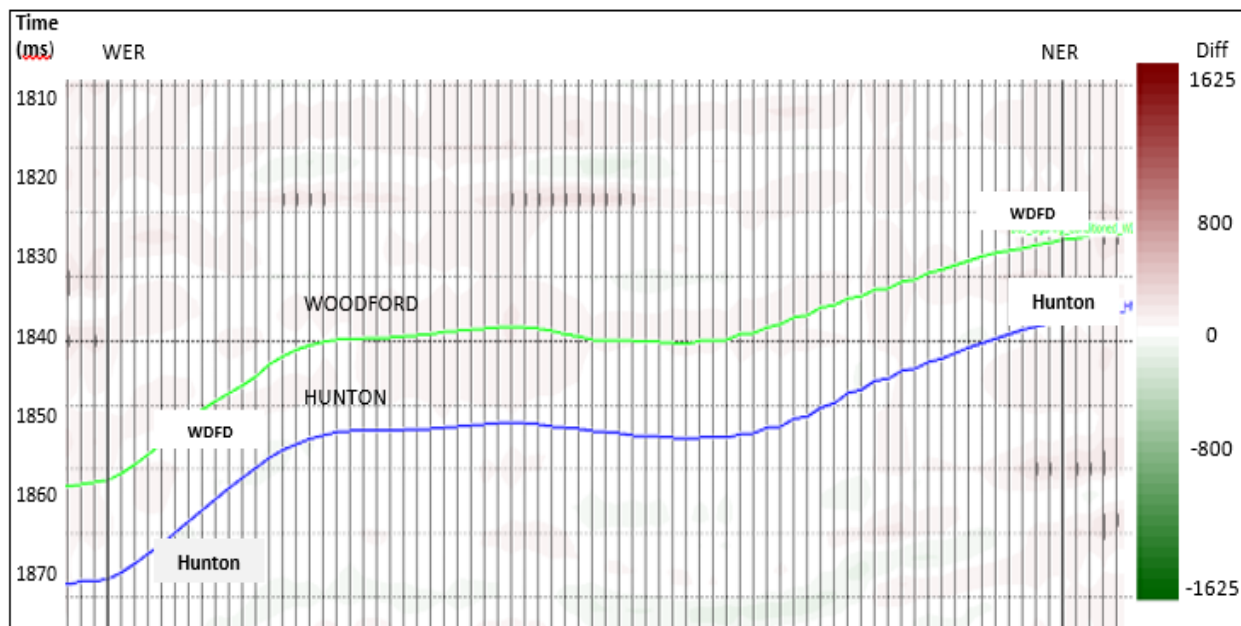


Figure 4.9 A plot showing the difference between the measured seismic data and the synthetic traces corresponding the inverted P-impedance model for the line connecting wells ‘NER’ and ‘WER’. The amplitude scale is the same as the seismic line shown in Figure 4.11 and indicates a very small residual.

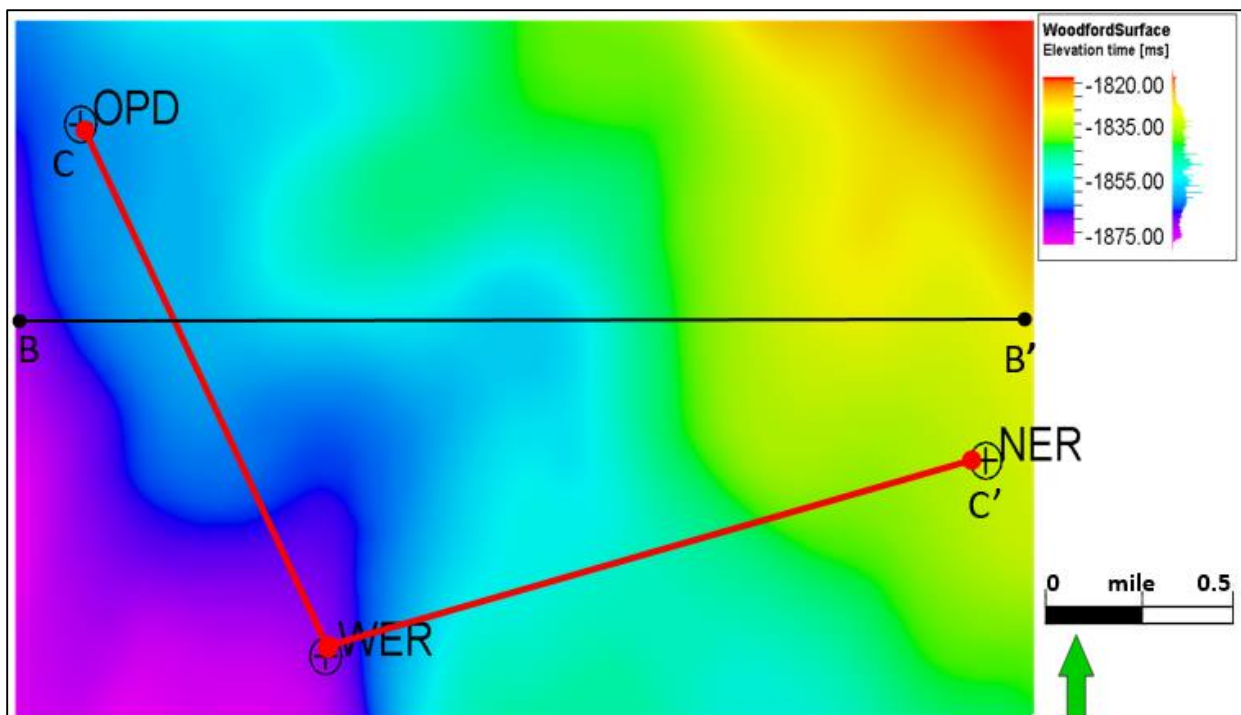


Figure 4.10 Time structural map of top of Woodford Shale formation. The depth of the top Woodford increases from northeast to southwest. Location of profiles BB’ and CC’ discussed in figures 4.14 and 4.15. This figure corresponds to the trend seen in the Anadarko basin geology literature.

Figure 4.9 shows a P-impedance inversion volume created across the study area. The Woodford Shale formation, a 15 ms isochron profile is clearly resolved with impedance value as low as 24,000 ft/s*g/cm³ and as high as 35,000 ft/s*g/cm³. To quality control the inversion procedure, the synthetic volume was subtracted from the input seismic, only a minimal difference across the entire Woodford formation was noticed as seen in Figure 4.10.

The variation in thickness or lateral prediction is delineated in the isochron map in Figure 4.12a as the Woodford Shale in wells 'WER' and 'OPD' are relatively thicker than that of well 'NER'. Within the Woodford subdivisions, there is a relatively small acoustic impedance range as seen. Based off of the impedance values, I propose that regions with obvious low impedance value are zones with presence of high fracture intensity (filled or opened) which reduces the density of the material or medium. The perimeter around well 'NER', east of well 'WER', and southeast of Well 'OPD' with low P-impedance is speculated to have a high fracture intensity. However, using only P-impedance volume to predict the presence of fracture intensity can be misleading, as we cannot ascertain if the fractures have effect on the sonic log of the wells during well-logging. As a result, AVAz analysis will be important to ascertain location, intensity and the orientation of the fracture-sets across the entire Woodford Shale formation.

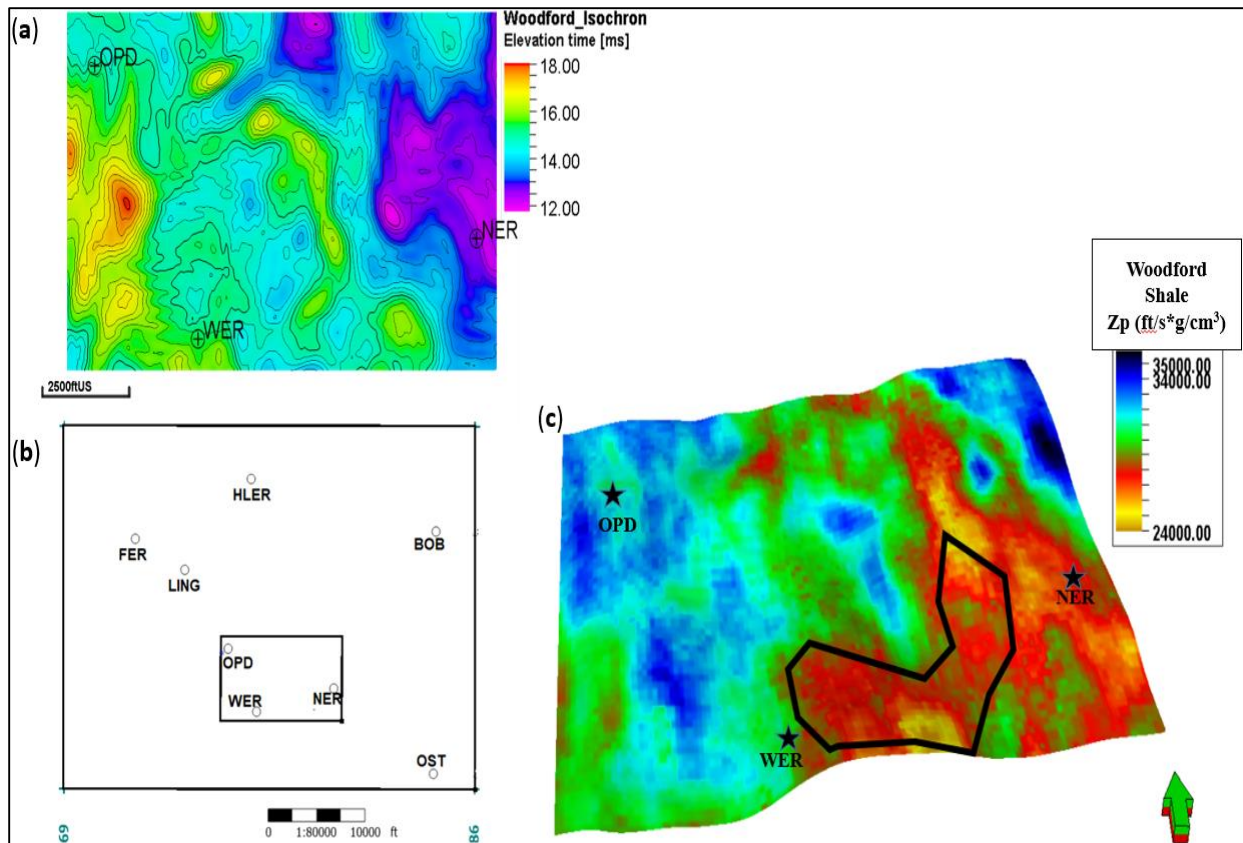


Figure 4.11 (A) An isochron map of Woodford Shale. Generally, the formation is thicker within the east area of the map. (B) Map of the study area showing location of the wells, the small black rectangle is the seismic volume area (C) P-impedance stratal slice through the middle Woodford Shale approximately 15 ms below the top Woodford Shale horizon. The black polygon indicates an area of low impedance which may be due to several causes, one of which is the area being highly fractured. The region within the polygon will be further investigated using AVAz analysis.

4.4 AVAz analysis and Inversion

Fracture intensity or stress attributes are resolved from the Woodford Shale interface analysis using variation in P-wave reflectivity with respect to azimuth and offset. Offset information necessary for this interpretation is within the range of critical angle of incidence of the Woodford Shale which is about 40^0 at approximately 9000 ft offset. Seismic reflectivity is estimated using Ruger's (1997) approximation which incorporates the anisotropy parameters into the reflection coefficient computation across the entire. We use this seismic reflectivity information to run an anisotropic inversion and extract anisotropy gradients B_{aniso} which measures fracture intensity and azimuthal isotropy, φ_{iso} which resolves the orientation of vertical fractures or regional stress.

With the aid of the AVAz workflow from the Hampson-Russell software, I assessed traces along offset information [at one (1) inline and one (1) crossline component] approximately 110 ft by 110 ft area of the seismic volume at the Woodford Shale horizon time window as seen in Figure 4.13 to Figure 4.18 . Applying Ruger's (1997) approximation, at well 'NER', I compute the AVAz curves in order to visualize the amplitude of reflectors at Woodford Shale horizon time (approximately 1.8 sec) along the traces as seen in Figure 4.13 and 4.15 and 4.17. Then, I interpreted the stress or vertical fracture intensity from the Ruger's (1997) AVAz approximation plot. This analysis is just for a well location visualization.

For Figure 4.14, 4.16, and 4.18, the curves are Ruger's AVAz approximation of the traces reflector amplitude which is a best fit curve for the data-points seen which represents amplitudes of the seismic traces reflector at Woodford horizon time. The sinusoidal pattern or trend of the curves is a function of the horizontal stress or fracture intensity at that location (Chopra and Marfurt, 2019). Well 'NER' location in Figure 4.14 is the most anisotropic region within the Woodford Shale formation of the three wells with a B_{aniso} of 16000 with azimuthal orientation φ_{iso} at 80^0 with

respect to 0^0 north. This is followed by the location at well 'OPD' (Figure 4.16) with B_{aniso} of 12840 with ϕ_{iso} at 70^0 with respect to 0^0 north, followed by well 'WER'. Interpreting from the value of the anisotropy gradient B_{aniso} , amongst the three well locations, the region around well 'NER' have most fractures intensity and the dominant fracture-set is in the E-W or NE-SW direction. The magnitude of the sinusoidal pattern of the AVAz curves is a result of variation in P-wave reflectivity across the azimuth and a reflection of intensity of vertical fractures or stress.

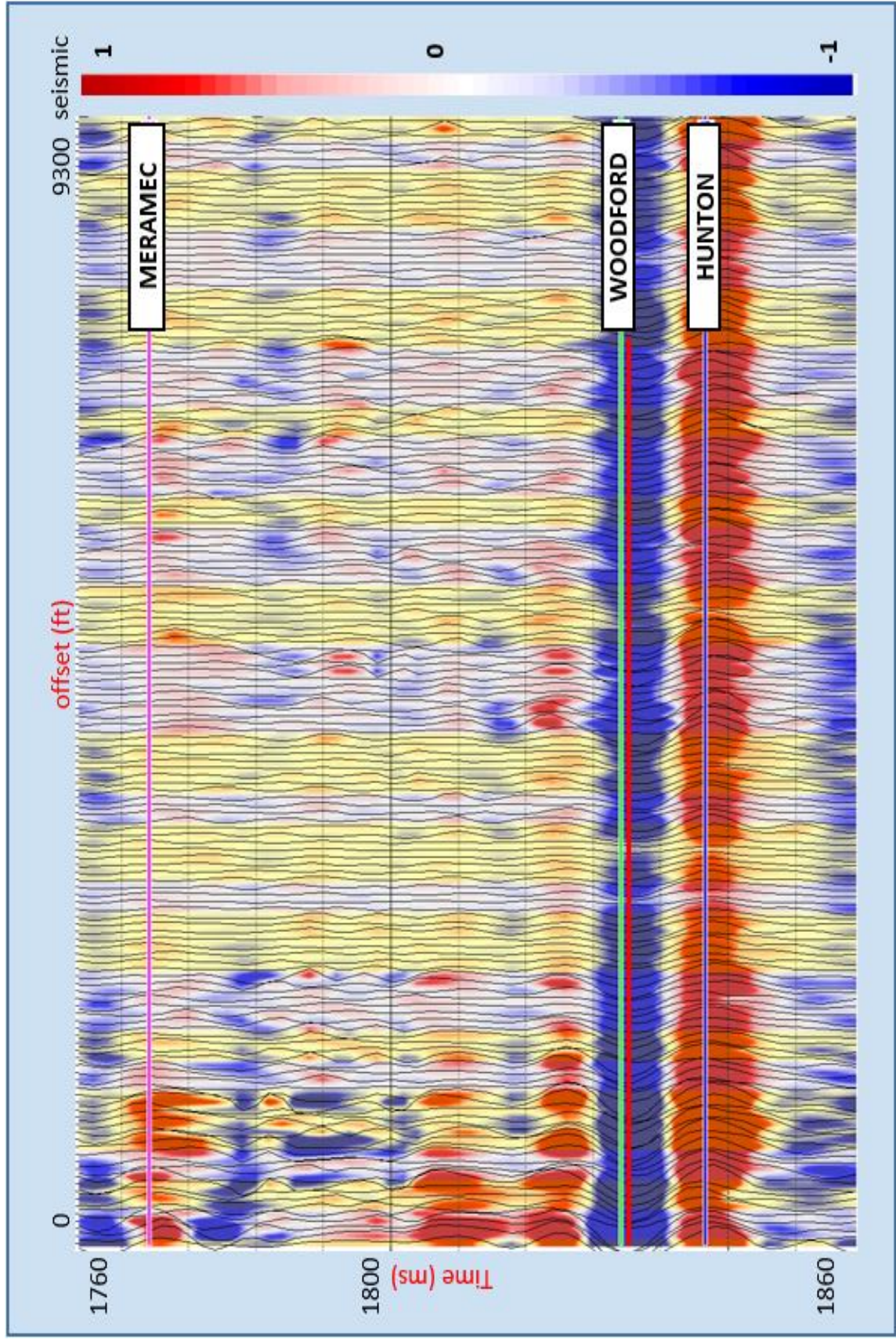


Figure 4.12 A seismic CDP gather time-window at well 'NER' location showing the Woodford Shale time (1840ms) interval (green line) and the trace amplitudes used for AVAz analysis. Notice the amplitude of the Woodford reflection in blue colour reduces as the offset increases. The magnitude of the decline is higher than that of Hunton below.

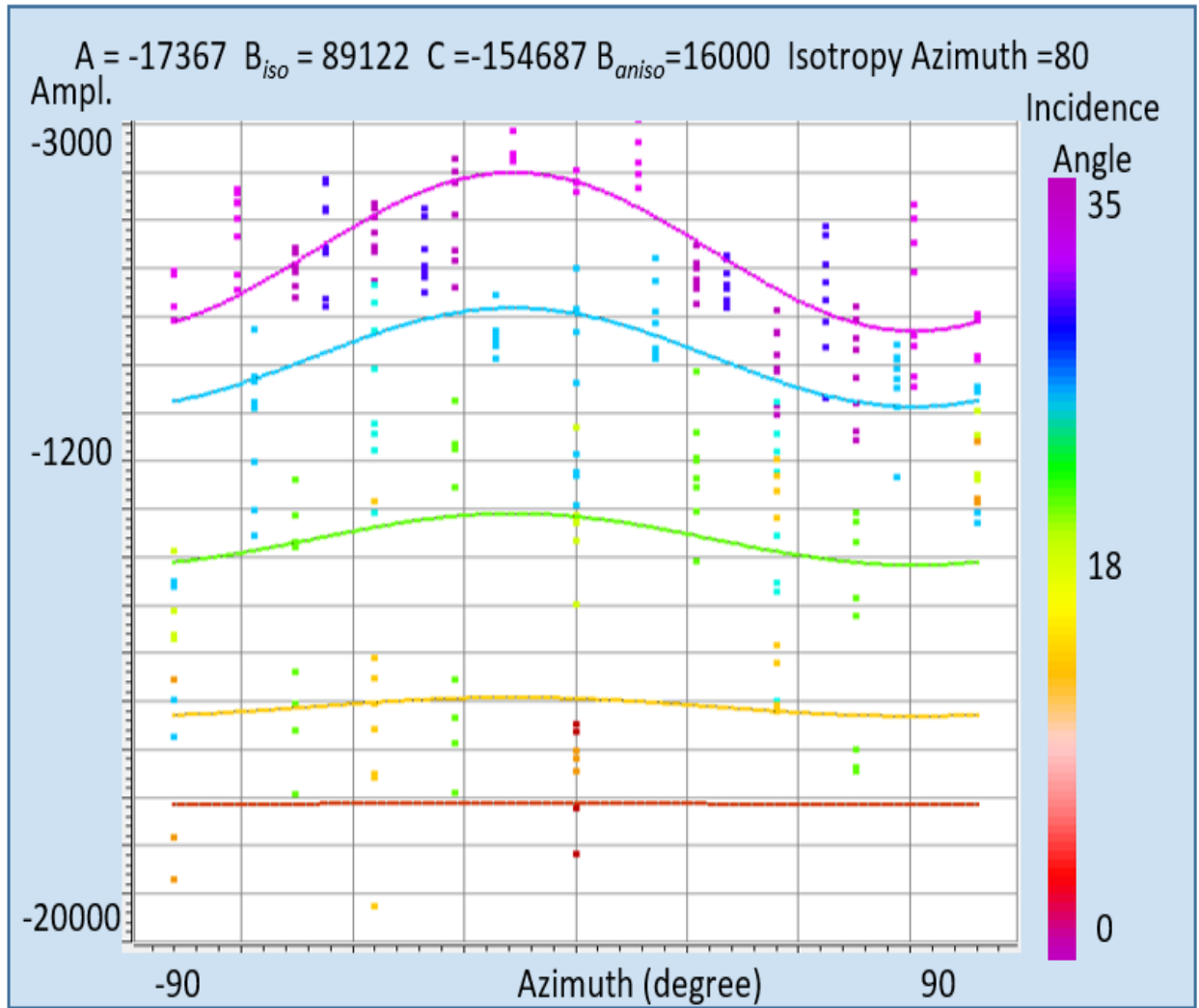


Figure 4.13 A AVAz window analysis at well 'NER' showing the predicted AVAz curves from Ruger approximation matching the data-points of the seismic traces at well 'NER'. Amplitude of the reflection coefficient is plotted against azimuth. The predicted curve represents the approximation of the reflection coefficient along azimuth for different incident angles (i.e. 0° , 7° , 14° , 21° , 28°). Notice the separation of the curves and the sinusoids pattern along azimuth compared with subsequent figures. The magnitude of the B_{aniso} is estimated at 16000. The isotropy azimuth is 80° .

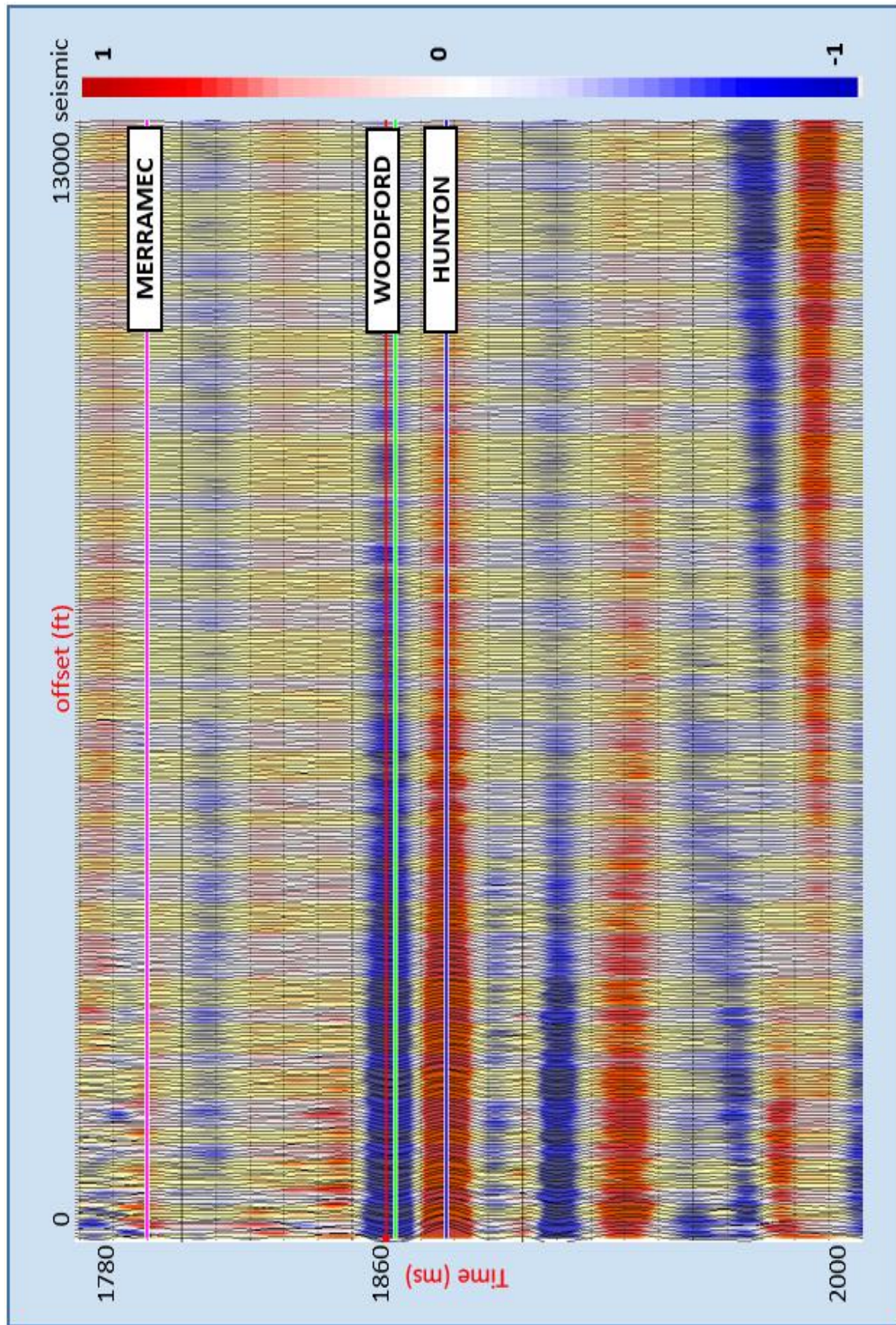


Figure 4.14 A seismic CDP gather time-window at well 'OPD' location showing the Woodford Shale time (1840ms) interval (green line) and the trace amplitudes used for AVAz analysis. Notice the amplitude of the Woodford reflection in blue colour reduces as the offset increases. The magnitude of the decline is higher than that of Hunton below.

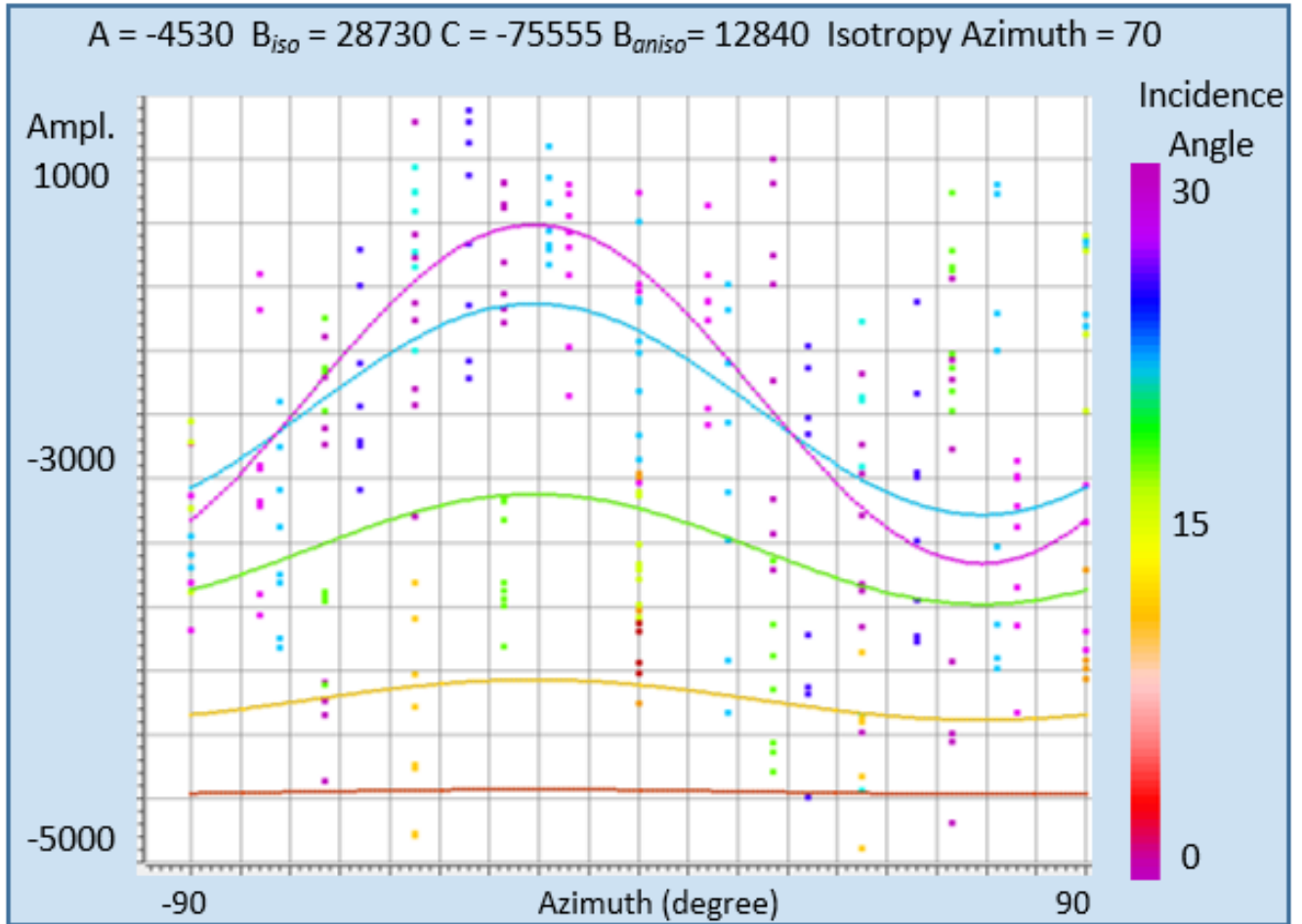


Figure 4.15 A AVAz analysis window at well ‘OPD’ showing the predicted AVAz curve using Ruger approximation. Amplitude of the reflection coefficient is plotted against azimuth. The predicted curve represents the approximation of the reflection coefficient along azimuth for different incident angles (i.e. 0° , 7° , 14° , 21° , 28°). The data-points are fairly approximated by the curves. Notice the separation of the curves and the sinusoids pattern along azimuth. At this location, the B_{aniso} is estimated at 12840. The isotropy azimuth is 70° .

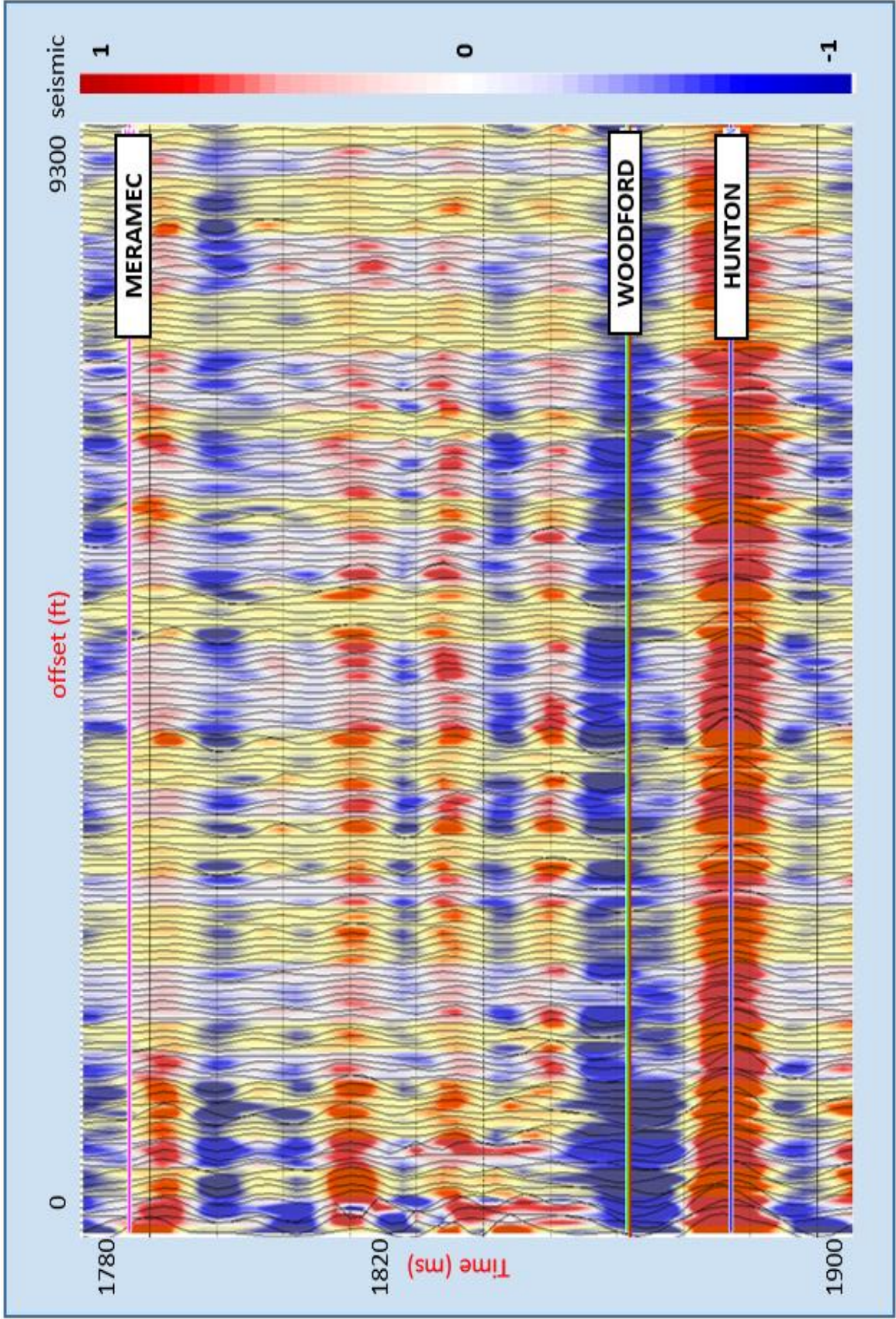


Figure 4.16 A seismic CDP gather time-window at well 'WER' location showing the Woodford Shale time (1840ms) interval (green line) and the trace amplitudes used for AVAz analysis. Notice the amplitude of the Woodford reflection in blue colour reduces as the offset increases. The magnitude of the decline is higher than that of Hunton below.

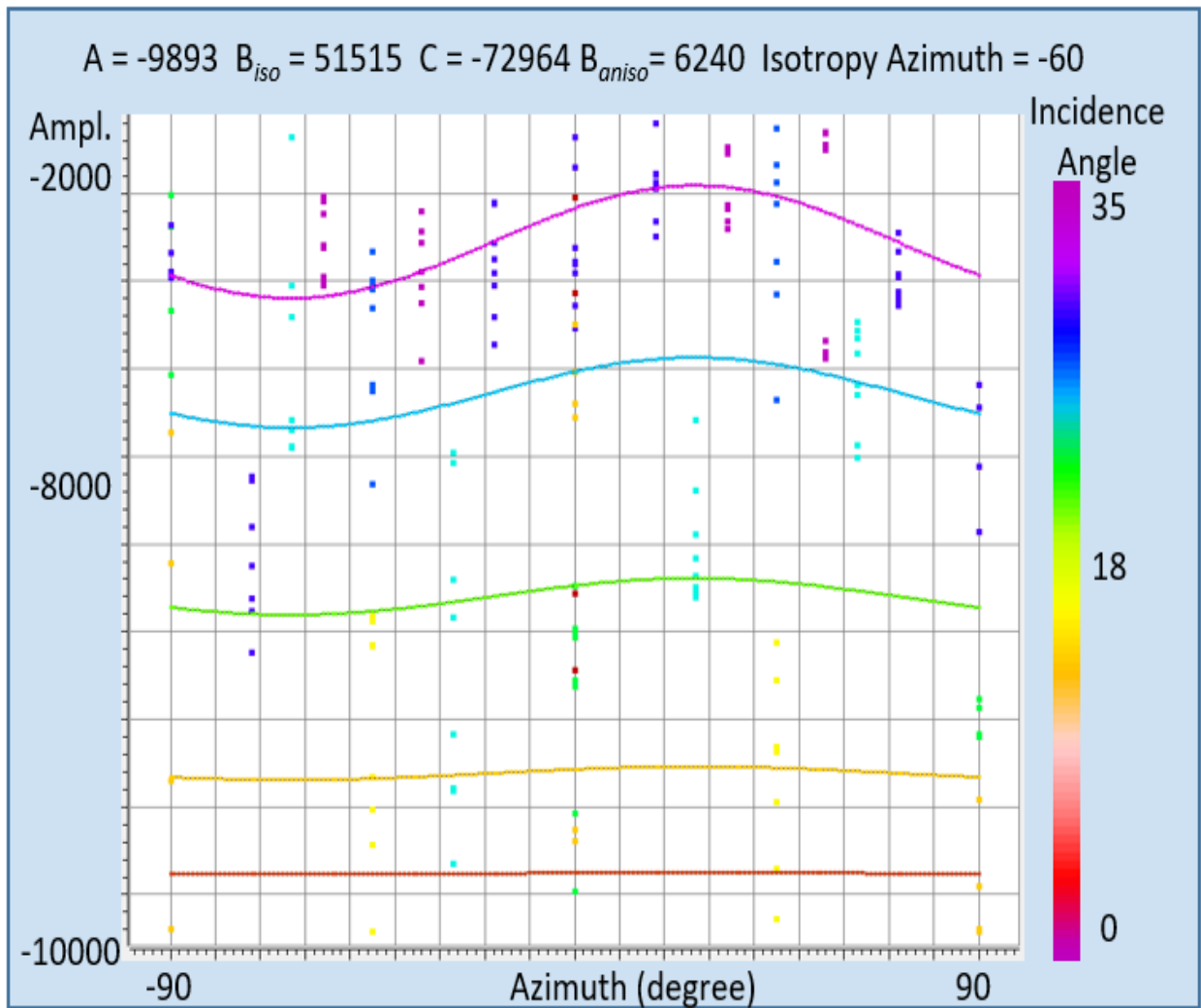


Figure 4.17 AVAz window analysis at well 'WER' showing the predicted AVAz curves from Ruger approximation matching the data-points of the seismic traces at well 'WER'. Amplitude of the reflection coefficient is plotted against azimuth. The predicted curve represents the approximation of the reflection coefficient along azimuth for different incident angles (i.e. 0°, 7°, 14°, 21°, 28°). Notice the separation of the curves and the sinusoids pattern along azimuth. The magnitude of the B_{aniso} is estimated at 6240. The isotropy azimuth is -60°.

4.4.1 AVAz Inversion and Seismic Attributes.

To estimate fracture intensity aurally for the entire survey area, I compute an anisotropic inversion for the Woodford Shale formation using the near-offset Ruger (1997) parametrization. The output are the anisotropy gradient volume and the azimuthal isotropy volume as seen in Figure 4.19 a and b. The area within the polygon in Figure 4.19a represents a region with high values of anisotropy gradient of about 15,000 which is interpreted to indicate a high fracture intensity. The same polygon in Figure 4.19b corresponds to a region where the dominant fracture-sets are in the $\sim 90^\circ$, E-W orientation and, $\sim 65^\circ$, NE-SW orientation. A co-rendered image of the two attributes in Figure 4.20 shows a good match. These dominant fracture-sets in the polygon conforms to those seen in the middle Woodford Shale outcrop with bitumen filling in the McAlister Quarrey, Ardmore Oklahoma. Ghosh (2017) has shown these fracture-sets to be the primary natural fracture-sets based on cross cutting relationships, terminations, and fracture fill.

Figure 4.21 shows the anisotropy vectors (hypothetized fracture sets) plot for the survey area showing the magnitude and direction of the hypothesized fracture-sets. Figures 4.22 and 4.23 corrender these vectors with the anisotropy gradient B_{aniso} and azimuthal isotropy ϕ_{iso} to provide a descriptive geomechanical image of the middle Woodford. I hypothesize that these inferred E-W/NE-SW fractures resolved in the study area correspond to the bitumen-filled fractures seen in the outcrop. Coincidentally, the three wells drilled are sited within high anisotropy locations.

Bends, folds, and flexures in the Woodford Shale are delineated from curvature attribute (k_{max} and k_{min}). As seen in Figure 4.24, this seismic attribute delineates good surface expressions (domes and bowls) where fractures are likely to exist within the Woodford Shale lithology.

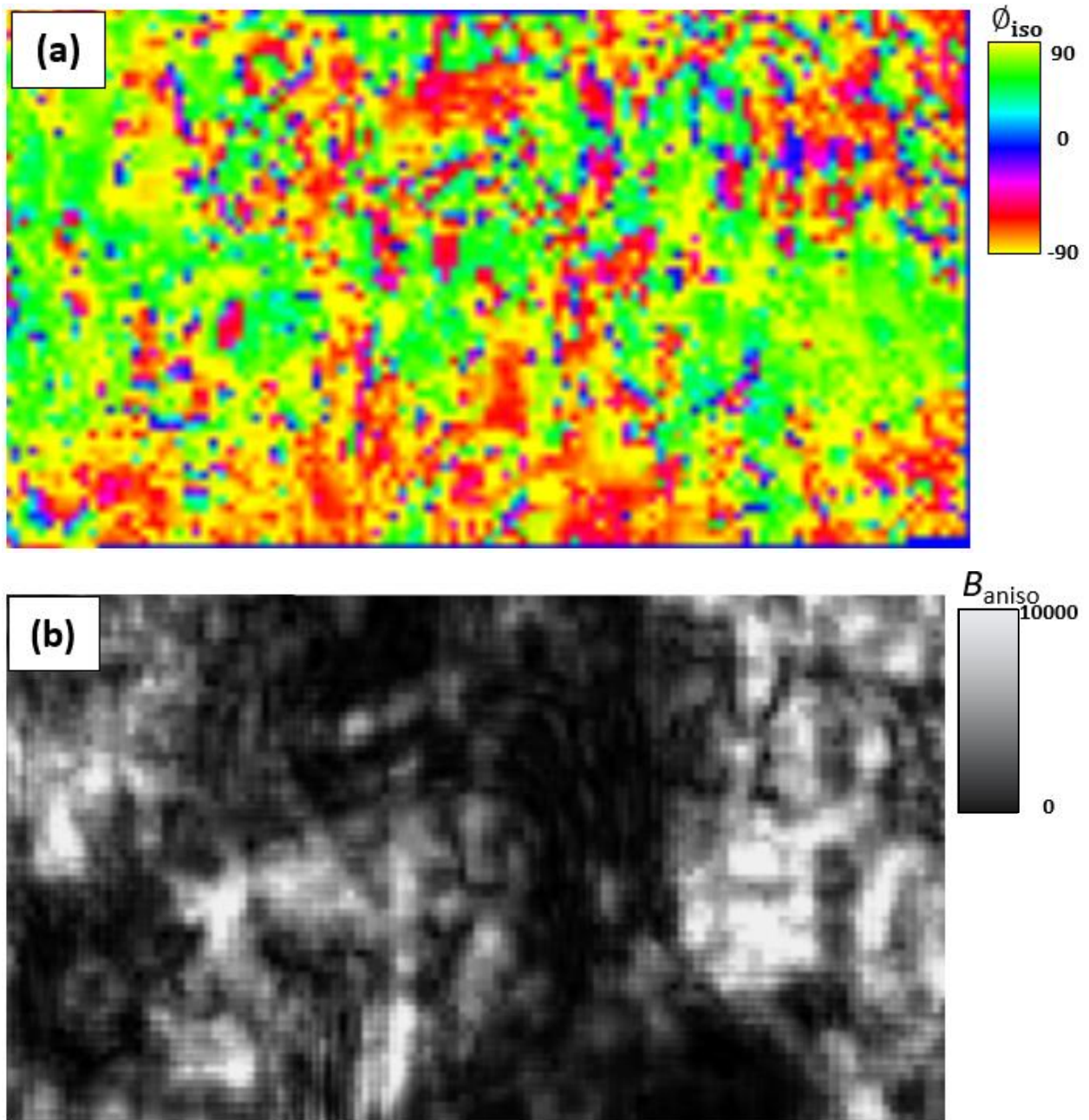


Figure 4.18 Anisotropy inversion results. Stratal slice of the azimuthal isotropy, ϕ_{iso} with 0° north orientation (a) and anisotropic gradient B_{aniso} (b) of the Woodford Shale. The black polygon defines a zone where B_{aniso} is high and the ϕ_{iso} is in the E-W or NE-SW orientation. We hypothesize that the region within the polygon has higher fracture intensity, and perhaps a thicker middle Woodford Shale unit than other regions.

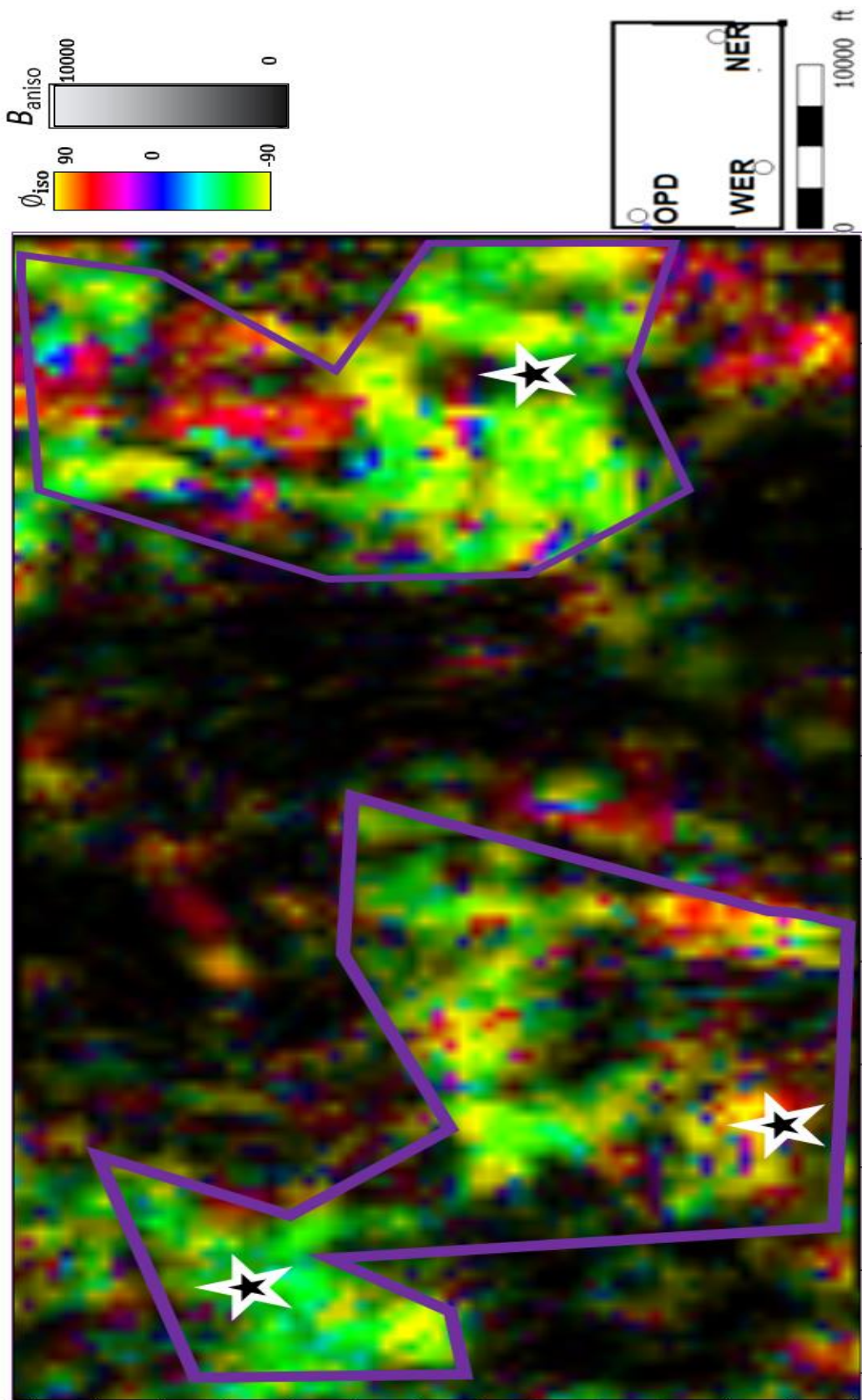


Figure 4.19 Strata slice of anisotropy gradient B_{aniso} using a monochrome black color bar and opacity, overlain with azimuthal isotropy ϕ_{iso} . Areas that appear black are relatively isotropic. There is a correlation between the two volumes as the bright region in the purple polygon matches region with a certain pattern of orientation in the ϕ_{iso} map and the locations of the three wells (located in the star symbols) drilled. The bright region has high magnitude fractures that are in the same orientation as the bitumen-filled fracture-sets seen in the outcrop. Interestingly, the three well locations were situated within the region highlighted.

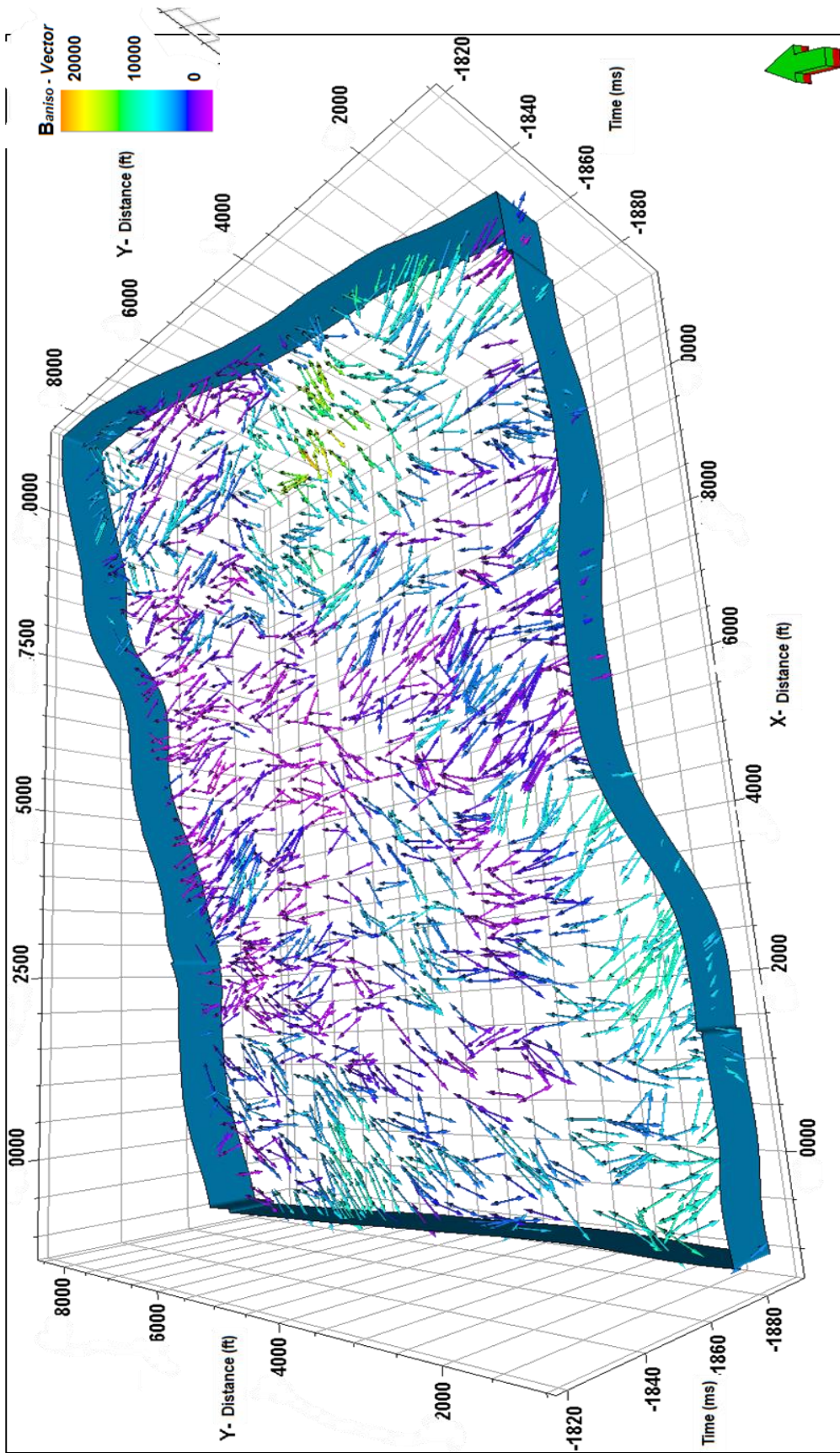


Figure 4.20 A 3D display of the vector plot of Woodford Shale. This is done by resampling the seismic azimuth isotropy and anisotropy gradient geometrically and applying it on 3D vector grid. The arrows indicate the orientation of the fracture or stress while the color of the arrow is the magnitude of the fractures at each location. Regions around well locations ‘OPD’, ‘NER’, and ‘WER’ have high anisotropy gradient compared to other locations. Hence, they have relatively thick middle Woodford formation with fracture-sets in the E-W or NE-SW orientation.

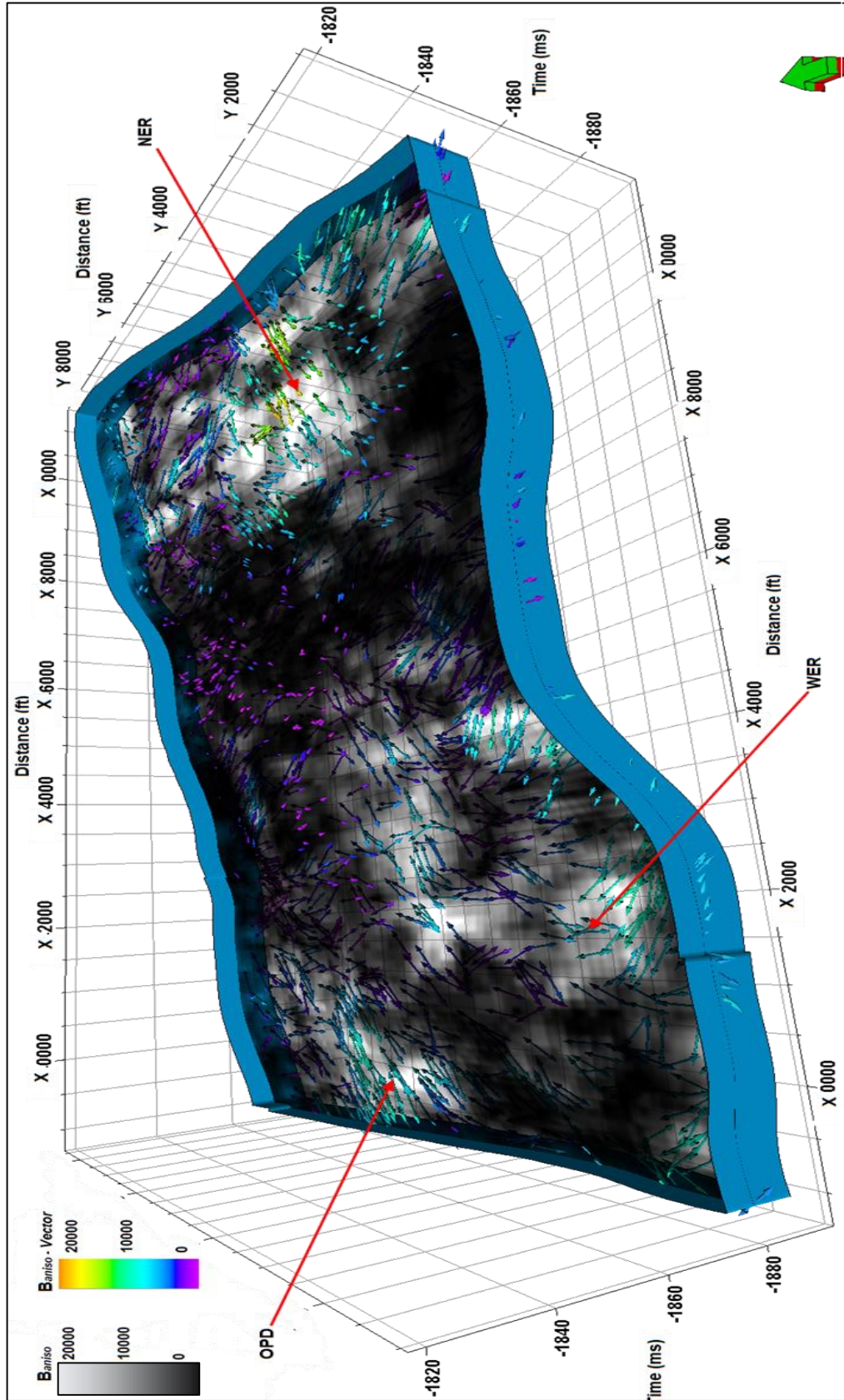


Figure 4.21 A 3D display of the Woodford Shale vector plot co-rendered with anisotropy gradient volume. The bright regions correspond to where there is high gradient while the dim or dark regions are where there is low gradient. Notice that the direction of the vector plot (arrows) where in the bright regions are mostly in the E-W or NE-SW orientation while in the dark regions, the fracture-sets are mostly N-S or NW-SE direction. From previous studies, the E-W and NE-SW fracture-sets in the Woodford Shale are the primary natural fracture-sets embedded with bitumen (Ghosh, 2017).

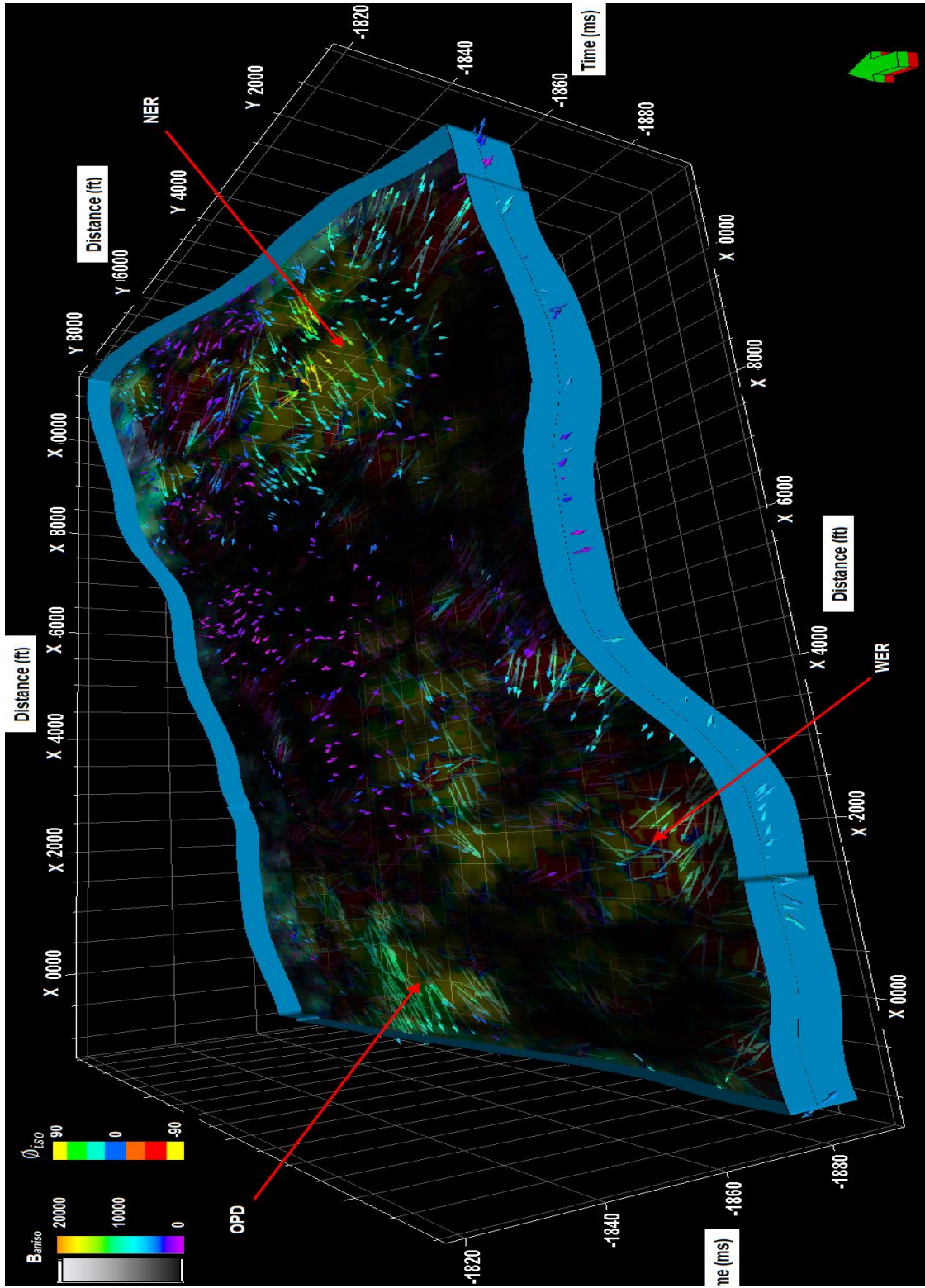


Figure 4.22 A 3D vector plot of Woodford fracture intensity co-rendered with anisotropy gradient and azimuthal isotropy. Here, the well locations are situated around the bright area, and also where the arrows are in the E-W and NE-SW direction, and the magnitude are high. In the background is the ϕ_{iso} orientation between 60° - 90°

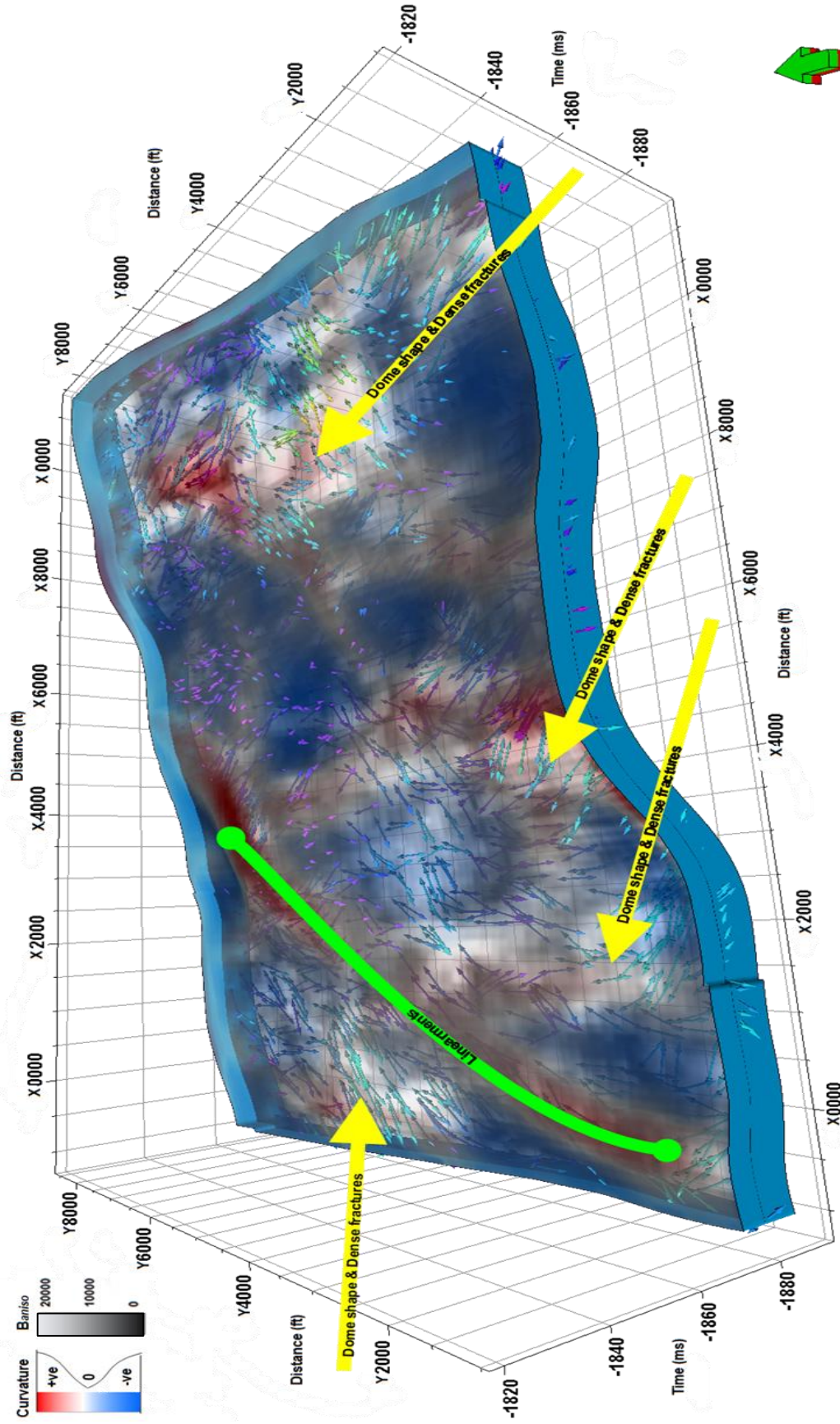


Figure 4.23 A 3D display of the Woodford Shale vector plot underlying curvature co-rendered attributes, K_{max} and K_{min} . The red regions are prominent for dome and anticline features from K_{max} attribute, the blue zone corresponds to regions with bowl and synclinal features from K_{min} attribute. Majority of the bright areas i.e. fracture swarms areas lie within the flexure (red) features highlighted by the yellow arrows. Hence, investigation of fracture intensity using seismic surface attributes is feasible.

5 CONCLUSIONS AND LIMITATIONS

Due to limited geologic information on the analysis of the complete section of the Woodford Shale in the study area, I used a Woodford Shale outcrop, 156 miles away, as a reference lithology profile. This outcrop provides a Woodford Shale geomechanical and fracture model. The stiffness analysis using Poisson's ratio and Young's modulus from well-logs provides a proper delineation of the subdivisions of the Woodford Shale that matched that of the outcrop. From gamma-ray parasequence analysis, I confirm the same lithology stacking pattern exists across both the Anadarko Basin (area of study) and the Ardmore Basin (reference outcrop).

Through deterministic inversion, I used the P-impedance volume to delineate the Woodford Shale from the adjacent Osagean and the Hunton group. Unfortunately, because of the low impedance contrast and limited seismic resolution at 11,000 ft depth, this inversion was not able to resolve any of the 30-ft thick Woodford subdivisions.

My outcrop-based geomechanical framework is that higher fractures and hence higher anisotropy indicates relatively thick middle Woodford formation embedded with fracture-sets embedded with bitumen. Based on the outcrop, I attribute the anisotropy response of the entire Woodford Shale to that of the middle Woodford Shale. AVAz parameters, B_{aniso} and ϕ_{iso} showed highly fractured region have orientation consistent with those fractures with bitumen filling in the distant outcrop. Outcrop analysis showed the middle Woodford Shale also exhibits the highest TOC content and thus exhibits the highest reservoir quality, RQ. The outcrop work also shows the middle Woodford to be the most naturally fractured and stiffest interval, and hence promises to have the highest completion quality. Therefore, for a RQ-CQ resources exploration in the Woodford Shale, the middle Woodford is the target of choice.

Limitations

1. Given the geological and elastic complexities involved (thickness of the middle Woodford and impedance contrast), seismic anisotropy can only resolve regions with relatively thick middle Woodford Shale formation but cannot explicitly resolve a lithology boundary or thickness. Hence, I propose that with improved well-log data, we can distinguish properties of Woodford subdivisions, by generating several realizations and models that can map the intervals through seismic stochastic inversion.
2. Fracture intensity cannot be quantitatively characterized as this approach only provides normalized anisotropy values across the whole Woodford shale interval.
3. The ambiguity of interpreting fracture intensity and unequal horizontal stress is still prevalent, as seismic anisotropy cannot discriminate between the two phenomena.

6 REFERENCES

- Abouelresh, M. and R. Slatt, 2011. Shale depositional processes: Example from the Paleozoic Barnett Shale, Fort Worth Basin, Texas, USA. *Open Geosciences*, **3**(4), 398-409.
- Amsden, T.W., 1967, Silurian and Devonian strata in Oklahoma: Symposium—Silurian Devonian rocks of Oklahoma and environs: *Tulsa Geological Society Digest* **35**, 25-34.
- Amsden, T. W., 1975, Hunton Group (Late Ordovician, Silurian, and Early Devonian) in the Anadarko basin of Oklahoma, *Oklahoma Geological Survey Bulletin* **121**: Norman, Oklahoma Geological Survey, 214 p.
- Backus, G. E., 1962, Long-wave elastic anisotropy produced by horizontal layering: *Journal of Geophysical Research*, **67**, 4427–4440, <http://dx.doi.org/10.1029/JZ067i011p04427>.
- Becerra, D. M., 2017, Integrated geological characterization at the bed scale of the Woodford Shale at the I-35 outcrop, southern Oklahoma: M.S. thesis, University of Oklahoma.
- Burch, D., 2002, GC Seismic to Well Ties with Problematic Sonic Logs. *AAPG Explorer*, Part 1 February, Part 2 March.
- Curtis, D.M., S. C. Champlin, 1959, Depositional Environments of Mississippian Limestones of Oklahoma. *Tulsa Geol. Soc. Dig.* **27**, 90–103.
- Chopra, S., and K. J. Marfurt, 2007, Seismic attributes for prospect identification and reservoir characterization. *Society of Exploration Geophysicists and European Association of Geoscientists and Engineers*.
- Chopra, S., R. K. Sharma, and K. J. Marfurt, 2019, Integration of AVAz/VVAz and Coherence/Curvature Seismic Attributes. *AAPG Explorer*.

- Denison, R.E., 1982, Geologic cross section from the Arbuckle Mountains to the Muenster Arch in southern Oklahoma and Texas: Geological Society of America Map and Chart Series MC-28R, **8**, 1-12.
- Feinstein, S., 1981, Subsidence and thermal history of southern Oklahoma aulacogen; implications for Petroleum exploration: American Association of Petroleum Geologists Bulletin, **65**, 2521–2533.
- Fishman, N. S., G. S. Ellis, A. R. Boehlke, S.T. Paxton, and S. O. Egenhoff, 2013, Gas storage in the upper Devonian-lower Mississippian Woodford Shale, Arbuckle Mountains, Oklahoma: How much of a role do chert beds play?, in J. Y. Chatellier and D. M. Jarvie, eds., Critical assessment of shale resource plays: AAPG Memoir **103**, 81–107.
- Galvis, H. A., 2017, Detailed lithostratigraphic characterization and sequence stratigraphy of a complete Woodford Shale outcrop section in Southern Oklahoma: M.S. thesis, University of Oklahoma.
- Gatewood, L.E., 1978, Stratigraphic trap possibilities in the Arbuckle Group; general relationships: Shale Shaker, **28**, no. 10, p. 219–227.
- Goodway, B., Perez, M., Varsek, J. and Abaco, C., 2010, Seismic petrophysics and isotropic-anisotropic AVO methods for unconventional gas exploration. The Leading Edge, **29**, 1500-1508.
- Ham, W. E., 1973, Regional geology of the Arbuckle Mountains, Oklahoma: Oklahoma Geological Survey Special Publication **73**–3, 56 p.
- Ham, W. E., and J. L. Wilson, 1967, Paleozoic epeirogeny and orogeny in the central United States. American Journal of Sciences, **265** 332-407.

- Hart, B. S., R. Pearson, & G. C. Rawling, 2002, 3-D seismic horizon-based approaches to fracture-swarm sweet spot definition in tight-gas reservoirs. *The Leading Edge*, **21(1)**, 28-35.
- Higgins S., S. Goodwin, A. Donald, T. Bratton and G. Tracy, 2008, Anisotropic stress models improve completion design in the Baxter Shale:SPE 115736.
- Lynn, H.B., 2018, The fabric, or internal structure, of rocks – The patterns of Anisotropy: AAPG Search and Discovery Article No. 42188.
- Marfurt, K.J. and T. M. Alves, 2015, Pitfalls and limitations in seismic attribute interpretation of tectonic features. *Interpretation*, **3**, pp.5-15
- Meckel, L. D. and A. K. Nath, 1977, Geologic consideration for stratigraphic modelling and interpretation. In *Seismic Stratigraphy – Application to Hydrocarbon Exploration*, ed. C.E. Payton. AAPG Memoir **26**, 417-438.
- Perry, W. J., 1989, Tectonic evolution of the Anadarko Basin Region, Oklahoma: United States Geological Survey Bulletin **1866-A**, 1-16.
- Rickman, R., M. J. Mullen, J. E. Petre, W. V. Grieser, and D. Kundert, 2008, A practical use of shale petrophysics for stimulation design optimization: All shale plays are not clones of the Barnett Shale: Presented at the SPE Annual Technical Conference and Exhibition.
- Rüger, A., 2002, Reflection coefficients and azimuthal AVO analysis in anisotropic media. Geophysical Monograph Series Number **10**, SEG Publication.
- Saberi, M. R. and J. Ting, 2016. A workflow to model anisotropy in a vertical transverse isotropic medium: *First Break*, **34**, (10), 41-48.

- Sayers, C. M., 1994, The elastic anisotropy of shales: *Journal of Geophysical Research* **B 99**, 767–774.
- Sheriff, R.E., 2002, *Encyclopedic Dictionary of Exploration Geophysics*: SEG Books, Tulsa, Oklahoma.
- Simm, R., and M. Bacon, 2014. *Seismic Amplitude: An interpreter's handbook*. Cambridge University Press.
- Slatt, R.M., 2006, Stratigraphic reservoir characterization for petroleum geologists, geophysicists, and engineers, **61**. Elsevier.
- Slatt, R.M. and Y. Abousleiman, 2011, Merging sequence stratigraphy and geomechanics for unconventional gas shales: *The Leading Edge*, **30**, 274-282.
- Thomsen, L., 1986, Weak elastic anisotropy: *Geophysics*, 5b, 1954-1966.
- Treadgold, G., C. Sicking, V. Sublette, and G. Hoover, 2008, Azimuthal processing for fracture prediction and image improvement: 78th Annual International Meeting of the SEG, Expanded Abstracts, 988-992.
- Tsvankin, I. and L. Thomsen, 1994, Non-hyperbolic reflection moveout in anisotropic media: *Geophysics*, **59**, 1290–1304.
- Webster, R.E., 1980, Evolution of S. Oklahoma aulacogen: *Oil and Gas Journal*, **78**, no. 7, 150–172.
- Weltje, G. J., X. D. Meijer, and P. L. De Boer, 1998, Stratigraphic inversion of siliciclastic basin fills: a note on the distinction between supply signals resulting from tectonic and climatic forcing: *Basin Research*, **10** (1), 129-153.

Widess, M.B., 1973, How thin is a thin bed: *Geophysics*, **38**, 1176-1180.

Wright, J., 1987, The effects of transverse isotropy on reflection amplitude versus offset.

Geophysics: **52**, 564–567.

7 Appendix

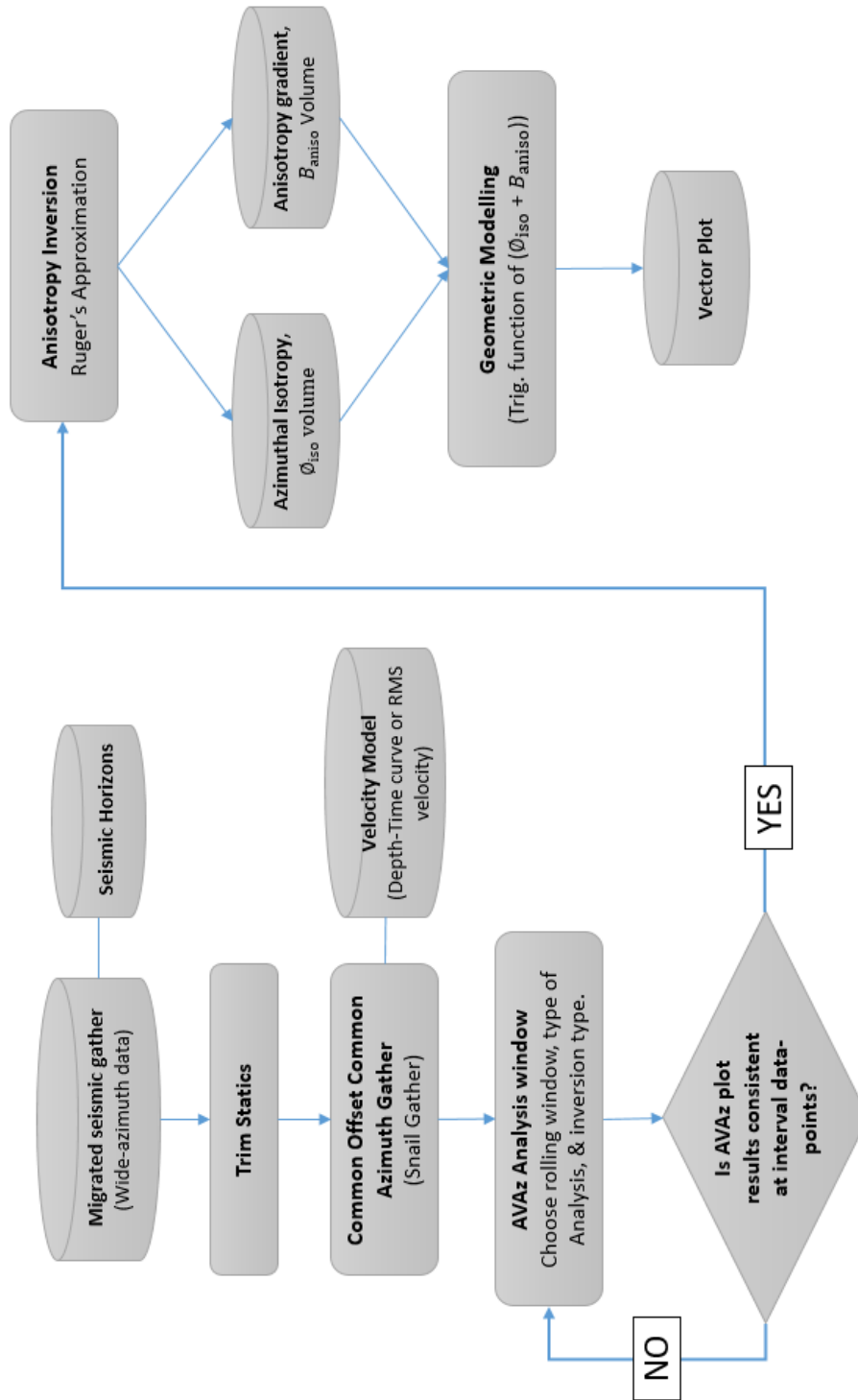


Figure A.1 AVAz Analysis and Inversion Algorithm Flow chart

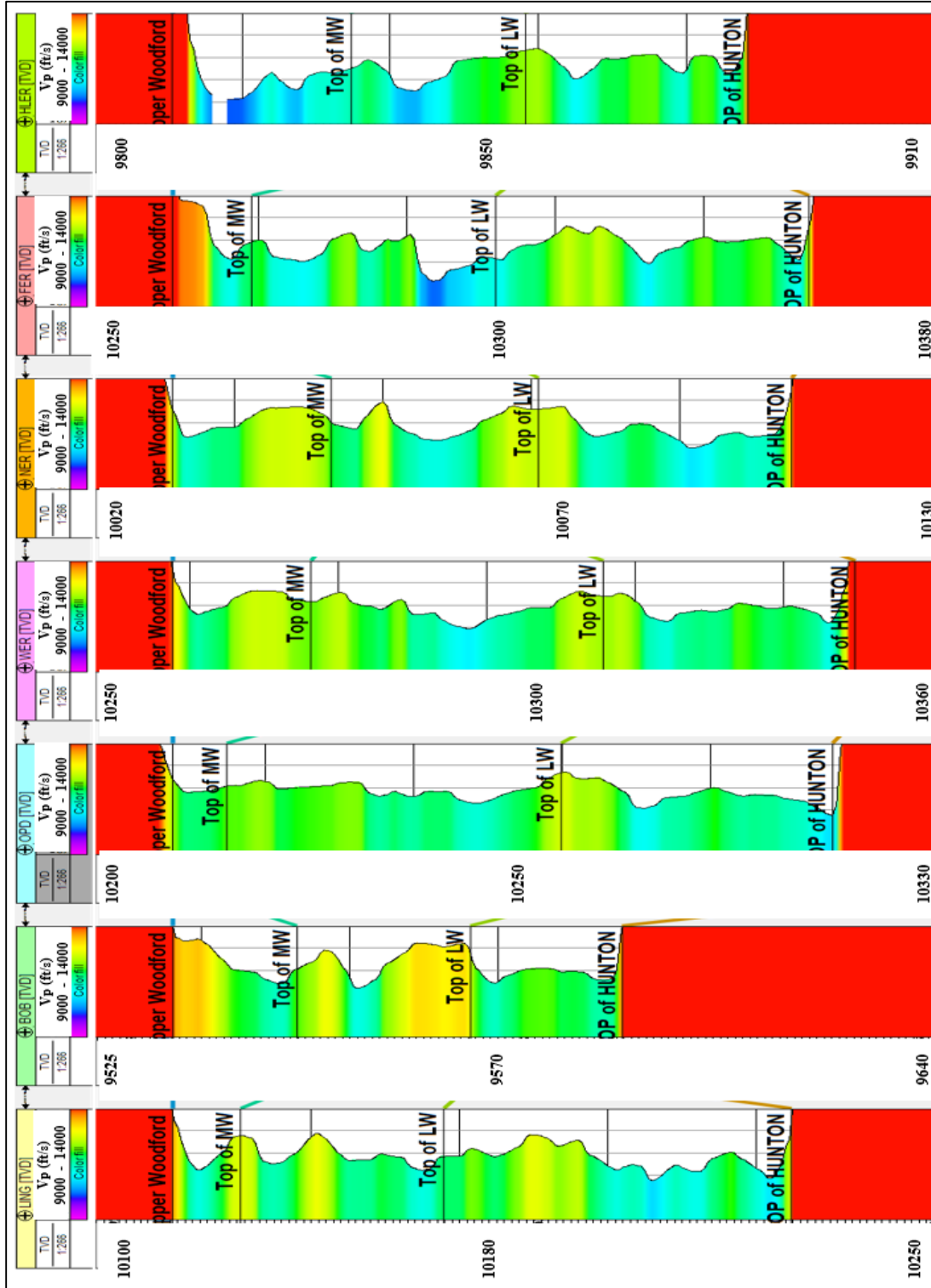


Figure A.2 Log display of compressional velocity profile across seven (7) wells. Overlaying the upper Woodford shale is the Osagean formation and underlying the lower Woodford Shale is the Hunton group. Flattened on the upper Woodford Shale. There is no clear velocity distinction between upper, middle (MW) or lower Woodford (LW) formation as the velocities are relatively the same from well log data.